CHALMERS
UNIVERSITY OF TECHNOLOGY

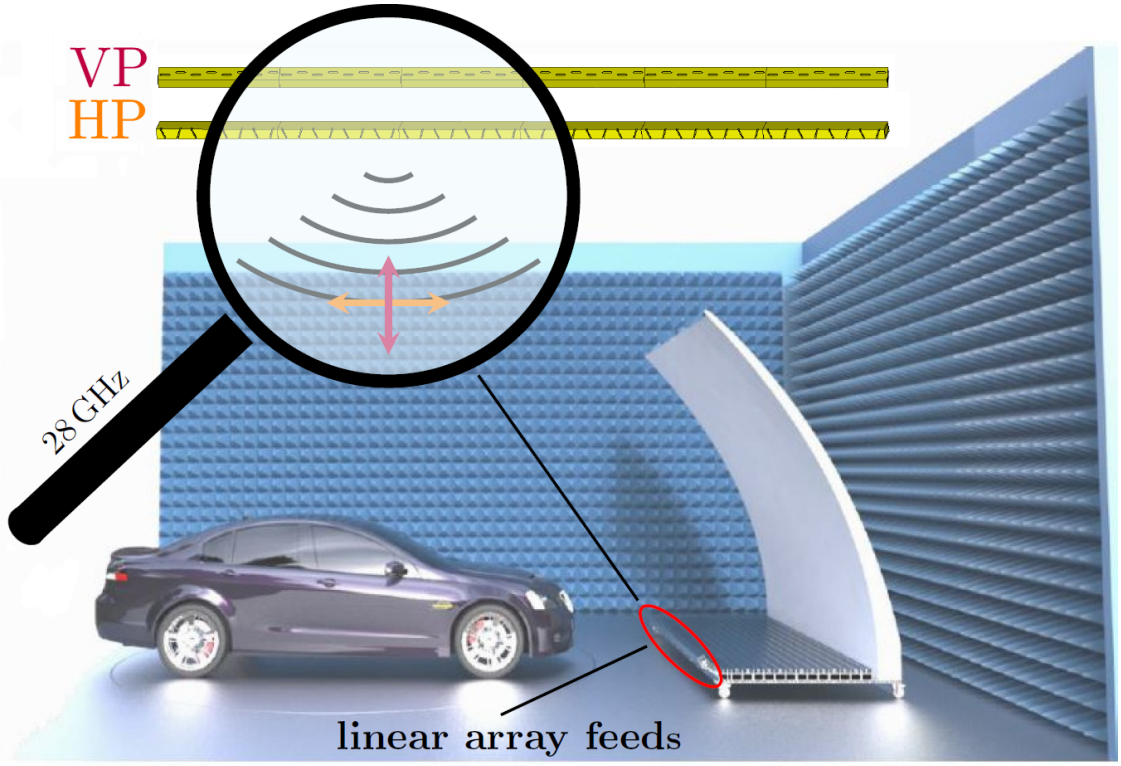

Design and Simulation of a Vertically and a Horizontally Polarized Array Feed for a 28 GHz Random-LOS Test Setup for Vehicular applications

Master's thesis in Wireless, Photonics and Space Engineering

KEVIN JOHANHAGE

Department of Electrical Engineering
CHALMERS UNIVERSITY OF TECHNOLOGY
Gothenburg, Sweden 2018

Master's thesis 2018

Design and Simulation of a Vertically and a Horizontally Polarized Array Feed for a 28 GHz Random-LOS Test Setup for Vehicular applications

KEVIN JOHANHAGE

CHALMERS
UNIVERSITY OF TECHNOLOGY

Department of Electrical Engineering
Division of Communication and Antenna Systems
Antenna Systems group
Chalmers University OF Technology
Gothenburg, Sweden 2018

Design and Simulation of a Vertically and a Horizontally Polarized
Array Feed for a 28 GHz Random-LOS Test Setup for Vehicular applications
KEVIN JOHANHAGE

Supervisors:
Jan Carlsson, Department of Signals and Systems, Chalmers / Provinn AB
Madeleine Schilliger Kildal, Department of Electrical Engineering, Chalmers

Examiner:
Jian Yang, Department of Electrical Engineering, Chalmers

Master's Thesis 2018
Department of Electrical Engineering
Division of Communication and Antenna Systems
Antenna Systems group
Chalmers University of Technology
SE-412 96 Gothenburg
Telephone +46 (0)31 772 1000

Cover: Illustration of the Random-LOS test setup. The linear array feeds that was simulated for 28 GHz are shown. The vertical/horizontal polarization radiated by the feeds are suggested. Note that the displayed reflector not is intended to be used with the 28 GHz feeds.

Typeset in LaTeX
Gothenburg, Sweden 2018

Design and Simulation of a Vertically and a Horizontally Polarized Array Feed for a 28 GHz Random-LOS Test Setup for Vehicular applications

KEVIN JOHANHAGE
Department of Electrical Engineering
Chalmers University of Technology

Abstract

Within a few decades, autonomous vehicles are likely to be a part of our everyday life. In order to ensure safe autonomous driving for passengers and pedestrians, strict performance requirements will be imposed on vehicular antennas that will be used to enable autonomous driving. This present an acute future need to perform large-scale testing of these antenna in a manner that is both fast and cheap and highly reliable and accurate. To meet this need has a hypothesis together with a propagation environment relevant for vehicular antennas been developed. This environment is called Random-LOS and assumes that a dominant LOS-component are present at most times but that the AoA of this component varies randomly. In order to utilize the hypothesis for testing of vehicular antennas, a setup that emulates the Random-LOS environment has been developed. The LOS-component in the setup is generated with a reflector that is fed with two linear arrays with orthogonal linear polarizations. The latter is needed so that MIMO capabilities can be evaluated. In order to evaluate the quality of the generated LOS-components, two figure of merits (power spread and phase spread) are used. These figures are evaluated for a circular area known as the *test-zone* that is assumed to completely surround the vehicular antenna. The present setup has not yet been designed to accommodate the coming 5G system where 28 GHz will be an important frequency.

The aim of this Thesis is to design the feeds as rectangular waveguide slot arrays for 28 GHz. The aim was divided into two sub-tasks as follows. In the first task, a preliminary study was conducted in the simulation program called WSAP. The purpose of this study was to investigate which array configuration, i.e. the number of antenna elements and the distance between the elements, that could be used to achieve a power/phase spread below 1 dB/10 ° at a distance of 1-2 m between the array and the vehicular antenna and for a 30 cm diameter of the test zone. In the second task, the appropriate array configuration was realized as slot arrays in CST. Two slot arrays, i.e one with vertical polarization och one with horizontal polarization, were designed. The slot arrays should be designed to be as broadband as possible, and at the same time yield a sidelobe level below -9 dB.

Simulations in WSAP were performed without considering the reflector. However, in WSAP, simulations were performed in free space and the linear array were located in the same plane as the test-zone. Under these specific conditions, a reflector fed by a linear array yields that same field-variation as using the linear array alone. This is enough for qualitatively evaluating the LOS-component. Simulations of the linear array were performed by sweeping a transmitting dipole in a $2\,\text{m} \times 2\,\text{m}$ grid in front of 128 sample points with a spacing of $\frac{\lambda}{2}$, where λ corresponded to 28 GHz. The dipole was sampled in each grid point and a spacing of 5 mm between the grid points was used. Due to the reciprocity and linearity of electromagnetic fields, the total field sampled by the 128 points in one grid position, is equivalent to the field that would be measured in the same position from an array with 128 elements and the same spacing. However, this assumes that the elements in the array are uniformly excited. The field corresponding to the 128 sample points could then be reconstructed by loading the sampled data for the $2\,\text{m} \times 2\,\text{m}$ grid into

Matlab. From this, data corresponding to the 30 cm test zone at different distances could be extracted, from which the power/phase spread could be calculated. In Matlab, sample points were also disregard for all grid positions. This allowed the field from thinner array configurations to be reconstructed. Seven arrays with different number of elements and a spacing of either $\frac{\lambda}{2}$ or λ were evaluated at the distances of 1 m, 1.5 m and 1.8 m between the array and the test-zone. The result of this analysis showed that a configuration of 48 elements and a spacing of λ could meet the requirements for the power/phase spread. This configuration was selected for the next sub-task of the Thesis.

Three different slot arrays were designed in CST. The slots were placed on a WR-28 waveguide. In order to excite the slots uniformly, slot arrays of standing wave type were considered. Two vertically polarized slot arrays as well as one horizontally polarized slot array were designed. For the vertically polarized arrays, two different types of slots, referred to as "rounded" and "dumbbell", were considered. In order to achieve broadband performance for all three arrays, each array was divided into 6 identical array sections with 8 slots. The sections were then placed end-to-end to maintain constant spacing between the slots. However, this prescribed that the each sections must be center fed. In general, it was seen that the performance of the array sections in terms of bandwidth and sidelobe level was in line with what one would expect given the number of slots that was used. The horizontally polarized array section/array provided better radiative performance, i.e. lower sidelobe level, than the vertically polarized array sections/arrays. However, the horizontally polarized array section/array were more narrowband than the vertically polarized counterparts. The sidelobe level of all three array sections/arrays were below the required -9 dB level. Furthermore, it was conclude that the array where rounded slots were used, performed somewhat better in terms of bandwidth than the array where dumbbell slots were used. It is therefore recommended that the array with rounded slots are used to provide the vertical polarization in the setup.

Keywords: Maxwell's equations, Plane wave propagation, Line-of-Sight, Rich Isotropic Multipath, Random Line-of-Sight, Vehicular antennas, Measurement setup, Rectangular waveguide, Slot antennas, Orthogonal linear polarizations, 28 GHz.

Acknowledgements

This Master Thesis has been carried out at the Department of Electrical Engineering, Antenna Systems group at Chalmers University of Technology for RanLOS. First and foremost, I would like to thank my supervisors Adj. Professor Jan Carlsson and Industrial PhD student Madeleine Schilliger Kildal. You have always taken time from your busy schedules and heavy workloads to help me. I would especially like to thank Madeleine for proofreading this thesis and providing me with useful feedback that made this Thesis much better. Also because You have been available daily and when You have helped me, always done it with a patient and friendly attitude - even when I had taken a long time to understand a concept and asked too many questions in the meantime.

I would also like to thank Professor Jian Yang at the Antenna Systems group who has been the examiner for this Thesis. I would like to extend my thanks to Jian for the useful help and advice I have received during meetings.

Thanks to Lars Granbom, CEO at RanLOS, to make me feel welcome and been nice and entertaining when we met.

A thanks should also be extended to PhD students Sadegh Mansouri Moghaddam and Abbas Vosoogh at the Antenna Systems group. Sadegh helped me on a few occasions when I had technical questions about CST and Abbas showed me how to extract the embedded radiation pattern for a slot in CST according to the depiction in Fig.A.2.

I would like to thank my family who always has supported me in desperate times throughout this thesis and during the years when I have been a student at Chalmers. Finally, I would like to thank selected students in MPWPS for all memorable moments that we shared together in 6217 and elsewhere, both within and outside of Chalmers.

Kevin Johanhage, Gothenburg, August 2018

List of Acronyms

EM	Electromagnetic
PEC	Perfect Electric Conductor
SLL	Sidelobe Level
Tx	Transmitting Antenna
Rx	Receiving Antenna
LOS	Line-of-Sight
AC	Anechoic Chamber
AUT	Antenna Under Test
VNA	Vector Network Analyzer
RIMP	Rich Isotropic Multipath
AoA	Angle of Arrival
RC	Reverberation Chamber
Random-LOS	Random Line-of-Sight
MIMO	Multiple Input Multiple Output
V2B	Vehicle to Base Station
V2V	Vehicle to Vehicle
FoM	Figure of Merit
RBS	Radio Base Simulator
TEM	Transverse Electromagnetic
TE	Transverse Electric
TM	Transverse Magnetic
SWA	Standing Wave Array
TWA	Traveling Wave Array
MoM	Method of Moment
XP	Relative Cross-polar level
WSAP	Wire Structure Analysis Program
CST	Computer Simulation Technology-Microwave Studios

List of Symbols

All symbols, with a few exceptions, that are used thought this thesis are listed below. The symbols are grouped according to the sections where the they first appear. The symbols on this list are linkable from the place in the running text where they are introduced. If the symbols occurs multiple times in the running text, is the variable linked each time it appears. Symbols occurring in a `\begin {equation} ... \end {equation}` block or in inline equations containing `\frac{}{}`, `\sqrt{}` or subscript/superscript, is not linked. This is because the link itself corrupts the symbol font.

Maxwell's Equations and the plane wave solution

$\vec{D}$	Electric flux density [C $\times$ m^{-1}]
$\vec{B}$	Magnetic flux density [Wb $\times$ m^{-1}]
$\vec{E}$	Electric field strength [V $\times$ m^{-1}]
$\vec{H}$	Magnetic field strength [A $\times$ m^{-1}]
ϵ	Permittivity [F $\times$ m^{-1}]
μ	Permeability [H $\times$ m^{-1}]
ϵ_0	Free space permittivity [F $\times$ m^{-1}]
μ_0	Free Space Permeability [H $\times$ m^{-1}]
ϵ_r	Relative permittivity [$\cdot$]
μ_r	Relative permeability [$\cdot$]
ρ	Charge density [C $\times$ m^{-3}]
$\vec{J}$	Current density [A $\times$ m^{-2}]
$\vec{J}_{cond}$	Conduction current density [A $\times$ m^{-2}]
$\vec{J}_{drift}$	Drift current density [A $\times$ m^{-2}]
$\vec{\nabla}$	Del operator

The Wave Equation and the Plane Wave solution

E_x	Complex field component of $\vec{E}$ in x [V $\times$ m^{-1}]
E_y	Complex field component of $\vec{E}$ in y [V $\times$ m^{-1}]
E_z	Complex field component of $\vec{E}$ in z [V $\times$ m^{-1}]
H_x	Complex field component of $\vec{H}$ in x [A $\times$ m^{-1}]
H_y	Complex field component of $\vec{H}$ in y [A $\times$ m^{-1}]
H_z	Complex field component of $\vec{H}$ in z [A $\times$ m^{-1}]
v	Propagation velocity of a general wave [m $\times$ s^{-1}]
k	Free space wave number [rad $\times$ m^{-1}]
η	Wave impedance of free space [Ohm]
j	Imaginary unit
ω	Angular velocity [rad $\times$ s^{-1}]
E_{0x}	Amplitude of E_x [V $\times$ m^{-1}]
H_{0y}	Amplitude of H_y [V $\times$ m^{-1}]
ϕ_x	Phase of E_x [rad]
ϕ_y	Phase of H_y [rad]
γ	Complex propagation constant [rad $\times$ m^{-1}]

α Attenuation constant [Np $\times$ m^{-1}]
β Propagation constant [rad $\times$ m^{-1}]

The Wave Equation in a Conductive Medium

$\vec{E}_2$ Electric field in PEC-region [V $\times$ m^{-1}]
$\vec{H}_2$ Magnetic field in PEC-region [A $\times$ m^{-1}]
$\hat{n}$ Surface normal pointing outwards from the PEC-region [m]
ρ_s Surface Charge Density [C $\times$ m^{-2}]
$\vec{J}_s$ Surface Current Density [A $\times$ m^{-1}]
δ_{skin} Skin depth [m]
σ Conductivity [S $\times$ m^{-1}]

Antennas in Pure-LOS

D_a Minimum diameter of antenna covering all radiating structures [m]
λ Free space wavelength [m]
$G(\mathbf{r})$ Far-field function [V]
r Scalar distance between Rx and Tx antenna
$\mathbf{r}$ Distance vector between Rx and Tx antenna [m]
$\hat{r}$ Unity vector for distance between Rx and Tx antenna [m]
ϕ_{az} Azimuth angle [°]
θ_{pol} Polar angle [°]
E_{XP} Cross-polar component [V $\times$ m^{-1}]
$E_{CO_{max}}$ Maximal CO-polar component [V $\times$ m^{-1}]

The Random-LOS Test Setup

R Radius of test-zone [m]
h Height of test-zone [m]
D Distance to center of test-zone [m]
F Focal distance [m]
L_f Length of linear feed [m]
h_r Height of reflector [m]
L_r Length of reflector [m]
θ_{feed} Tilt angle of linear feed [°]
N Total number of: antenna elements in the linear feed used in the Random-LOS test-setup/slots in the SWA that is designed in CST/sample points used in WSAP
d Spacing between antenna elements/slots [m]

The Test Zone

$\vec{E}_{tot}$ Total field from N antenna elements in a point given by $\mathbf{r}$ [m]
$\mathbf{r_n}$ Positional vector of n^{th} antenna elements in the linear feed [m]
$\hat{r}_n$ Phase reference point of n^{th} antenna elements in the linear feed [m]

$G(\hat{r}_n)$	Far-field function of the n^{th} antenna elements in the linear feed [m]
$Var[\cdot]$	Operation of calculating the variance of a set of values
$Mean(\cdot)$	Operation of calculating the mean of a set of values
$arg(\cdot)$	Operation of calculating the argument of a set of complex numbers
P_{samp}	Power of a field sample [$V^2 \times m^{-2}$]
P_{norm}	Normalized power of a field sample within the test zone [$V^2 \times m^{-2}$]
σ_{dB}	Standard deviation (in dB) of all P_{samp} within the test zone.
σ	Standard deviation (in linear units) of all power samples within the test zone.
ϕ_{samp}	Phase of a field sample [°]
ϕ_{norm}	Normalized phase of a field sample [°]
$\Delta\phi_{max}$	Phase spread of the test zone [°]

EM Propagation in Transmission Lines

$\vec{E}_t$	Transverse $\vec{E}$-field components of a plane wave propagating in z [$V \times m^{-1}$]
$\vec{H}_t$	Transverse $\vec{H}$-field components of a plane wave propagating in z [$A \times m^{-1}$]
β_{mn}	Propagation constant of the TE_{mn}-mode in a R-WG [$rad \times m^{-1}$]
k_c	Cut-off wave number [$rad \times m^{-1}$]
∇_t	Del operator applied on the transverse field components
k_x	Wave number in x-direction [$rad \times m^{-1}$]
a	The longer dimension of the waveguide cross section [m]
b	The shorter dimension of the waveguide cross section [m]
m	Mode number
n	Mode number
f_c	Cutoff frequency of the TE_{mn}-mode [Hz]
c_0	Speed of light in vacuum [$m \times s^{-1}$]
$\lambda_{g_{mn}}$	Guided wavelength of the TE_{mn}-mode [$m \times s^{-1}$]

A Single Slot in the Wall of a Rectangular Waveguide

$Z_{TE_{mn}}$	Impedance of a R-WG when a TE_{mn} wave propagates thought the guide [Ohm]
Z_{rad}	Antenna radiation impedance [Ohm]
R_{rad}	Antenna resistance [Ohm]
X_{rad}	Antenna reactance [Ohm]
Y_{rad}	Antenna addmittance [S]
G_{rad}	Antenna conductance [S]
B_{rad}	Antenna susceptance [S]

Properties of a Single Slot

ϕ	Rotation angle of a compound slot [°]
δ_{pos}	Offset position from center-line of a longitudinal slot [m]
$\vec{J}_x$	x-component of the surface current density on the walls of a R-WG that is fed with the TE_{10} mode [$A \times m^{-1}$]
$\vec{J}_y$	y-component of the surface current density on the walls of a R-WG that is fed with the TE_{10} mode [$A \times m^{-1}$]

$\vec{J_z}$ z-component of the surface current density on the walls of a R-WG that is fed with the TE_{10} mode [$A \times m^{-1}$]
Y_s Slot addmittance [S]
y Slot addmittance normalized by the waveguide admittance
s_{11} Reflection coefficient corresponding to the normalized addmittance
Z_s Slot impedance [Ohm]

Design of a Slot Array Antenna

y_{in} Input addmittance of a R-WG SWA antenna
y_n Normalized admittance of the n^{th} slot in an R-WG SWA antenna
g_n Normalized conductance of the n^{th} slot in an R-WG SWA antenna
S_{11} Nonnormalized reflection coefficient
Δf_{-10dB} The bandwidth for which the return loss of an antenna is below $-10\,\mathrm{dB}$

Near-Field Simulations Using WSAP

L_x Distance in x sweeped out by the dipole [m]
L_y Distance in y sweeped out by the dipole [m]

Simulation of the N-Slot Array in CST

n Number of slots in a SWA section ($n < N$)

Investigation of the Slot Admittance

l Slots length [m]
w Slot width [m]
r_{slot} Slot radius of dumbbell slot [m]
δ_l Variable used to vary the slot length [m]
l_{inner} Inner length of the compound slot when placed on the narrow wall of a R-WG [m]
l_{WG} Length of a SWA section [m]
n_s The final number of slots that were used for each SWA section

Design of the n_s-Section

f_{upper} Lower frequency corresponding to Δf_{-10dB} of the SWA section [Hz]
f_{lower} Upper frequency corresponding to Δf_{-10dB} of the SWA section [Hz]
f_{center} Middle frequency corresponding to Δf_{-10dB} of the SWA section. Note that this variable always is considered at 28 GHz regardless if it is the true middle frequency of Δf_{-10dB} or not [Hz]

Design of the n_s-Section

δ_b Variable used to vary the port width of the SWA section [m]
$\delta_{pos,c}$ Offset position of the two slots located closest to the port [m]

ϕ_c	Rotation angle of the two slots located closest to the port [°]
$\delta_{l,c}$	Variable used to vary the length of the two slots located closest to the port [m]
δ_d	Variable used to vary the length of the SWA section [m]
P_h	Height of post used to mitigate the port mismatch [m]
P_d	Depth of post used to mitigate the port mismatch [m]
P_w	Width of post used to mitigate the port mismatch [m]
W_h	Height of wedge used to mitigate the port mismatch [m]
W_d	Depth of wedge used to mitigate the port mismatch [m]
W_w	Width of wedge used to mitigate the port mismatch [m]

Contents

List of Figures

List of Tables

1
Introduction

One of the promises with the technology in the foreseeable future is the transition to autonomous vehicles that can navigate without any or with very few requirements on human interactions. Autonomous vehicles offer many attractive benefits such as safer driving, where fatigue, alcohol, drugs and other "flaws" associated with human drivers looses its role. Another advantage is more effective traffic flow, as the autonomous vehicles can drive very close to each other in traffic (known as platooning) and generally navigate in a manner that maximizes traffic flow. This kind of driving cannot be performed consistently by human drivers interacting with other human drivers. Autonomous vehicles are also expected to reduce emissions, since human driving patterns contain fast accelerations, heavy breaking, etc., which is associated with higher fuel consumption. Finally, autonomous vehicles may liberate a substantial part of our daily life as the time that we now spend on commuting back and forth to work etc. can be used for something else.

Before autonomous vehicles can break through and become part of our everyday life, great challenges regarding engineering and infrastructural planning must first be solved. An example of these challenges is the handling of the vast amounts of data that autonomous vehicles will consume and produce. It is anticipated that each autonomous vehicle will be equipped with two different sensor systems (Radar and LIDAR) for long - and mid-range, as well as sonar systems for short-range and camera systems for recognition of road signs, traffic signals, pedestrians etc. [1]. In addition to the systems that the vehicles must have to navigate safely in the immediate traffic, the vehicles must also be able to access a large amount of external data for an overall safe and comfortable driving experience. This includes for example data for navigation, traffic space and weather information, as well as entertainment, such as real-time video -and audio streaming [1]. In [1], an estimate is made that a fully autonomous vehicle will produce and consume on average 4000 GB of data during a single day which is approximately equivalent to 2.66 internet users.

It is predicted that a large number of micro base stations that act as nodes in a large information network will be placed along roads in order to handle the vast amount of data required by the autonomous vehicles. Networks, which largely depend on wireless communication with antennas, will hence be developed. This, in turn, prescribes that strict requirements will be placed on the performance of the antennas used in these networks to ensure safe autonomous driving for passengers and pedestrians [2],[3]. The need to test these antennas on a large-scale requires a test method that is both cheap and fast, while also being accurate and reliable. In order to accommodate this need, was the Random Line-of-Sight (Random-LOS) environment developed [2],[4]. Random-LOS is a propagation environment that is relevant for vehicular antennas [2],[3]. A hypothesis that links the Random-LOS environment to another propagation environment has also been formulated [5],[6]. The actual hypothesis itself allows for a fast and reliable way to evaluate the performance of vehicular antennas [2],[4]. In order to understand both the

Random-LOS environment and the significance of the hypothesis for testing of vehicle antennas, should a general discussion about antenna testing first be made.

All real-life environments where an antenna will be used can radiatively be confined between two ideal propagating environments. The environments will from this point be referred to as *edge-environments* [7],[10]. Let us first discuss testing of fixed antennas.

Fixed antennas are commonly evaluated in the "traditional" way, i.e. on a test range using one transmitting (Tx) and one receiving (Tx) antenna [8],[9]. The antennas are typically located in each other's far-field [9]. One of the antenna constitutes the Antenna Under Test (AUT), i.e. the antenna that is to be evaluated [8],[9]. At shorter far-field ranges, i.e. up to tens of meters, test-ranges that are located indoors are typically used. The testing is then commonly performed in an anechoic chamber (AC) to eliminate indirect wave paths between the Rx and Tx antenna due to reflections from the ground and walls [8],[9].

The AUT that is characterized through traditional testing is typically supposed to communicate with other antennas that also are fixed [9]. The communication with the AUT is therefore supposed to be more or less predictable over time, i.e. the AUT will receive/transmit signals mainly from a dominant direction corresponding to the other antennas that it communicates with. This means that the AUT will, during most of the time, be in Line-of-Sight (LOS) with the other antennas [9],[8]. The radiation pattern is then a relevant performance metric of the AUT as it indicates how the AUT should be pointed to communicate optimally with the other antennas, i.e. receive/transmit the strongest signals [8].

In the far-field, the signals that are received/transmitted by the AUT may be approximated as plane waves [12],[11]. For traditional testing, will the number of plane waves that is received by the AUT typically be small due to the dominant LOS-component. This means in turn that the amplitude, phase, polarization and incident direction, which are the unique features of a plane wave, will vary little over time [8]. Traditional antenna testing can hence be said to recreate a LOS environment, i.e. an environment in which a dominant LOS-component exists. The pure-LOS environment is the extreme or ideal case of the LOS environment [5]. In pure-LOS is only a single plane wave present between two antennas [5],[7]. The LOS-component is then completely dominant, meaning that the amplitude, phase, polarization and direction of the received/transmitted signal are deterministic unless any of these features are deliberately changed [7]. The pure-LOS is one of the two edge-environments [5].

In an environment opposite to pure-LOS, will a large number of plane waves exist between the Rx and the Tx antenna due to multipath [10]. Multipath occur to a much greater extent when a large number of scattering objects exist between the antennas [11]. Consequently, for fixed antennas, the number of planar waves will generally vary from few to many when the antennas are used in a environment that is more rich on scattering objects, i.e. in urban rather than a rural settings. Rich Isotropic Multipath (RIMP) is a propagation environment where a very larger number of plane waves exist. RIMP represent the second edge-environment for fixed antennas [7],[10]. Due to the large number of plane waves will fading be very fast in RIMP if scatters are moving in this environment. The strong fading in that case means that the received/transmitted amplitude, phase and polarization effectively will vary randomly over time. Additionally, the large number of planar waves will cause the angle of arrival (AoA) of the waves to effectively be incident from any direction [7],[12]. Since the received signal varies randomly in RIMP will the

radiation patter be an irrelevant performance metric of the AUT. Useful metrics are instead those that describe the performance of the antenna in a statistical sense. [12]. Antenna testing in a RIMP environment can be performed in a reverberation chamber (RC), where the chamber essentially act as a cavity resonator that allows a large number of planar waves between the Tx and Rx antenna [12]. Metallic plates are moved inside the chamber, which yields the fading.

Let us now consider the autonomous vehicles that communicate with the base stations. Autonomous vehicles will typically navigate in open landscapes (highways and other open roads) so that in most cases there will be a LOS-component between vehicles and base stations (V2B) or between the vehicles themselves (V2V) [2],[3],[10]. When autonomous vehicles have broken through, will the next generation communication system, i.e. 5G or possibly 6G, be used. These systems will push towards the use of higher frequencies to allow for large throughput of data. At these higher frequencies will the far-field occur at shorter distances, i.e. within a few meters and shorter, which mean that the communication V2B and communication V2V can be assumed to occur in the far-field [3],[10], [4]. The amplitude, phase and polarization when will then be quite small due to the LOS-component or *plane wave* that will be present. However, due to the motion of the vehicles will the relative position between V2B and V2V constantly be changed. The AoA of the LOS-component will therefore vary randomly. However, the AoA will only vary randomly in the azimuth plane as the variation of the polar angle of the antenna will be quite limited. From these observations, we can define the Random-LOS for vehicular antennas as an environment in which a dominant LOS-component exist at most time but where the AoA varies randomly [13],[14]. Due to movement of a vehicle antenna will fading always be present in Random-LOS, but it will be slow due to the LOS-component [5],[10]. It should also be pointed out that the radiation pattern of an antenna in Random-LOS is relevant, but the antenna must be able to receive/transmit well in any direction in the azimuth plane due to the random AoA [5].

We have defined two edge-environments for fixed antennas (pure-LOS and RIMP). These environments can be recreated for testing purposes in the AC and the RC, respectively [6],[5]. In addition, Random-LOS which is a relevant propagation environment for vehicle antennas has also been defined. Generally, the real environment where a fixed AUT will be used can neither be completely described with pure-LOS or RIMP. The propagation will instead always be somewhere on the spectrum between these environments, i.e. there will be more or less of and pronounced LOS-component. It is generally impossible to predict exactly where on this spectrum the real environment might lie, as all real environments are complex and ever-changing [7]. In order to make a simplification of antenna testing has a hypothesis been develop [2],[3]. Let us first consider the hypothesis for fixed antennas. The hypothesis claims that

> *If an AUT performs well in both pure-LOS and RIMP, it will also, statistically speaking, perform well in all real-life environments and situations [6].*

The main benefit of the hypothesis is that it allows one to evaluate the performance of the AUT for real-life environments and situations based on the tested performance in two environments that already can be emulated. When the AUT is used for movable applications, will there always be fading. This means that for antennas used in movable applications

will the edge-environment be Random-LOS (slow fading) and RIMP (very fast fading). In order to exploit the hypothesis for testing of vehicular antennas, the Random-LOS environment must emulated. The next paragraph describes the development of the setup used for this purpose.

An outdoor test range can be used to emulate the LOS-component in the Random-LOS environment. However, accurate antenna testing requires an AC to eliminate indirect wave paths due to reflections. An outdoor testing area is also associated with many disadvantages, such as the antenna testing becoming weather-dependent, extra wear and tear on equipment and the need for access to land in which the test range can be accessed. This leaded to the need for an indoor test range located in an AC [5],[10]. However, since the variation of the polar angles of the vehicle antennas are limited, will the complete radiation pattern that is obtainable in an AC not be relevant [4],[16]. Instead was a semi-AC proposed for the setup [16]. In the proposed chamber was is also suggested that the LOS-component should be obtained through a transformation process rather than the AUT itself being located in the far-field. This allows a considerably smaller (and also cheaper) test-chamber to be used, i.e. a few meters instead of tens of meters [5],[4].

A semi-AC big enough to accommodate a vehicle with the AUT mounted on top of the vehicle was suggested. One reason for considering the vehicle in the test room and not just the AUT is that this allows evaluation of the whole system including both the antenna and the vehicle itself. [5],[2]. Testing the antenna in a similar way as it will be used, i.e. mounted on the vehicle, also enables more realistic testing [16]. The vehicle is placed on a turntable inside the chamber. The AUT receives the LOS-component from a chamber antenna placed a few meters in front of the turntable [15],[16]. In order to emulate randomly varying AoA of the LOS-component, the vehicle is rotated by the turntable as the AUT receives the LOS-component from the chamber antenna [5],[16]. The chamber antenna is connected to a radio base simulator (RBS) that emulates the performance of a real base station [15],[13]. The idea is that the transformation process ensure that plane waves are obtained at the output of the chamber antenna, meaning that the signals from the RBS will be obtained as if the RBS was placed in the far-field of the vehicle and the AUT [15],[4]. In order to evaluate the quality of the LOS-component that is received by the AUT, is the AUT alone considered to located in the center of a circular area. Within this area or *test zone*, should the transformation process yield a sufficiently plane wave. Two figure of merits (FoM's) are introduced. These are the power [dB] -and phase spread [°] [13]. An ideal plane wave has wave-fronts with zero variation in both power-and phase [13]. Note that the test zone as a concept is important as it requires sufficient good quality of the plane wave to be generated by the transformation process in a area and not just in one point. This relaxes the requirement of having to exactly place the AUT at this point to obtain a good LOS-component [4],[13].

The last detail that has not yet been discussed is the actual transformation process that provides the far-field. It also need to be discussed what kind of antenna that should be used for the chamber antenna.

In order to achieve a test zone with a diameter in order of several centimeters or decimeters, an antenna with a relatively large aperture must be used [5]. At the same time must the chamber antenna be able to provide two orthogonal polarized LOS-components so that MIMO capabilities also can be tested in the setup [5],[10]. In [5], a planar array was first suggested to be use as a chamber antenna. The signals from RBS are then transferred to the array antenna via a beamforming network that provides the actual

transformation of the RBS signals to the far-field [5]. In [15], the ability to emulate the LOS-component was investigated by attempting to generate a plane wave with a linear array. The ability to create a plane wave with a planar array was then investigated in [16]. In both [15] and [16], only simulated results were obtained by using ideal Huygens sources as antenna elements for the arrays. A center frequency of 3 GHz was considered. In [16] could it be shown that a power spread of less than 0.5 dB could be obtained over a test zone with radius of 1 m at 3 GHz when a planar array with 24×24 elements and a spacing of $0.1309\,\lambda$ were used.

It was argued in [17] that the LOS-component also could be generated by using a linear array as feed for a cylindrical reflector. It is than the reflector that act as the transformation process and generate the LOS-component. It was eventually argued that the planar array solution would become too expensive, especially if the setup should be able to be commercialized. The reason for this is the larger beamforming network required for a planar array compare to a linear array [13]. The company RanLOS that was founded in 2016, owns rights to the Random-LOS setup and acts to commercialize it [13]. RanLOS is thus the issuer of the task that is reported in this thesis. Before the specific task is discussed further, should some important results regarding the setup where the reflector solution is used first be mentioned. This will provide a better understanding of the task given by RanLOS.

In [4], the ability to generate a plane wave using the reflector solution was investigated through simulations. The linear feed consisted of 24 elements. Ideal Huygens sources was used for the antenna element. It was then found that a power spread less than 1 dB could be achieved over a test zone with 1 m radius for frequencies between 1.6 GHz to 2.8 GHz. One of the most recent (to the author's knowledge) contributions to the setup where the reflector + array feed solution are used, are reported in [18],[19] and [20]. In these works are practical measurements performed without a cylindrical reflector. In the absence of the reflector, several measurements have been made with the same linear array at adjacent positions to synthetically create a planar array that can generate the LOS-component.

In [18], the number of antenna elements required to obtain different values of power/phase spread in the test zone was examined. This was done using a simulation program called *Wire Structure Analysis Program* (WSAP), which is a Method of Moments (MoM) program written in C++. Three different antenna configurations were examined for different radii of the test zone and distance to the test zone. Furthermore, it was investigated how the presence of a ground plane in the simulations affected the power/phase spread. The simulations showed that the use of a planar array configuration gave the lowest power/phase spread, which also could be confirmed by measurements performed in an AC. The measurements also show that the power/phase spread predicted in the simulation was close to the measured values.

In the measurements, the self-grounded Bowtie antenna were used as element. The simulations and measurements were performed at 2.7 GHz. It was also concluded in [18] that the presence of a ground plane give rise to a ripple of the field in the test zone and thus to a greater power/phase spread and thus poorer quality of the generated LOS-component. However,this ripple could be avoided completely when using the planar array configuration.

This could be confirmed in [19], which describes practical measurements between a chamber antenna and an isolated vehicular antenna that constituted the AUT. The

measurement was performed in a semi-AC. In [19], the self-grounded Bowtie antenna was also used as antenna element. The measurements were performed between 1.6 and 3 GHz, which is the limited operating range of the chamber antenna that was used.

In [20], antenna measurements of the Random-LOS environment were performed for the very first time. A vehicle antenna mounted on the roof of a car constituted the AUT and was tested at 2.665 GHz. The car was placed on a turntable so that measurement for different AoA of the AUT could be evaluated.

RanLOS has expressed a desire to use the setup for the upcoming 5G system. In 5G, frequencies around 28 GHz will be important. To use the setup at this frequency, a different antenna element than the self-grounded bowtie antenna must be used for the linear feed. An task has therefore been issued by RanLOS to design a array feed that can be used at 28 GHz.

1.1 Aim and goals

The aim of this thesis is to further develop the Random-LOS test setup so that it can be used at 28 GHz. This means that a linear feed with a new type of antenna elements needs to be used for the cylindrical reflector. This linear feed must be designed for orthogonal linear polarizations. It has already been decided by RanLOS that an appropriate candidate for this purpose is a linear slot array based on a rectangular waveguide. The purpose of the report is therefore to design this linear feed for two orthogonal polarizations at 28 GHz. This purpose can be divided into two sub-tasks as follows

1. To perform a preliminary study with the simulation program WSAP. This study is performed with the purpose of finding out how the configuration of the linear feed affects the field variation that can be achieved in the circular test zone. The configuring of the linear feed means the number of antenna elements and the uniform spacing between these elements. Note that WSAP is a general field analysis program and that no specific antenna elements can be used in this program. A diameter of 30 cm is considered for the test zone. A distance of $1 - 2$ m between the linear feed and the center point of the test zone must be considered in the simulation. The achievable field-variation in the test zone must be characterized using the FoM's, i.e. power/phase spread, used in [18]. The goal is that the power spread should be less than 1 dB and that the phase spread should be less than 10° for the given distance to the test zone and size of the test zone.

2. The most appropriate configuration considered in the preliminary study is implemented as a linear slot array antenna using the program *Computer Simulation Technology - Microwave Studios* (CST-MWS or just CST). The most suitable feed means the feed out of the investigated ones that can meet the requirement. Two slot array feeds with orthogonal polarizations must be designed, i.e. one with vertical and one with horizontal linear polarization. The center frequency for the slot array feeds will be at 28 GHz. In order to allow the setup to be used for as large frequency range as possible, RanLOS has simply requested that the array feeds are designed for as large -10 dB bandwidth as possible with respect to the return loss of the feeds. In addition, the sidelobe level of the feeds should not be below -9 dB for reasonably good radiative performance.

Note that the reflector will not be considered in this thesis. In the previous section, it is emphasized that the LOS-component can be realized both with a planar array and with

a linear array that feeds a cylindrical reflector. Both of these ways of realizing the LOS-component will provide the same variation and strength of the field in the test zone if the aperture of the planar array is equal to the effective illuminated aperture of reflector. If a linear array of the same configuration as the linear array feed is used in free space and if the test zone is located in the same plane as this linear array, the linear array will give the same field variation as with the planar array solution or the reflector + array feed solution. These specific requirements, if impossible to meet practically, can quite easily be met in simulations. The field strength achievable with the linear array will be less compare to the other two setups, as a smaller aperture is obtained. However, it is the variation of the field inside the test zone that demonstrates the ability to create a sufficiently good plane wave with the chamber antenna and not the strength of the field itself. Simulation of the linear feed without taking the reflector into account can thus be justified. As for the simulations in WSAP, these will be performed without examining the effects of a ground plan, since it in [19] has already shown that ground induced ripple can be eliminated by using a planar array as chamber antenna which, in turn, can be realized with a reflector + array feed solution. The linear feeds will not be manufactured and no practical measurements will be performed. In order to achieve as large bandwidth as possible, each feed will be divided it into smaller sections that are put end-to-end to maintain constant spacing between each slot. To distribute the signals to each section of the feed, a beamforming network must be used. In addition, a transition component between the beamforming network and each section must also be used. Both the beamforming network and the transition component required to realize the feeds will not be considered in this thesis.

1.2 Outline of thesis

The rest of this thesis is organized as follows. Chapter 2 provides an extensive theoretical background, both so that the Random-LOS environment and test setup, as well as the design of the rectangular waveguide slot array feeds can be understood. Chapter 3 presents the methods used in WSAP and in CST. The chapter is organized so that the methods and underlying assumptions that was used in the preliminary study in WSAP are presented before the methods and assumptions that was used when designing the feeds in CST. In Chapter 4 are the results presented. Chapter 4 is organized such that the results from the preliminary study in WSAP are presented before the results that were obtained in CST. In Chapter 5, conclusions and interesting aspects of the results are highlighted and discussed. In addition, some suggestions for topics for future work are presented.

“”

2
Theory

2.1 Basic Electromagnetic Theory

In this Section will Maxwell's equations be introduced along with some other fundamental results that follows from the equations. The ultimate goal of this Section is to derive the propagation equations of the *electromagnetic* (EM) fields and one special solution to these equations. This solution represents so called plane wave propagation of the fields.

2.1.1 Maxwell's Equations

The behaviour of EM fields can fundamentally be understood from Maxwell's equations. Maxwell's equations is comprised of four coupled equations that can be presented in integral form or vector form. The vector representation of Maxwell's equations are given by the equations in (2.1) [21]

$$\nabla \times \vec{E} = -\frac{\partial \vec{B}}{\partial t} \ , \tag{2.1a}$$

$$\nabla \times \vec{H} = \vec{J} + \frac{\partial \vec{D}}{\partial t} \ , \tag{2.1b}$$

$$\nabla \cdot \vec{D} = \rho \ , \tag{2.1c}$$

$$\nabla \cdot \vec{B} = 0 \ , \tag{2.1d}$$

where $\vec{D}$, $\vec{B}$ is the electric- and magnetic flux density and $\vec{E}$, $\vec{H}$ is the electric- and magnetic field strength. Vectors $\vec{D}$ and $\vec{B}$ are related to $\vec{E}$ and $\vec{H}$ through a pair of equations known as the *constitutive relations* which are formulated in equation (2.2) [21]

$$\vec{D} = \epsilon_0 \epsilon_r \vec{E} = \epsilon \vec{E} \ , \tag{2.2a}$$

$$\vec{B} = \mu_0 \mu_r \vec{H} = \mu \vec{H} \ , \tag{2.2b}$$

where ϵ and μ is the permittivity and permeability. ϵ_0, μ_0 and ϵ_r, μ_r is the permittivity/permeability in free space and relative to free space.

Equation (2.1c) and (2.1d) are commonly referred to as *Gauss's law* and *Gauss's law for magnetism* [21]. Equation (2.1c) state that the electric net flux, i.e total inward or outward flow of the electric field, from a given surface is equal to the total charge, ρ, enclosed inside the surface [21],[22]. The other equation sates that the net flux of an magnetic field is zero [21].

Equation (2.1a) and (2.1b) links the electric and magnetic fields. Equation (2.1a) state that a circulating electric field will give rise to a time-varying magnetic field emerging from the area enclosed by the circulating field [21],[22]. Equation (2.1b) states analogously that a circulating magnetic field will give rise to a time-varying electric field together with a possible current density $\vec{J}$ [21],[22]. The current density, $\vec{J}$, represents movement of charge per unit volume and will hence appear in equation (2.1b) if the magnetic field is circulating an area where charges can be moved [21],[22]. The current density is given by equation (2.3) and can be represented by two different terms

$$\vec{J} = \vec{J}_{cond} + \vec{J}_{drift} \ . \tag{2.3}$$

The fist term, $\vec{J}_{cond}$, applies for conductive materials, while the second term, $\vec{J}_{drift}$, applies for other materials where charges can move [21]. The $\frac{\partial \vec{D}}{\partial t}$ term in equation (2.1b) is also referred to as a current (displacement current), but it requires no movement of charged particles to be sustained. An EM wave may therefore propagate in free space.

It is clear from the discussion in the previous paragraph that equations (2.1a) and (2.1b) governs the propagation of EM fields. This will be shown next.

2.1.2 The Wave Equation and the Plane Wave solution

Derivation of the propagating equation (also called the *wave equation*) assumes that the fields is propagating in a source-free medium, i.e. $\rho = 0$ and $\vec{J} = 0$ [21],[22]. Taking the curl on both side of (2.1a) yields the following expression that is shown in equation (2.4) [21],[22]

$$\vec{\nabla} \times \Big(\vec{\nabla} \times \vec{E}\Big) = -\vec{\nabla}^2 \vec{E} + \vec{\nabla}\Big(\vec{\nabla} \cdot \vec{E}\Big) = -\frac{\partial}{\partial t}\mu\Big(\vec{\nabla} \times \vec{H}\Big) \ . \tag{2.4}$$

The middle equivalence in (2.4) is obtained using the vector identity in equation (2.5) [21]

$$\vec{\nabla} \times \Big(\vec{\nabla} \times \vec{A}\Big) = -\vec{\nabla}^2 \vec{A} + \vec{\nabla}\Big(\vec{\nabla} \cdot \vec{A}\Big) \ . \tag{2.5}$$

In cartesian coordinates $\vec{\nabla}^2 = \frac{\partial^2}{\partial x^2} + \frac{\partial^2}{\partial y^2} + \frac{\partial^2}{\partial z^2}$ and $\vec{E} = \vec{E}_x + \vec{E}_y + \vec{E}_z = \hat{x}E_x + \hat{y}E_y + \hat{z}E_z$, where E_x,E_y,E_z is the complex amplitudes or field components of the $\vec{E}$-field in the x, y, z direction [22],[12]. The $\Big(\vec{\nabla} \cdot \vec{E}\Big)$ term in equation (2.5) will disappear due to the source-free assumption, $\vec{B}$ can be replaced with $\vec{H}$ using the constitutive relation in (2.2b) and $\vec{\nabla} \times \vec{H}$ can be substituted using equation (2.1b). These simplifications yields the expression shown in equation (2.6) [22]

$$\frac{\partial^2 \vec{E}_i}{\partial i^2} = \epsilon\mu \frac{\partial^2 \vec{E}_i}{\partial t^2} \ , \tag{2.6}$$

where $\frac{\partial^2 \vec{E}_i}{\partial i^2}$ and $\frac{\partial^2 \vec{E}_i}{\partial t^2}$ is a short-hand notation for the second order spatial- and time derivatives of the electric field, i.e. $i = x, y, z$ [23]. A propagating equation for the magnetic field vector can be derived analogously using equation (2.1b) as starting point. The final equation is given in equation (2.7) [21],[22]

$$\frac{\partial^2 \vec{H}_i}{\partial i^2} = \epsilon\mu \frac{\partial^2 \vec{H}_i}{\partial t^2} \ . \tag{2.7}$$

Equations (2.6) and (2.7) can be compared with the general formulation of the wave equation that is shown in equation (2.8) [23]

$$\frac{\partial^2 \vec{A}_i}{\partial i^2} = \frac{1}{v^2}\frac{\partial^2 \vec{A}_i}{\partial t^2} \ . \tag{2.8}$$

The variable v in equation (2.8) is the propagation velocity of the wave. A comparison between equation (2.6),(2.7) and (2.8) reveals that the speed of the EM wave must be equal to $v = \frac{1}{\sqrt{\epsilon\mu}}$, which is the speed of light [23].

The partial time-derivatives in equation (2.6) and (2.7) can be replaced with $j\omega$ if the fields are time-harmonic, i.e. varies with a sinusoidal time-reference [21],[22]. The wave equations in (2.6) and (2.7) can then be formulated according to equation (2.9)

$$\nabla^2 \vec{E} + \omega^2 \epsilon\mu \vec{E} = \nabla^2 \vec{E} + k^2 \vec{E} = 0 \ , \tag{2.9a}$$

$$\nabla^2 \vec{H} + \omega^2 \epsilon\mu \vec{H} = \nabla^2 \vec{H} + k^2 \vec{H} = 0 \ , \tag{2.9b}$$

where $k = \omega\sqrt{\epsilon\mu} = \frac{2\pi}{\lambda}$ is known as the free space *propagation constant* or *wave number*. The wave number accounts for the phase-advancement, i.e. propagation, of the fields. The formulation of the wave equations in (2.9) gives the additional insight that the propagation of time-harmonic fields depends on the frequency of the sinusoidal reference.

The equations in (2.9) can be solved analytically for a one dimensional case, i.e. $\frac{\partial}{\partial x} = \frac{\partial}{\partial y} = 0$. By convention is the wave assumed to depend on the z-coordinate. The solutions following this convention are expressed in equation (2.10) [22],[23]

$$\vec{E}_x = \hat{x} E_{0x} \cos\Big(\omega\Big(t - \frac{z}{c} + \phi_x\Big)\Big) \ , \tag{2.10a}$$

$$\vec{H}_y = \hat{y} H_{0y} \cos\Big(\omega\Big(t - \frac{z}{c} + \phi_y\Big)\Big) \ , \tag{2.10b}$$

where E_{0x} and H_{0y} are the amplitudes of the fields and ϕ_x and ϕ_y are the phases of the cosines. Equation (2.10) can be written in so-called *phasor-notation*, as shown in equation (2.11) [23]

$$\vec{E}_x = \hat{x} E_{0x} e^{j(\omega t - kz)} \ , \tag{2.11a}$$

$$\vec{H}_y = \hat{y} H_{0y} e^{j(\omega t - kz)} \ . \tag{2.11b}$$

The one dimensional solution of the wave equations in (2.10) represent plane wave propagation of the fields, which means that the field propagate in a single direction while the transverse components of the fields, i.e. E_x, H_x and E_y, H_y in this case, varies strictly in a plane perpendicular to the direction of propagation. The fields may have components along one or both unit vectors defining the plane. A complete description of the plane waves in (2.11) are formulated in equation (2.12)

$$\vec{E} = \vec{E}_t e^{(\omega t - jkz)} = [E_x \hat{x} + E_y \hat{y}] e^{j(\omega t - kz)} \ , \tag{2.12a}$$

$$\vec{H} = \frac{1}{\eta}\hat{z} \times \vec{E}_t e^{j(\omega t - kz)} \ , \tag{2.12b}$$

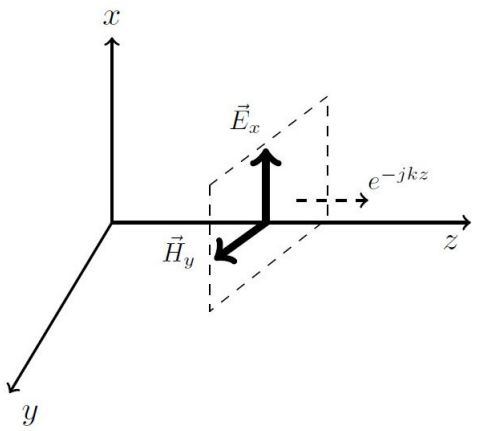

Figure 2.1: Depiction of a general plane wave. Note that the time-dependence, $\omega\ t$, of the wave is omitted.

where η is the wave impedance in free space. A plane wave is depicted in Figure 2.1.

2.1.3 The Wave Equation in a Conductive Medium

It has been assumed so far that the fields are propagating in a non conductive medium like free-space. The wave equations with the effect of sources included can be derived in the same manner as outlined in Section 2.1.2. It can then be shown that the solution to the one dimensional case will have the same form as in (2.11), but with the propagation $\gamma{=}\alpha{+}j\beta$ instead of k [22]. The two variables constituting γ account for different things. The first factor, α, accounts for propagation losses of the fields, while β assumes the role of k [22].

When the wave are propagating inside a medium with good conductive properties will the field be completely attenuated after a short distance of propagation [22],[12]. The so called depth of penetration or skin depth, δ_{skin}, is introduced to describe this distance. The skin depth corresponds to the propagation distance where the amplitude of the wave has been attenuated by a factor of $e^{-1} = 36.8\%$ after entering the medium. The skin-depth is hence defined as [22]:

$$\delta_{skin} = \frac{1}{\alpha} = \sqrt{\frac{2}{\omega\mu\sigma}}\ . \tag{2.13}$$

It can be concluded from equation (2.13) that $\delta_{skin} \Longrightarrow 0$ when $\sigma \Longrightarrow \infty$. A conductor with infinite conductivity is an ideal or *perfect* conductor. EM fields may therefore not penetrate a Perfect Electric conductor (PEC). Based on this insight must Maxwell's equations at the boundary of a PEC fulfill the following conditions [22]:

$$\hat{n} \times (\vec{E}_1 - \vec{E}_2) = \hat{n} \times \vec{E}_1 = 0\ , \tag{2.14a}$$

$$\hat{n} \times (\vec{H}_1 - \vec{H}_2) = \hat{n} \times \vec{H}_1 = \vec{J}_s\ , \tag{2.14b}$$

$$\hat{n} \cdot (\vec{E}_1 - \vec{E}_2) = \hat{n} \cdot \vec{E}_1 = \rho_s\ , \tag{2.14c}$$

$$\hat{n} \cdot (\vec{H}_1 - \vec{H}_2) = \hat{n} \cdot \vec{H}_1 = 0\ . \tag{2.14d}$$

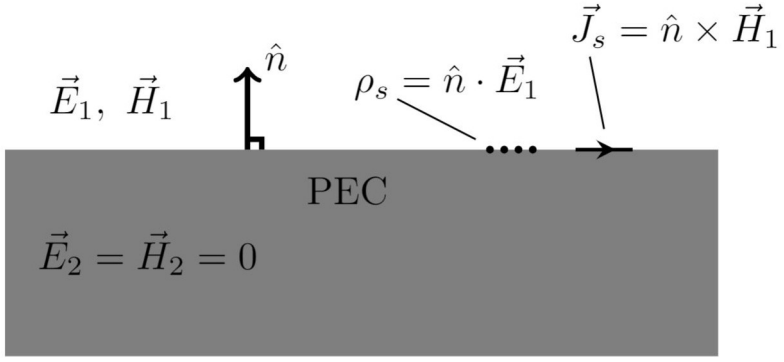

Figure 2.2: Illustration of the boundary conditions of at a PEC / non-PEC interface, where $\hat{n}$ is the surface normal of the PEC. The charge- and current densities induced on the PEC surface according to the boundary conditions are indicated.

The equations in (2.14) can be explained with the aid of Figure 2.2. The field inside the PEC is denoted with subscript 2 and the field in the non-PEC region is denoted with 1. The field inside the PEC is identically equal to zero due to zero skin-depth. A surface normal ($\vec{n}$) pointing outwards from the PEC is assumed. The operation of dot- and cross product is denoted by $\cdot$ and $\times$ in the equations. Equation (2.14c) and (2.14d) does hence represent the field components in the non-PEC region that are *normal* to the surface of the PEC, while (2.14a) and (2.14b) represents the components that are *tangential* to the surface.

Equation (2.14a) and (2.14d) show that the tangential $\vec{E}$-field and the normal $\vec{H}$-field in region 1 will disappear at the PEC boundary. Equation (2.14b) and (2.14c) show conversely that the tangential $\vec{H}$-field and the normal $\vec{E}$-field in region 1 induce charge, ρ_s, and current, $\vec{J}_s$, respectively at the PEC boundary. The subscript s implies that the induced charge (current) density only can reside at the very surface of the PEC.

A practical conductor with finite conductivity will have non-zero skin-depth. $\vec{E}_2 \neq 0$ and $\vec{H}_2 \neq 0$ must hence fulfilled at the boundary. The depth of penetration does however become very small for good conductors, i.e. for metals like copper, aluminum etc. at mm-wave frequencies [22]. The boundary condition in (2.14) may hence be used approximately for these materials [12]. The boundary conditions will become important when deriving the solution for the propagating fields in rectangular waveguide in Section 2.4.2

2.2 Antennas in pure-LOS and RIMP

The number of propagating plane waves, i.e. wave paths, between the transmitting and receiving antenna will be used to defined two environments called *LOS* and *RIMP*. An antenna will perform very differently in the two environments. The characteristics of antennas in pure-LOS and RIMP and how these environments can be emulated to test antennas is important for understanding the Random Line-of-Sight environment and test setup that has been developed.

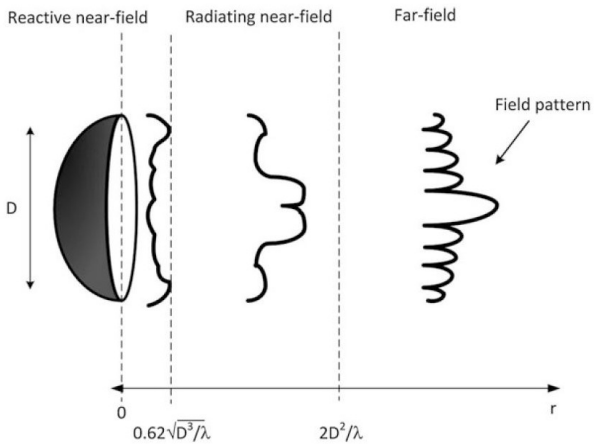

Figure 2.3: Illustration of the radiation regions of an antenna. The near-field region is divided into the reactive and radiating regions [9].

2.2.1 Antennas in pure-LOS

The LOS environment means that a Rx antenna receives EM waves from a Tx antenna through a direct propagating path [12],[8],[13]. In the LOS environment is the Rx antenna located in the *far-field region* with respect to the Tx antenna. In this region is the distance, $\mathbf{r}$, between the antennas large enough so that the waves revived by the Tx antenna is approximately planar [12],[8].The minimal distance from the transmitting side where this approximation is sufficiently accurate is commonly defined by the expression in equation (2.15) [12],[8]

$$\mathbf{r} = \frac{2D_a^2}{\lambda} \ , \tag{2.15}$$

where D_a is the diameter covering all radiating parts of the Tx antenna and λ is the wavelength of the propagating wave. The condition in equation (2.15) is not absolute and may vary in practical situations [12]. Radiated fields at distances smaller than (2.15) is called *near-fields* and this region is hence called the *near-field region* of the Tx antenna [12], [8]. A fundamental difference between the near-field and far-field region is that the variation of the radiated field in different directions stops to vary with the distance form the Tx antenna in the far-field region [8]. This is illustrated in Figure 2.3
Note that a third region within the near-field of the antenna is shown in Figure 2.3. The range of the reactive near-field region is usually within a few λ from the antenna [9]. The plane wave that is received on the Rx side is formulated in equation (2.16) [12]

$$\vec{E}(\mathbf{r}, t) = \frac{1}{r} e^{j(\omega t - kr)} \vec{G}(\mathbf{r}) \ , \tag{2.16a}$$

$$\vec{H}(\mathbf{r}, t) = \frac{1}{\eta} \hat{r} \times \vec{E}(\mathbf{r}, t) \ , \tag{2.16b}$$

where $G(\mathbf{r})$ is the *far-field function* that accounts for the fixed radiation pattern of the Tx antenna in the far-field region. The $\frac{1}{\mathbf{r}}$ term accounts for attenuation of the field due to propagation and $e^{(\omega t - jkr)}$ for the temporal and spatial advancement of the field. The

other variables in equation (2.16) are given in equation (2.17)

$$r = \sqrt{x^2 + y^2 + z^2} \ , \tag{2.17a}$$

$$\mathbf{r} = \hat{x}x + \hat{y}y + \hat{z}z \ , \tag{2.17b}$$

$$\hat{r} = \frac{\mathbf{r}}{r} \ , \tag{2.17c}$$

where r is a scalar representing the geometrical distance between the Tx antenna and the Rx with coordinates x, y, z. Equation (2.17) show that the received fields can be predicted at any given distance in the far-field region as long as $G(\mathbf{r})$ of the Tx antenna is known. $\mathbf{r}$ and $\hat{r}$ in (2.17) represents the vector between the Tx and Rx antenna and the unit vector of this direction.

It can be seen that the parameters in (2.17) are defined with the transmitting side as the geometrical origo. The origo is usually placed at some practical point like in the center of the radiating structure of the Tx antenna. This gives that the phase advancement of the fields in (2.17) is defined by this particular point. This point is consequently called the *phase reference point* of the antenna [12].

It is important to note that the fields in equation (2.16) usually are expressed in spherical coordinates. The so called *physical convention* of the spherical coordinate system, i.e. ϕ_{az} is the angle in azimuth and θ_{pol} is the polar angle, are typically used [12].

2.2.1.1 Linear polarization of a Plane Wave

The polarization of a planar wave describes how the transverse field components oscillates in the plane as the wave is propagating [22],[23]. The polarization of an EM wave is defined by the polarization of the $\vec{E}$-field [22]. The corresponding polarization of the $\vec{H}$-field can be determined from $\vec{E}$ as the electric and magnetic fields are orthogonal [12]. *Circular* polarization is defined as the transverse $\vec{E}$-field components traversing one full circle in the transverse plane as the plane wave is propagating one period. The polarization is instead called *linear* if the transverse components of $\vec{E}$ oscillates along a single direction in the plane [22]. If the field coincides with one of the unit vectors of the plane, i.e. $E_x = 0$, $E_y \neq 0$ or $E_y = 0$, $E_x \neq 0$, is the wave linearly polarized in the y-direction and x-direction, respectively [22]. Linear polarized antennas are usually refereed to as having *horizontal* or *vertical* polarization. For antennas that are extended along a single direction (a half-wave dipole for example, see Figure 2.4) does horizontal polarization mean that the length of the antenna is *parallel* to the ground surface, while vertical polarization means that the length of the antenna is *orthogonal* to the ground [12].

The notation *CO-polar* and *Cross-polar* is commonly use in the antenna community. The CO-polarization is simply the desired polarization of the antenna, while the Cross-polarization is the undesired polarization [12]. For example, a linear polarized antenna in the x-direction would have the CO-polarization in x and the Cross-polarization in y if plane wave propagation in z is assumed. Even more generally, if the antenna is vertically polarized would the CO-polarization be vertical and the Cross-polarization horizontal. The relative Cross-polar level (XP) of an antenna is the ratio between the Cross-polar component and the maximal CO-polar component of the antenna as expressed in equation (2.18) [12]

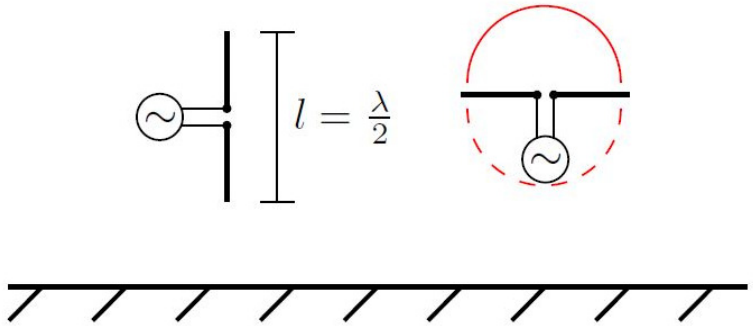

Figure 2.4: Illustration of vertical (left) and horizontal (right) linear polarization of a half-wave dipole antenna. The far-field radiation pattern of the half-wave dipole (drawn in read color) is also shown. Note that the drawn pattern only is intended to give a rough idea of what the actually pattern looks like.

$$XP = 10 \log_{10} \left(\left| \frac{E_{XP}}{E_{CO_{max}}} \right|^2 \right) , \tag{2.18}$$

where E_{XP} is the Cross-polar component and $E_{CO_{max}}$ is the maximal CO-polar component. An perfect linearly polarized antenna should provide a infinitely low XP [12]. The relative cross polar level can therefore be used to indicate the quality of polarization of these antennas in that the lower the XP is, the more linear is the polarization.

2.2.1.2 Antenna Radiation in pure-LOS

The far-field function in equation (2.16) is a function of the fixed spatial radiation of the antenna in the far-field region. A graphically representation of $G(\mathbf{r})$ is hence called the *radiation pattern* of the antenna [12]. Figure 2.5 shows the radiation pattern (ϕ_{az}= 0 ° cut) from an array antenna consisting of rectangular waveguide that was obtained using CST.

It is apparent from Figure 2.5 that the radiation has one major maximum and several minor maxima. The major maximum of the radiation pattern is called the *main-lobe* and the minor are called *sidelobes*. The direction of the main lobe is called the *boresight direction* [12]. It is generally desirable that the main lobe is considerably larger than the sidelobes. The reason for this is that high sidelobes may cause undesirable cross-talk in the system were the antenna is used [23].

The sidelobe closest to the main lobe is of particular interest since this lobe typically is the larges sidelobe. The *sidelobe level* (SLL) is defined as the difference between the level of the main lobe and the level of the closest sidelobe [12]. Since SLL is a relative measure can it conveniently be expressed in units of decibel. The unit for SLL is dBi, where i denotes that it is relative to an isotropic level. The radiation pattern is always normalized (usually to the level of the main lobe) [12]. The normalized radiation pattern shows the ability of the antenna to focus the radiation in different direction. This ability is known as the *gain* of the antenna [8]. A normalized radiation pattern is hence called the

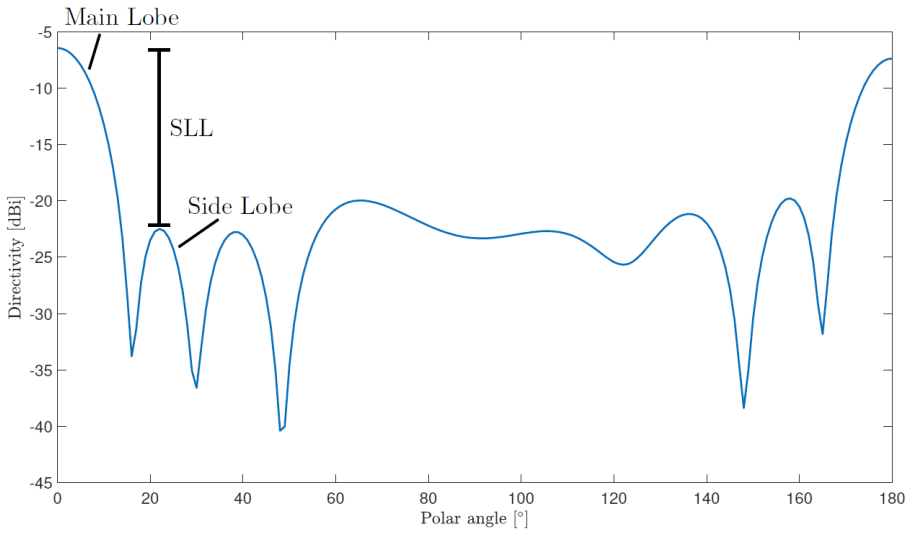

Figure 2.5: The radiation pattern of an array antenna in CST.

directive gain and the directive gain at the boresight directions is known as the *directivity* of the antenna [12],[23]. The directive gain and directivity is important characteristics of antennas in a LOS environment [8].

2.2.1.3 Emulation of the pure-LOS Environment

LOS typically assumes that the distance between the Tx and Rx antenna remains fixed [4]. The performance of an antenna in LOS can therefore be evaluated by receiving EM radiation from a source antenna located in the far-field region. Such measurement is performed at a *test range* [8]. The AUT is placed on a positioner and receives radiation from a source antenna at a distance that fulfills the far-field condition [8],[13]. The source antenna has well known characteristics, i.e. directive gain, polarization. The orientation in azimuth and elevation of the AUT is varied by the positioner so that the AUT scans the complete radiation pattern from the source antenna in discrete steps. A *vector network analyzer* (VNA) is connected to the ports of the source antenna and the AUT. The reason for this is that the radiation pattern can be obtained form the *transmission*, i.e. measured S_{21}, between the antennas [9]. The VNA can hence be used to calculate S_{21} for different positions of the AUT which yield the radiation pattern of the AUT. The measured radiation patter is normalized by the directive gain of the source antenna. [8]. In a test-range is the the AUT used as the Rx antenna. However, a consequence of Maxwell's equation being linear is that EM fields are *reciprocal*. This means that the response from the AUT is the same weather it is used as an Tx or Rx antenna [8],[22].

Antennas can be measured at test ranges located indoors or outdoors [13]. An indoor test range are commonly located in an AC to eliminate indirect wave patch between the Tx and Rx antenna [8],[13]. In an outdoor test range is the AUT (and sometimes also the source antenna) commonly mounted on a tower or similar to avoid reflections from the ground [13].

2.2.2 Antennas in RIMP - Multipath and Fading

Multipath means that there exist multiple propagation paths between the Tx and Rx antenna [12]. Multipath is the result of the transmitting waves deviating from the direct

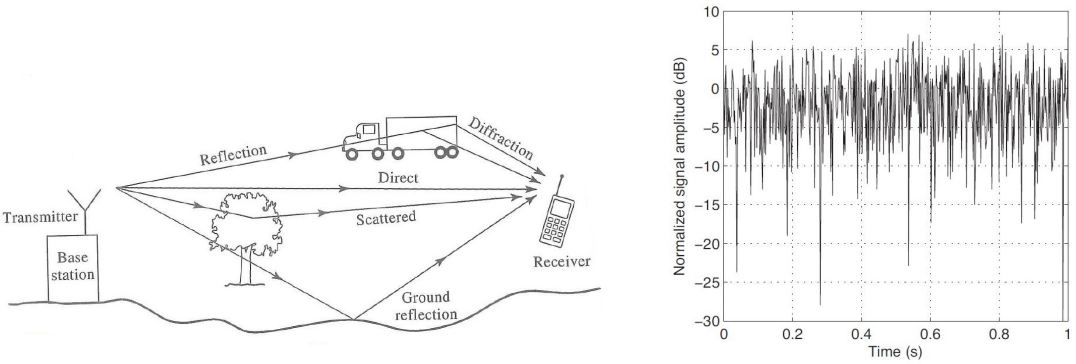

(a) (b)

Figure 2.6: (a) Illustration of different phenomena that may cause multipath in a real propagation environment [11]. (b) Illustration of a received signal undergoing fading [12].

path due to effects like reflection, diffraction and scattering [11]. These effects will occur in environments where many objects may obstruct the propagating wave such as dense urban areas and indoor areas [12], [11]. Figure 2.6(a) illustrate different phenomenon that may cause multipath in a propagation environment.

If the relative position between scatters and the antenna is changing, will the received waves start to add constructively or destructively such that the total received signal will vary stochastically over time. Such received signal is said to undergo *fading* [11]. Fading may also occur in situations where the relative position between the Tx and Rx antenna is changing, i.e. the Tx, Rx or both antennas are is used in a movable application [12]. Figure 2.6(b) shows an example of a fading signal.

A signal that undergoes fading may become so weak at the points of destructive interference that it can not be detected at these instances [11]. Fading is however useful when one want to take advantage of diversity and multiplexing (see Section 2.3.1), as the fading itself yields independency of the transmitted data streams. In LOS can this only be achieved by using different polarizations [9].

The adjectives *slow* and *fast* is used to characterize the fading. If the received signal amplitude varies strongly with small changes in relative position between the Tx and Rx antenna (or between the antennas and scattering sources) is the fading fast, otherwise it is slow. The fading may also be characterized as fast (slow) if the signal amplitude varies strongly (weakly) during very short periods of time [11].

2.2.2.1 The RIMP Environment

RIMP is an environment in which antennas are communicating in the far-field region but in a ideal fading environment without direct LOS [14], [13]. RIMP stands for *Rich Isotropic Multipath*. Rich means that a large number of plane waves with independent amplitude, phase and polarization are incident on the antenna due to the multipath. [12],[13]. Isotropic means that the AoA of the plane waves are uniformly distributed. This means that the plane waves incident on the antenna are equally likely to come from any direction. The directive gain of an antenna in RIMP is therefore not relevant [10],[15]. The receiving situation of an antenna located in RIMP is illustrated in Figure 2.7.

In real fading environments is the AoA never completely uniformly distributed and the polarization is not truly random [15],[16]. RIMP is therefore said to represent an

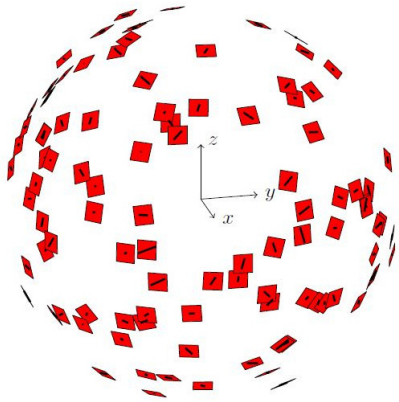

Figure 2.7: Illustration of the RIMP environment. The antenna is located in the middle of the coordinate system. A large number of incident plane waves (the red patches) with random amplitude and phase is shown. The AoA of the plane waves can be seen to be uniformly distributed. The polarization of each plane waves are indicated as a line on the red patch. It can be seen that the polarization vary randomly. [14].

ideal fading environment. Fading in real-life environments will always be less severe than in RIMP [12],[13].In some real situations is RIMP however a good approximation. A large number of mobile phones communicating with a base station in a dense urban area or indoors environments is such examples [13]. RIMP is therefore used as a reference environment for antennas operating in real fading environments [13],[12]. The RIMP environment can be emulated in the RC [12],[13],[10].

2.2.2.2 Emulation of the RIMP Environment

The RC (see Fig. 2.8) is a cavity resonator, i.e. a hollow box with flat metallic walls, that supports a large number of modes at the operating frequency of the antenna [13]. Each mode inside the resonator consist of eight plane waves, which mean that the number of plane waves inside the chamber will be sufficiently large to emulate a RIMP environment [12],[25].

Various mechanism is employed to ensure that plane waves will have random amplitude, phase and polarization and that the AoA will be uniformly distributed. One such mechanism involves metallic plates that are moved in discrete steps inside the chamber. The plates changes the boundary condition inside the chamber so that a new number of modes are supported by the chamber. Each new position of the plates does ensure that a new set of plane waves continuously are generated inside the chamber, which in turn ensures that the AUT will receives plane waves with random amplitude and phase in a statistical sense and that the AoA will be uniformly distributed [12]. The AUT is also place on a turntable which rotates as the plates are moving. The rotation will ensure that the antenna will look in different directions in the azimuth plane during measurement which will eliminates any direct contributions of the chamber antenna (see below) where the AoA is deterministic [12].

Inside the chamber is also three antennas with orthogonal linear polarization mounted on the walls. These antennas make up the chamber antenna. The chamber antenna and the AUT are connected to a VNA. The transmission between the AUT and the chamber antenna is successively measured for each new position of the plates, which ensure that the AUT receives plane waves with randomly varying polarization in a statistical sense

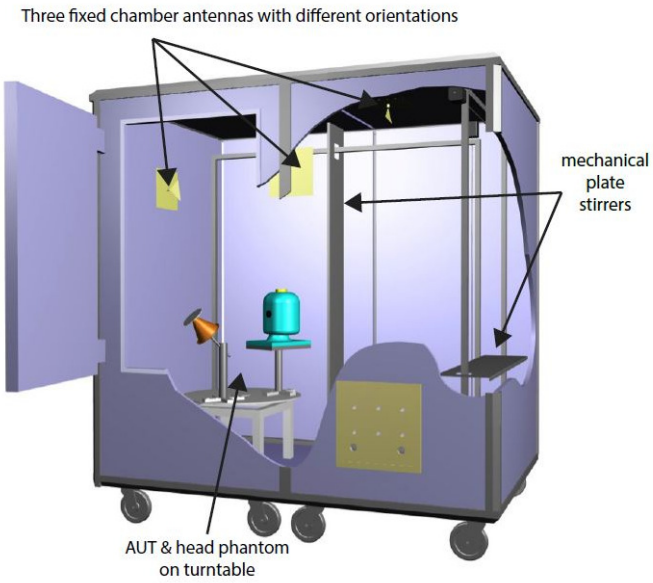

Figure 2.8: Illustration of a Reverberation chamber used to emulate the RIMP environment [12].

[12],[13]. The measurements between the AUT and chamber antenna are used to derive different characteristics of the antenna that is relevant in RIMP [12]. These characteristics will not be accounted for.

2.3 Antennas in Random-LOS

The Random-LOS represents an environment where a LOS-component exist but the polarization and the AoA of the received plane wave varies randomly [14],[5],[7].The Random-LOS environment is relevant in situations where the relative position between the Tx and Rx antenna is changing [14],[4]. There will typically exist multiple movable antennas, i.e. users, on the Tx side, Rx side or on both sides. In many real-life situations however there will be only multiple users on one side, while a single fixed antenna exist on the other side, i.e. a base station serving multiple users [14],[10]. It is the unpredictable behaviour of the users, i.e. the changing position, that introduce the random features of the plane waves, while the LOS-component exists because the user typically will see the base station and there will be a direct path between the base station and the user.

Random-LOS can be divided in two different cases, the 2D and 3D case [14],[13]. The 3D case applies for antennas used in handheld devices like smart phones and tablets [14],[2]. A handheld device can be oriented arbitrarily by the user. A base station will therefore receive signals from the device that are randomly linearly polarized [13],[5],[7]. Conversely, the linear polarized antenna inside the device can be orientated in any direction relative to a base station by the user and will thus receive signals that are randomly linear polarized.

A base station communicating with an antenna mounted on a vehicle may receive signals mainly from any direction in the horizontal plane. Because the vehicle is mainly moving around in the horizontal plane, with some slight elevation angles, can the overall situation however be approximated as a 2D case [5],[7]. The same approximation also applies in the opposite direction, i.e. for a vehicle antenna that receives signals from the base station [13],[7]. Since the vehicle antenna is limited to the horizontal plane, will the

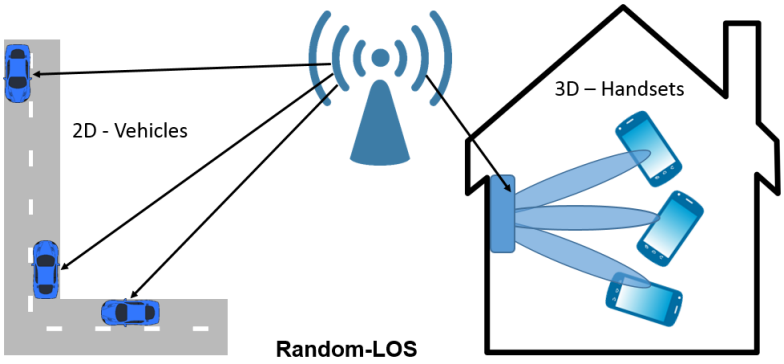

Figure 2.9: Illustration of 2D (left) and 3D (right) Random-LOS [13].

polarization vary much less than for a handheld device. The 2D case of Random-LOS is therefore defined as only the AoA being random [2],[3]. Figure 2.9 illustrates the 3D and 2D case of Random-LOS.

Before the introduction of Random-LOS was the pure-LOS and the RIMP environments introduced. In pure-LOS will a direct wave path exist, while a large number of paths will exist in RIMP. Pure-LOS and RIMP are known as *edge environments* because they describe two ideal environments on opposite ends, i.e. between containing few scattering objects yielding a direct path and containing multiple scattering objects yielding multiple paths. A real-life propagation environment will always contain an unknown number of scattering objects and will be somewhere between pure-LOS and RIMP [5],[7]. To make an accurate prediction of how an antenna will perform in a real-life environment is generally hard due to the many unknown scatters may effect the performance [5]. It would therefore be useful if it was possible to make an accurate prediction based on how the antenna is performing in pure-LOS and in RIMP since these environments are well established and can be emulated. In order to simplify testing of antennas has an hypothesis been developed alongside the Random-LOS environment. The hypothesis is formulated accordingly [10]:

> *If an antenna performs well in both RIMP and pure-LOS will it also, statistically speaking, perform well in all real-life environments and situations.*

In movable applications will the antenna be subjected to fading. The fading may be slow or fast depending on the environment. If the environment ideally contains no scattering objects would the fading be very slow and if the environment conversely contains many scatters would the fading be fast. The edge environments for a antenna used in movable applications would hence be Random-LOS and RIMP [5],[7]. These edge environments are illustrated in Figure 2.10 for a vehicular application. It can be seen that the vehicles is moving both in an RIMP like environment, i.e the urban area indicated by the buildings, as well as in an Random-LOS environment, i.e the open road with no surrounding building.

An identical hypothesis that includes RIMP and Random-LOS has also been formulated [5],[10],[15]. The hypothesis was formulated in order to meet the future needs of reliable and simple testing of vehicular antennas [13],[10],[15]. The hypothesis has not yet

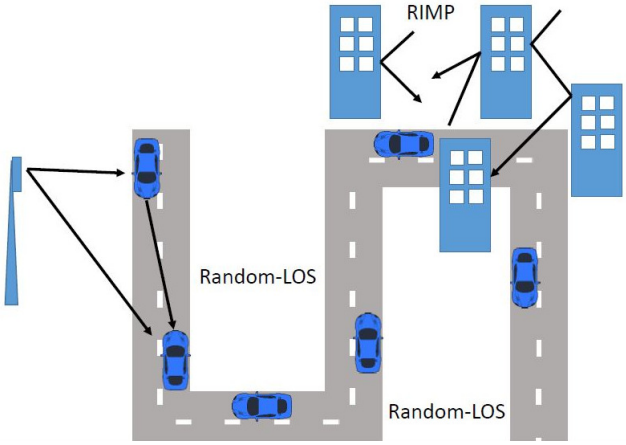

Figure 2.10: Illustration of the two edge-environments for vehicular antennas [2].

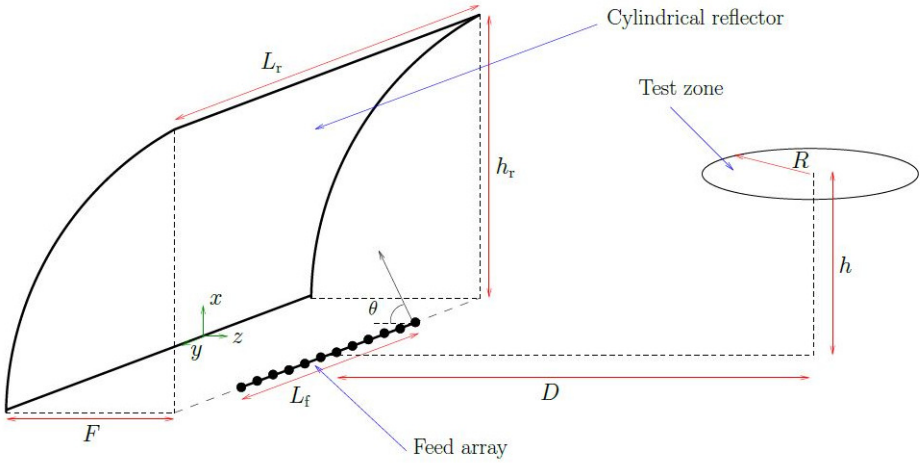

Figure 2.11: Schematic of the 2D Random-LOS test setup viewed from the side [4]. A circular test zone with the radius R is placed at a height h and distance D from the reflector/linear feed providing the AUT located in the center of the test zone with plane wave illumination. The linear feed that illuminates the reflector is L_f long and is located at the focal distance F of the reflector. The linear feed is slanted from the yz-plane with the angle θ_{feed}. The effective height and width of the reflector are given by h_r and L_r respectively. The length of the linear feed can be expressed as L_f=Nd, where N is the number of antenna elements and d is the spacing between the elements.

been proven but is nonetheless important as it has been used as a working hypothesis for the development of the Random-LOS test setup. [13],[15]. Section 2.3.1 will be dedicated to the test setup that emulates the Random-LOS environment.

2.3.1 The Random-LOS Test Setup

If the performance of a vehicular antenna should be evaluated using the 2D Random-LOS environment, then it needs to be emulated somehow. A setup that emulates this environment should produce a plane wave illumination of the AUT as well as provide random AoA in the horizontal plane.

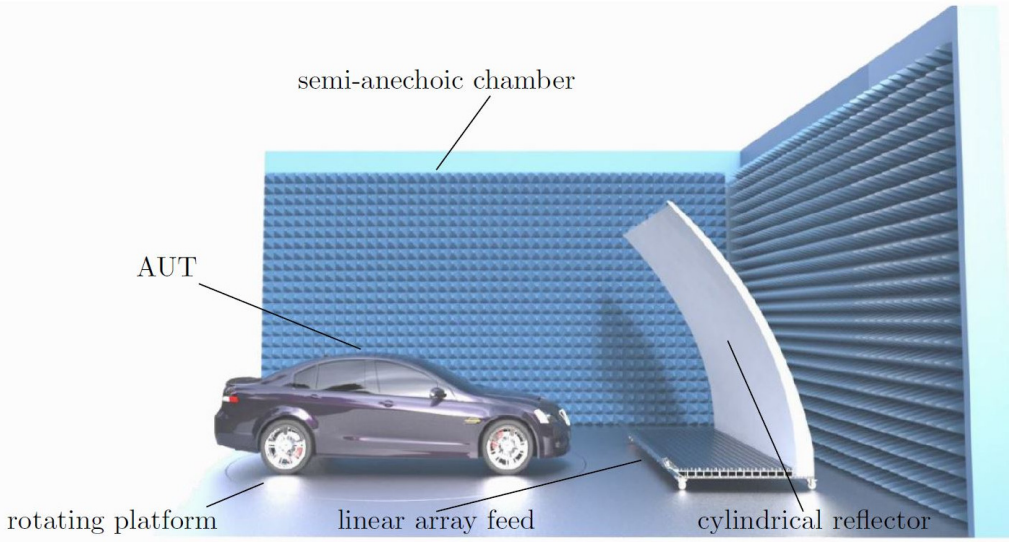

Figure 2.12: An artistic illustration of the final 2D Random-LOS test setup [13].

Figure 2.11 shows a schematic of the Random-LOS test setup and Figure 2.12 shows an illustration of what the final setup may look like when it has been implemented. The position of the AUT can be seen in Figure 2.11 to be located a distance D from a linear feed array that feeds the cylindrical reflector.The linear feed array act as the chamber antenna and illuminate the AUT via the reflector during testing [4],[17]. The array is placed along the focal line of the reflector [4]. The AUT is also seen to be located at a height h from the floor of the room where the testing is performed. This height is considered since the AUT will be located at some distance above the floor depending on where the AUT is mounted on the vehicle [4],[15],[16]. The AUT is commonly mounted on the roof of the vehicle (see Figure 2.12), which corresponds to a height of approximately h= 1.5-1.8 m [13].

In Figure 2.12 can it also be seen that absorbing materials will be covering the walls of the test room to ensure a direct propagating path between the AUT and the chamber antenna. Unlike a regular AC can it be seen that no absorbent material covers the floor. The test room shown in Figure 2.12 is therefore called a *semi*-AC [13]. It should be noted that an regular AC chamber also may be used. However, testing of vehicular antennas are more commonly performed in semi-AC [9],[8].

The vehicle is placed on a turntable in front of the linear array. The turntable rotates the vehicle during testing so that the AUT is illuminated from any direction in the horizontal plane. This will provide random AoA [15],[16],[17].

The actually plane wave illumination is provided by the reflector [4],[17]. The plane wave illumination of the AUT could also be achieved in a traditional antenna test range. The far-field distance given by equation (2.15) may however become very large at mm-wave frequencies. Large test-ranges would naturally be more expensive. The reflector solutions is therefore preferred [15],[17]. The reflector's role in achieving plane wave illumination can be understood as follows. The spherical wave fronts radiated from the elements in the linear array feed are collimated by the reflector to planar wave fronts. The plane wave will then be created close to the reflector in the near-field region of the linear array. This corresponds to the reflector transforming the near-field radiation of the feed array into the far-field region. [13],[8]. A test ranges that utilizes a reflector is called a *compact* test range due to the shorter range that is needed in order to reach the far-field region of the

chamber antenna. [8],[26].

In order to evaluate the performance of the AUT is a RBS (also know as a *communication tester*) connected to the array via a beamforming network. The communication tester emulates a real base station [13]. The beamforming network is used to excite the individual element of the array with the signals from the communication tester [13]. A modern system that operates in a fading environment usually employs several antennas at the Tx side, Rx side or on both sides to mitigate the fading. This is known as *antenna diversity* [12],[14]. Different signal processing algorithms can be implemented in the software of the diversity antenna. These algorithm require that at least two independent signals are employed [12]. In order to evaluate diversity performance of the AUT should the array be design for two orthogonal polarizations which allow two independent signals to be transmitted [14],[17]. With two orthogonal polarizations can multiple data streams also be transmitted simultaneously, which allow for more data to be send between the RBS and the AUT, i.e. a larger system throughput. Transmitting multiple data stream over a single communication channel, i.e. between the source antenna and the AUT, is known as *multiplexing* [14].

2.3.2 The Test Zone

It was stated in Section 2.3.1 that the wave fronts leaving the surface of the reflector will be planar. The finite diameter of a practical reflector does however make it impossible to obtain a perfectly planar wave front [26]. Some limit of what is considered as an acceptable quality of the collimated waves must therefore be determined. The so called *quiet-zone* is the area in front of the reflector where a planar wave is generated with acceptable quality [26]. When referring to the Random-LOS test setup is the quiet zone also called the *test zone* [13],[4],[16]. To adhere to this convention will this word only be used from here. In the Random-LOS test setup should the test zone coincide with the location of the AUT [4]. It can be seen in Figure 2.11 that a circular shape of the test zone is considered. The size of the test zone is determined by the radius R. A circular test zone is considered due to the rotation of the AUT that is caused by the turntable [4]. The planar field received by the AUT must be of acceptable quality independent on how the AUT is rotated relative to the liner feed and the reflector. The concept of a test zone thus becomes meaningful to use for the Random-LOS test setup [13] [16],[17].

The discussion in the previous paragraph has implied that the planar wave quality of the collimated field can be evaluated. The radiation from the linear array that is collimated by the reflector must therefore be measured in some way. This can be done by sample the field in front of the reflector at fixed positions using a half-wave dipole [13],[15],[16]. A half-wave dipole is suitable for probing due to it its radiation pattern being close to isotropic in the the directions orthogonal to the extension of the dipole, see Section 2.4) [27],[9]. The advantages of this is that the dipole then will measure the field equally well in any direction in the plane where the field is sampled [8]. Note that the half-wave dipole will be presented in Section 2.4.3.1.

Assume now that a the position of the sampling dipole in front of the reflector is given by the position vector $\mathbf{r}$. If the reflector are illuminated by a linear array consisting of N antenna elements and each element is given by the positional vector $\mathbf{r_n}$, will the total $\vec{E}$-field measured by the dipole at $\mathbf{r}$ be given by equation (2.19) [15],[16]

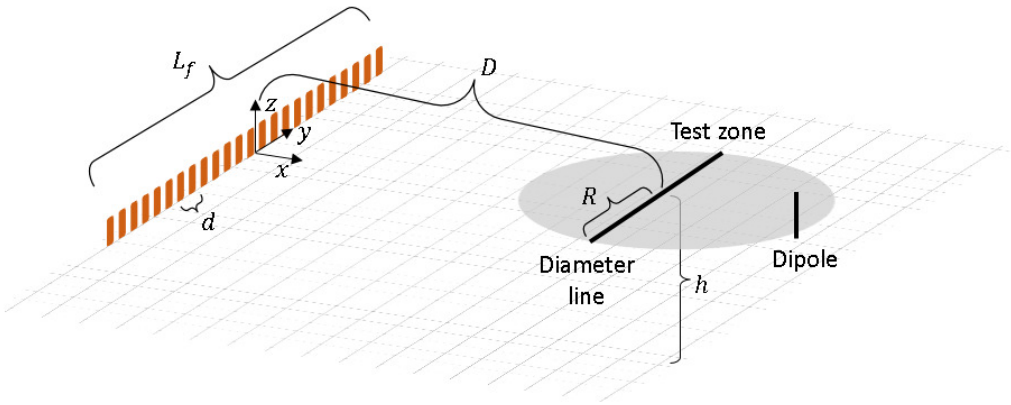

Figure 2.13: Sampling of the field within the test zone using a half-wave dipole [13]. The elements of the linear array contributing to the total field in the test zone are also indicated. Note that the simplifying conditions is assumed in the figure, see Section 1.1. For that reason is the reflector not displayed in the figure.

$$\vec{E}_{tot}(\hat{r}_n) = \sum_{n=1}^{N} G(\hat{r}_n) \frac{e^{-jk|\mathbf{r}-\mathbf{r_n}|}}{|\mathbf{r}-\mathbf{r_n}|} \ . \tag{2.19}$$

The variable $G(\hat{r}_n)$ in equation (2.19) is the far-field function of the n^{th} antenna element in the array. The factor $|\mathbf{r}-\mathbf{r_n}|$ is the distance between the n^{th} antenna element and the dipole. $\vec{E}_{tot}$ in equation (2.19) is a function of $\hat{r}_n = \frac{(\mathbf{r}-\mathbf{r_n})}{|\mathbf{r}-\mathbf{r_n}|}$, which is the phase reference point of the n^{th} antenna element. Note that the corresponding $\vec{H}$-field from each antenna element is obtained from the relation in (2.16b).

Equation (2.19) implies that each antenna element contributes to the total field that is measured at a the dipole. This is known as the *superposition principle* and is ultimately a result of Maxwell's equations being linear [15],[8]. This means in turn that the desired size and location of the test zone can be controlled by the number of antenna elements that are used in the linear array. In order to evaluate the test zone for a given linear feed is the field sampled according to Figure 2.13. Note that free space is assumed in the figure as only a linear array without a reflector is shown.

Figure 2.13 illustrate the collection of field samples within the test zone using a half-wave dipole. The origo of the test zone coincides with $x = D$, $y = 0$, and $z = h$. The variables D, R and h in Figure 2.13 is the same variables as shown in Figure 2.11. The dipole can be seen to be orientated orthogonal to the sample plane for reasons explained in the previous paragraph. The spacing between the elements is d and the length of the array is given by $L_f = Nd$ (see Figure 2.11). The variable d will be discussed again briefly in Section 2.4.4 when defining the minimum element spacing to avoid grating lobes. The diameter of the test zone is indicated in Figure 2.13. The meaning of the this line with regards the planar quality of the fields within the test zone will be explained shortly. The collected field samples are used to calculate two FoM, which are used to evaluate the planar quality [13]. The first FoM is called the *Power spread* and is defined in equation (2.20) [13]

$$\sigma_{dB} = 5\log_{10}\left(\frac{1+\sigma}{1-\sigma}\right) , \tag{2.20}$$

where σ_{dB} and σ is the *standard deviation* of all field samples collected within the test zone in units of dB and in linear units, respectively. The standard deviation in linear units is given by equation (2.21) [13]

$$\sigma = \sqrt{Var\left[\frac{P_{samp}}{Mean(P_{samp})}\right]} = \sqrt{Var[P_{norm}]} , \tag{2.21}$$

where P_{samp} denotes the power of one field sample. The power sample is defined by equation (2.22) [13]

$$P_{samp} = \left|\sum_{i=1}^{N} \vec{E}_n(\hat{r})\right|^2 , \tag{2.22}$$

where the summation is taken over all N antenna elements at the position of the dipole. $Var[\cdot]$ and $Mean(\cdot)$ in (2.21) denoted the operation of calculating the variance and mean, respectively. The second FoM is called the *phase spread*. The phase spread is given by equation (2.23) [13]

$$\Delta\phi_{max} = max\Big|\phi_{samp} - Mean(\phi_{samp})\Big| = max\Big|\phi_{norm}\Big| , \tag{2.23}$$

where ϕ_{samp} is the phase of one field sample collected along the diameter of the test zone that is shown in Figure 2.13. Note that the variables P_{norm} and ϕ_{norm} are introduce to denote the normalized field samples within the test zone [13]. The reason why the phase is evaluated along the diameter of the test zone and not over the whole test zone can be explained accordingly; the phase of the plane wave advance along the test zone with e^{-jkr}, while the phase ideally is constant across the test zone. The direction along (across) the test zone is seen to be in the x (y)-direction in Figure 2.13. The phase varies with 2π between consecutive wave fronts. At mm-frequencies can a large number of wave fronts fit inside a normal-sized test zone. The mean phase in (2.23) would then average out to zero yielding a large value of $\Delta\phi_{max}$ that don't represents the phase spread. ϕ_{samp} in equation (2.23) is defined in equation (2.24) [13]

$$\phi_{samp} = arg\Big(\sum_{n=1}^{N} \vec{E}_n(\hat{r})\Big) , \tag{2.24}$$

where the summation is taken over all N antenna elements of the linear feed. $arg(\cdot)$ in (2.24) is the argument of a complex number. The FoM's in (2.20) and (2.24) are used to evaluate the variation of the generated planar wave inside the test zone; the first FoM measure the variation of power and the second measure the phase variation [13]. The wave fronts corresponding to an ideal planar wave has constant amplitude and phase [8], which corresponds to zero power- and phase spread. The planar waves obtained in a indoors compact range chamber will typically achieve a power spread of 1 dB and a phase spread of 10 ° within the test zone [8].

2.4 The Rectangular Slot Array Antenna

The linear feed array used in the 2D Random-LOS setup will be implemented as a slot array antenna. The slot array antenna that will be considered rely on a rectangular

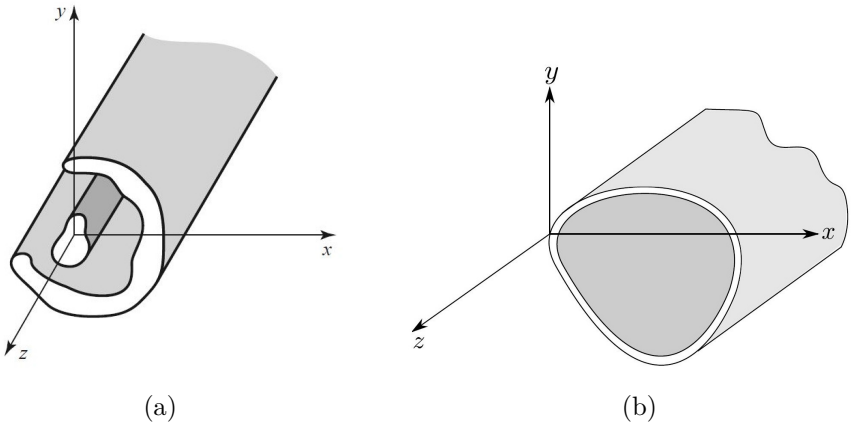

Figure 2.14: Illustration of generic transmission lines extended along the z-axis. (a) A transmission line with two conductors [22]. (b) A single conductor transmission line or a waveguide [29].

waveguide. The rectangular waveguide is a robust construction with good power handling capabilities [23],[9]. Rectangular waveguides supporting frequencies between a few GHz up to hundreds of GHz are available commercially [22],[9]. The slot array itself is simple in its structure making it relatively cheap to manufacture [9],[28]. The array can also be designed for vertical and horizontal linear polarization which allow for larger throughput and for testing of diversity performance and multiplexing in the test setup. First will some basic concepts of transmission lines be introduced. A presentation of the rectangular waveguide will then follow. The understanding of the slot array relies on a thorough analysis of the properties of a single slot in the waveguide. Such analysis will therefore be given followed by a review of the slotted array antenna and the required steps that are needed in order to design the array antenna for vertical and horizontal polarization.

2.4.1 EM Propagation in Transmission Lines

A transmission line is a structure consisting of one or several conductors that can guide EM fields [22],[29]. A transmission line comprised of a single conductor, i.e. a metallic tube, is commonly known as a waveguide [29]. A depiction of a generic transmission line of one and two conductors are shown in Figure 2.14.

The transmission line shown in Figure 2.14(a) allow EM propagation when a source signal is connected to the conductors due to the fields that arise between the conductors [22]. The fields propagating in this waveguide will have components limited to a plane transverse to the extension of the conductors, i.e. the propagation direction. Besides the transverse components may the propagating fields also have components along the propagation direction. [22],[29].

The guiding of EM fields in the waveguide that is shown in Figure 2.14(b) rely on the fields being reflected between the inner walls of the guide with small losses [22],[29]. The propagating field inside this type of waveguide must have at least one component along the extension of the guide [22]. The discussion so far has suggested that different types of waves can be sustained by transmission lines. These are the *transverse electromagnetic* (TEM), *transverse electric* (TE) and *transverse magnetic* (TM) waves [22],[29].

A transverse electric wave is defined as $E_z = 0$ and $H_z = 0$. The plane wave discussed in Section 2.1.2 is a transverseelectric wave [29]. The propagation of a TEM wave requires a transmission line consisting of at least two conductors.

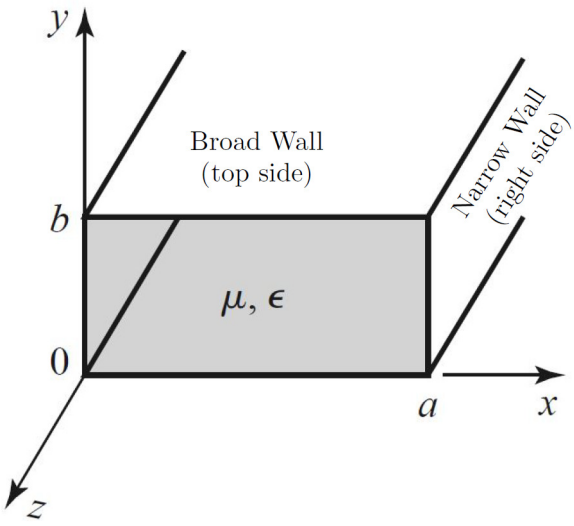

Figure 2.15: The geometry of a rectangular waveguide [22]. Note that the naming of the waveguide walls has been added to the original Figure.

The TE and TM wave are defined as $E_z = 0$, $H_z \neq 0$ and $E_z \neq 0$, $H_z = 0$, respectively. TM and TEM waves can only be supported by waveguides [22].

2.4.2 Rectangular Waveguides

The geometry of a rectangular waveguide is shown in Figure 2.15. The geometry depicted in the figure will be assumed from here. The fields corresponding to a TE or TEM wave can generally be expressed according to the equations in (2.25) [22]

$$\vec{E} = [\vec{E}_t + \hat{z}E_z]e^{j(\omega t - \beta_{mn} z)} \,, \tag{2.25a}$$

$$\vec{H} = [\vec{H}_t + \hat{z}H_z]e^{j(\omega t - \beta_{mn} z)} \,, \tag{2.25b}$$

where $\vec{E}_t = E_x\hat{x} + E_y\hat{y}$ and $\vec{H}_t = H_x\hat{x} + H_y\hat{y}$ are the transverse components of the fields and $\beta_{mn} = \sqrt{k^2 - k_c^2}$ is the constant accounting for the phase advancement of the field. The variable k_c is known as the *cut-off* wave number. Note that the propagation constant, γ, in equation (2.25) is assumed to be lossless, i.e. $\gamma = j\beta$. The transverse components can be expressed as a function of E_z and H_z using (2.1a) and (2.1b) from Maxwell's equations [22]. The transverse components are expressed in equation (2.26)

$$E_x = \frac{-j}{k_c^2}\left(\beta_{mn}\frac{E_z}{\partial y} + \omega\mu\frac{\partial H_z}{\partial x}\right) \,, \tag{2.26a}$$

$$E_y = \frac{j}{k_c^2}\left(-\beta_{mn}\frac{E_z}{\partial y} + \omega\mu\frac{\partial H_z}{\partial x}\right) \,, \tag{2.26b}$$

$$H_x = \frac{j}{k_c^2}\left(\omega\epsilon\frac{E_z}{\partial y} - \beta_{mn}\frac{\partial H_z}{\partial x}\right) \,, \tag{2.26c}$$

$$H_y = \frac{-j}{k_c^2}\left(\omega\epsilon\frac{E_z}{\partial y} + \beta_{mn}\frac{\partial H_z}{\partial x}\right) \,, \tag{2.26d}$$

For a propagating TE wave is $E_z = 0$ and $H_z \neq 0$. The propagation of the TE wave can hence be derived by solving equation (2.9b) and applying the boundary condition in equation (2.14) at the waveguide walls [22],[23]. H_z in equation (2.25b) depends on the transverse coordinates only. The wave equation in (2.9b) is therefore reduce to a two dimensional case which is expressed in equation (2.27)

$$\left(\nabla_t^2 + k_c^2\right)\vec{H}_z = 0 \ , \tag{2.27}$$

where ${\nabla_t}^2 = \frac{\partial^2}{\partial x^2} + \frac{\partial^2}{\partial y^2}$. The solution to equation (2.27) is shown in equation (2.28) [22],[23]

$$H_z = A_{mn}\ cos(k_x x)\ cos(k_y y)\ e^{j(\omega t - \beta_{mn} z)} \ , \tag{2.28}$$

where $k_x = \frac{m\pi}{a}$ and $k_x = \frac{n\pi}{b}$ are the wave numbers of the field in the x- and y-direction, respectively. The variables m and n are nonnegative integers, while a and b are the dimensions of the waveguide in accordance with Figure 2.15. The format of the wave numbers implies that a TE wave can assume different distributions inside the waveguide. Each set of the integers m, n represents one distribution or *mode* and are a solution to the wave equation in (2.9b) [22],[23]. Equation (2.28) implies that the amplitude as well as the propagation is dependent on the mode. The corresponding transverse components of the TE wave can be obtained from the equations in (2.26) and are expressed in equation (2.29) [22]

$$E_x = \frac{j\omega\mu k_y}{k_c^2}\ A_{mn}\ cos(k_x x)\ sin(k_y y)\ e^{j(\omega t - \beta_{mn} z)} \ , \tag{2.29a}$$

$$E_y = \frac{-j\omega\mu k_x}{k_c^2}\ A_{mn}\ sin(k_x x)\ cos(k_y y)\ e^{j(\omega t - \beta_{mn} z)} \ , \tag{2.29b}$$

$$H_x = \frac{j\beta_{mn} k_x}{k_c^2}\ A_{mn}\ sin(k_x x)\ cos(k_y y)\ e^{j(\omega t - \beta_{mn} z)} \ , \tag{2.29c}$$

$$H_y = \frac{j\beta_{mn} k_y}{k_c^2}\ A_{mn}\ cos(k_x x)\ sin(k_y y)\ e^{j(\omega t - \beta_{mn} z)} \ . \tag{2.29d}$$

The field solution for the TM wave can be derived analogously by solving (2.9a) for E_z in equation (2.25a). The solution is given by equation (2.30) [22]

$$E_z = A_{mn}\ sin(k_x x)\ sin(k_y y)\ e^{j(\omega t - \beta_{mn} z)} \ . \tag{2.30}$$

For $k < k_c$ is the propagation constant imaginary and the propagation factor, $e^{-j\beta_{mn}}$, of the wave becomes real-valued [22],[29]. The wave will then be attenuated, which implies that the TE or TM wave cannot propagate as a certain mode for values of the wave number below k_c. The wave number is a function of frequency, so an equivalent statement is that modes cannot be sustained inside the waveguide for frequencies below a certain *cut-off frequency* f_c [29]. The cut-off frequency for TE and TM waves are given by equation (2.31) [22]

$$f_c = \frac{k_c}{2\pi c} = \frac{c_0}{2\pi\sqrt{\epsilon_r \mu_r}} \sqrt{\left(\frac{m\ \pi}{a}\right)^2 + \left(\frac{n\ \pi}{b}\right)^2} \ , \tag{2.31}$$

where c_0 is the speed of light in vacuum. It can be seen that the cut-off frequency is a function of the geometry as well as the material, i.e. ϵ_r and μ_r, filling the waveguide.

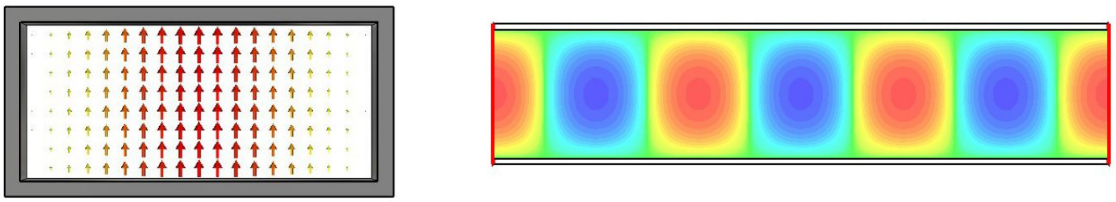

(a) (b)

Figure 2.16: The TE_{10} mode of a rectangular waveguide [29]. (a) The E_y component in the xy-direction. (b) The E_y component in the xz-direction plotted for constant values of z. The cos variation of E_y in the z-direction is apparent.

Two sine functions appear in (2.30). The lowest TM mode that yield $E_z \neq 0$ and hence a propagating wave must therefore be TM_11. For the TE wave can both the TE_{01} and TE_{10} mode exist, but since $a>b$ is assumed (see Figure 2.15) is TE_{10} the lowest mode. This mode is also the overall lowest mode in a rectangular waveguide [22]. It is important to note that the TE or TM wave will propagate as their respectively lowest modes for all frequencies above f_c and below the cut-off frequency of the second lowest mode given by (2.31). For higher frequencies will the field distribution inside the waveguide be a superposition of all modes that can be sustained at the frequency [23],[29].

The design of a slot array antenna rely on placing the slots, i.e. cut openings, in the waveguide wall at suitable positions so that certain characteristics of the array as a whole can be achieved [28],[9]. Suitable placement of the slots rely on knowing the field distribution inside the waveguide. The distribution tend to quickly become complicated when the number of modes increase. The design procedure is therefore greatly simplified if only a single mode, i.e. TE_{10}, propagates inside the waveguide [28]. It is therefore important to dedicate some additional attention to this mode.

The fields corresponding to $m= 1, n= 0$ can be derived from the equations in (2.28) and (2.29) [22]. The fields are expressed in the equation (2.32)

$$H_z = A_{10}\ cos(\frac{\pi x}{a})\ e^{j(\omega t - \beta_{10} z)}\ , \tag{2.32a}$$

$$H_x = \frac{j\beta_{10} a}{\pi}\ A_{10}\ sin(\frac{\pi x}{a})\ e^{j(\omega t - \beta_{10} z)}\ , \tag{2.32b}$$

$$E_y = \frac{-j\omega\mu a}{\pi}\ A_{10}\ sin(\frac{\pi x}{a})\ e^{j(\omega t - \beta_{10} z)}\ . \tag{2.32c}$$

The field corresponding to E_y is shown in Figure 2.16, while H_z and H_x are shown in Figure 2.17. It can be noted in Figure 2.16(a) how E_y must be zero at the walls in order to satisfy the boundary conditions in (2.14). The surface current flowing along the inner walls of the waveguide can be calculated (see Section 2.4.3.2) by equation (2.14b). The surface current in the xz-direction of the waveguide is shown in Figure 2.18.
It is apparent that the field components depicted in Figure 2.17 and 2.18 varies periodically in the propagation direction. The periodic variation can be described by the *guided wavelength* $\lambda_{g_{mn}}$. The guided wavelength can be derived from β_{mn} and is defined in equation (2.33) [22]

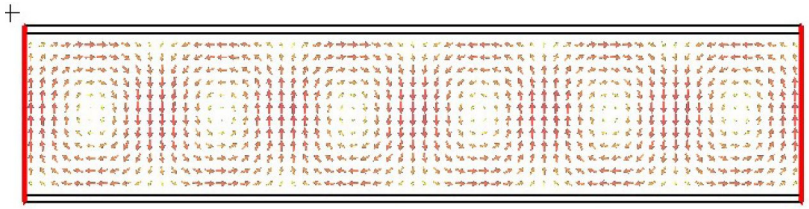

Figure 2.17: The TE_{10} mode of a rectangular waveguide. The H_z and H_x components of the TE_{10} mode in the xz-direction [29].

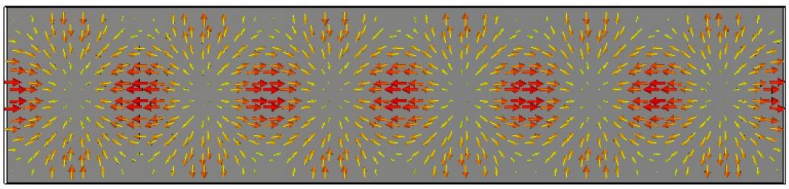

Figure 2.18: The surface current of the TE_{10} mode in the xz-direction [29].

$$\lambda_{g_{mn}} = \frac{2\pi}{\beta_{mn}} = \frac{2\pi}{\sqrt{k^2 - k_c^2}} \ . \tag{2.33}$$

The wavelength of a guided wave carries the same physical meaning as the wavelength of an unguided wave in free-space; it is the shortest distance between two points on the propagating wave with equal phase [23],[9]. A consequence of equation (2.33) is that the guided wavelength for a given frequency always is *larger* then the corresponding free-space wavelength [22],[9]. The guided wavelength is an important parameter when designing a slot array antenna.

Finally, the impedance of the waveguide is defined by the transverse components of the propagating wave [22]. The impedance ,$Z_{TE_{mn}}$, of a propagating TE wave is given by equation (2.34)

$$Z_{TE_{mn}} \equiv \frac{E_x}{H_y} = \frac{-E_y}{H_x} = \frac{k\eta}{\beta_{mn}} \ . \tag{2.34}$$

2.4.3 A Single Slot in the Wall of a Rectangular Waveguide

A rectangular waveguide slot antenna consist of one or several openings in the waveguide walls from which the field inside the waveguide couples to the space outside the waveguide. The waveguide itself is hence used as a feeding system to the antennas, i.e. the slots [9]. Antennas where fields radiate from an opening in a metal wall is known as *aperture antennas* [9],[23].

2.4.3.1 Babinet's Principle and the Half-Wave Dipole

An aperture antenna can be analyzed using Babinet's principle [29],[30]. The principle is illustrated in Figure 2.19.
Consider Figure 2.19(a). The figure shows a screen and the complement of the same screen. Babinet's principle was originally formulated from studies of diffraction patterns

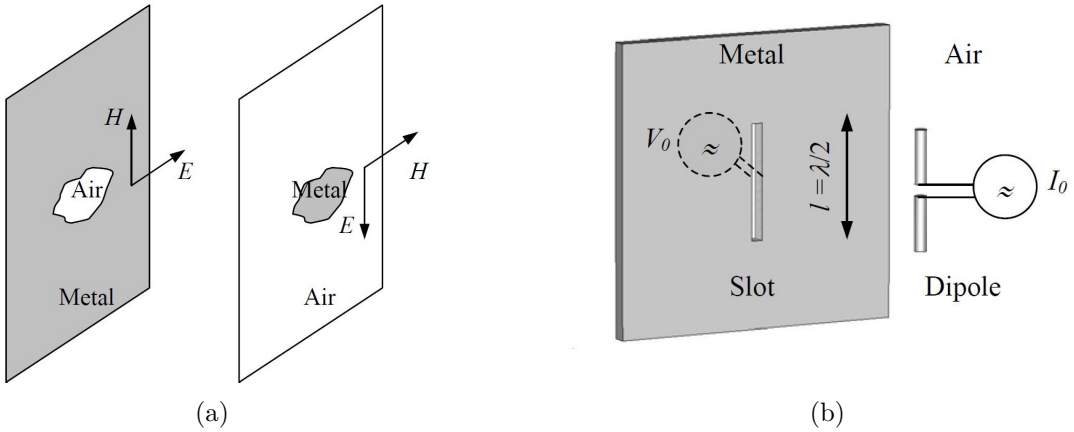

Figure 2.19: Illustration of Babinet's principle for aperture antennas [23]. (a) A metallic screen with an arbitrary cut opening and its complement, i.e. a metal piece with the same geometry as the whole with air around, will both yield the same radiation pattern but the $\vec{E}$ and $\vec{H}$-fields are interchanged. (b) A slot of length $\frac{\lambda}{2}$ excited by a voltage source and the complementary half-wave dipole of the slot.

of light. It states that a screen and the complement of the same screen will both yield the same diffraction pattern when illuminated by a light source [30],[9]. The analogues of Babinet's principle for a slot antenna are as follows: the radiation pattern of the slot is analogous to the diffraction pattern, and the EM field source is analogous to the light source. It can however be seen in Figure 2.19(a) that the EM fields of the screen and its complement are interchanged in order for Babinet's principle to hold true [23],[30]. This is a general results that is valid for all aperture antennas [23],[29].

Consider now Figure 2.19(b). It shows that a slot connected to a voltage source and the complement of the slot, i.e. a metal rod or a dipole, connected to a complementary source, both will yield the same radiation pattern. A slot of arbitrary length, l, may therefore be analyzed as a dipole of the same length. This dipole is known as the *complementary dipole* of the slot. The length is commonly chosen to be $\frac{\lambda}{2}$ so that the slot can be analyzed as a *half-wave dipole*. The reason for this choice is that a dipole will radiate at this length and multiples thereof [27]. In order to understand the continued analysis of the slot better should some key concepts of the half-wave dipole first be presented.

The schematic of the dipole is shown in Figure 2.19(b) and Figure 2.4. A dipole is essentially a source connected to a *balanced* transmission line, i.e consisting of two conductors. The source can either be a voltage or current source and will yield voltage- and current waves traveling along the transmission line. The ends of the balanced transmission line are bent at a right angle and each length is $\frac{\lambda}{4}$ long [27]. The bended conductors constitute the radiating structure of the dipole.

In order to understand the radiation pattern of the dipole must the voltage and current waves traveling along the conductors be understood. Figure 2.20 shows the reflection of the voltage- and current waves along an unbalanced transmission line for an open-circuited termination.
It is seen that the open-circuit will reflect the voltage and current so that a *standing wave* is created. It can be deduced from Figure 2.20 that a current null will appear at the open end of the conductors. A well known results is that the null (max) of a standing wave will be transformed to a max (null) by a transmission line that is $\frac{\lambda}{4}$ long [22],[27]. The $\frac{\lambda}{4}$ conductors will therefore provide a current max at the point where the conductors are

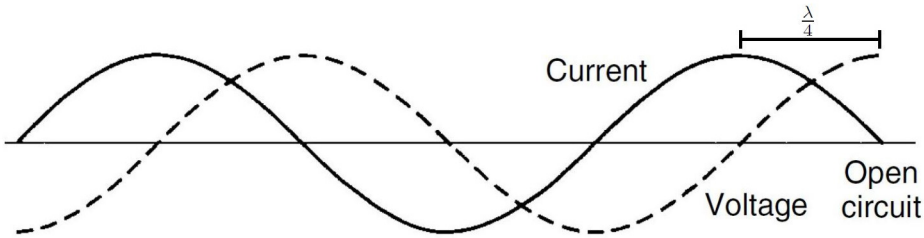

Figure 2.20: Reflection of voltage- and current waves along an unbalanced transmission line terminated with an open circuit [27]. A distance of $\frac{\lambda}{4}$ from the open end is indicated. Note that the indication of this distance has been added to the original Figure.

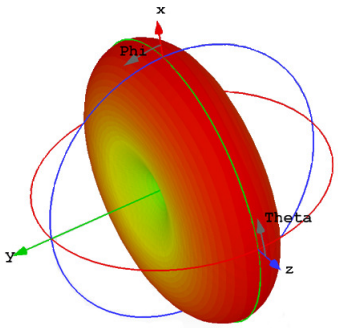

Figure 2.21: The radiation pattern of a y-directed half-wave dipole in CST.

bent. This yields in effect a standing current pattern that approximately appear as a semi-circle (the solid red line in Figure 2.4) [27]. When the polarity of the driving source is reversed will the direction of the currents in the conductors also be reversed and the semi-circular current pattern (the dashed red line in Figure 2.4) will be set up in the opposite direction [27]. Since the current waves in the conductors give rise to radiated magnetic $\vec{H}$-field by equation (2.1b), will the radiation be proportional to the shape of the current waves in the conductors. The full radiation pattern of the dipole will therefore be shaped as a donought (see Figure 2.21) [27].

It was stated in Section 2.2.1.1 that the polarization of a dipole is given by the direction of the dipole. This can be understood as the $\vec{H}$-field will be orthogonal to the current waves (equation [2.1b]) while the associated $\vec{E}$-field will be orthogonal to $\vec{H}$ and hence parallel to the current waves and the dipole itself [27]. This implies that the polarization of a slot also will yield linear polarization due to Babinet's principle as long as the slot is excited with a single current component (see Section 2.4.3.2). It has been shown that the fields of the slot and its complementary dipole are interchanged, which will also mean that the polarization will be interchanged [9], [28]. This means that if the complementary dipole is horizontally polarized will the slot yield vertical polarization and vice versa if the complementary slot is vertically polarized [30].

One final note regarding the polarization of the dipole is important to make. In theoretical presentations of the dipole it is commonly assumed that the dipole is infinitely thin [12][27]. This implies that the current flowing inside the dipole truly will flow in the direction of the dipole. In practice is the thickness finite, such that the current not only flow in the direction of the dipole, but also in the transverse direction along the radius of the dipole. The current flow will therefore not be completely uniform, which

degrades the purity of the polarization somewhat. By virtue of Babinet's principle must the polarization of the slot also be effected by its width. The reason for this is that the slot will start to interrupt both components of the TE_{10} surface current as the width is increased [23],[30]. It has been shown in previous work that a slot width of $\frac{1}{10}$ of the slot length is sufficient for the slot to yield good polarization purity [23],[30].

One important concept is the so called *radiation impedance* (Z_{rad}=R_{rad}+jX_{rad}) or *radiation admittance* Y_{rad}=G_{rad}+jB_{rad} of an antenna. R_{rad} (G_{rad}) represents the real-valued power from the source that are either radiated or dissipated as heat in the antenna structure, while G_{rad} (B_{rad}) is related to power that is not radiated but oscillates in the antenna structure, i.e. reactive power [12]. The dipole is said to be at resonance when it radiates. A dipole that is $\frac{\lambda}{2}$ long radiates, so this length is referred to as the resonance length of the dipole [27],[30]. The imaginary part of the dipole impedance or admittance is zero at resonance [23],[30].

2.4.3.2 Properties of a Single Slot

The actual radiation of the slot is caused by the surface current on the waveguide walls [23],[28]. The slot will interrupt the surface current and cause it to flow around the slot. The circulating current creates a time-varying electric field across the slot, which will cause a EM wave to propagate in the space outside the waveguide [29],[23]. It is seen in Figure 2.19(b) that the slot is excited with a voltage source. This notation indicate the field across the slot that give rise to the radiation [22]. The field that arise due to the surface current circulating the slots can be understood better if we consider the law of conservation. This law states that electrons cannot be created or destroyed. A flow of electrons leaving a closed area must therefore be equivalent to a negative time-derivative of the charges enclosed by that area [21]. The law of conservation is defined in equation (2.35)

$$\nabla \cdot \vec{J} = -\frac{\partial \rho}{\partial t} = -\epsilon \frac{\partial}{\partial t}(\nabla \cdot \vec{E}) \ , \tag{2.35}$$

where $\vec{J}$ is a physical current corresponding to the surface current inside the waveguide. The last equivalence in equation (2.35) is obtained by using equation (2.1c) to substitute ρ and then use the constitutive relation in (2.2a) [21],[23]. When a slot is introduced is the current forced to flow from the inner wall to circulate the rim of the slot [23]. This yield a situation where the current is leaving the waveguide. The total charge must then be conserved, which give rise to a changing electric field in the area where the current was changed, i.e. across the slot [23]. The time-derivative of an electric field can be recognize from (2.1b) as a displacement current, which is equivalent to a rotating magnetic field. An EM wave, proportional to the field inside the waveguide, will thereby start to radiate from the slot. An important consequence of equation (2.35) is that the change or interruption of the current caused by the slot is proportional to the field that will be radiated by the slot [23],[9],[28]. By knowing the distribution of the surface current can the magnitude of the radiation from the slot be controlled [9],[28].

As mentioned previously is the waveguide designed so that only the TE_{10} mode will propagate. The corresponding surface current on the top wall and sidewalls of the guide (see Figure 2.15) can be obtained from the boundary conduction in (2.14b). The surface

currents are expressed in equation (2.36) [22],[31].

$$\vec{J}_{top\ wall} = -\hat{y} \times (H_z\hat{z} + H_x\hat{x})|_{y=b} = \vec{J}_x + \vec{J}_z \ , \tag{2.36a}$$

$$\vec{J}_{right\ side} = -\hat{x} \times (H_z\hat{z} + H_x\hat{x})|_{x=a} = \vec{J}_y \ , \tag{2.36b}$$

$$\vec{J}_{left\ side} = \ \ \hat{x} \times (H_z\hat{z} + H_x\hat{x})|_{x=0} = \vec{J}_y \ , \tag{2.36c}$$

where the field components are given in equation (2.32). An inwards pointing surface normal, $\hat{n}$, at the respective wall is used to derive the expressions in equation (2.36). The vector components of the surface currents in equation (2.36) are given in equation (2.37)

$$\vec{J}_x = -\hat{x}H_z = -\hat{x}\frac{jA_{10}}{\omega\mu}\ cos(\frac{\pi x}{a})\ e^{-j\beta_{10}z} \ , \tag{2.37a}$$

$$\vec{J}_y = \ \ \hat{y}H_z = -\hat{y}\frac{jA_{10}\pi}{\omega\mu a}e^{-j\beta_{10}z} \ , \tag{2.37b}$$

$$\vec{J}_z = \ \ \hat{z}H_x = \ \ \hat{z}\frac{A_{10}}{\omega\mu}\ sin(\frac{\pi x}{a})\ e^{-j\beta_{10}z} \ . \tag{2.37c}$$

The current on the bottom wall of the waveguide is not considered, since normally the slot is not placed there. Let's now analyze the surface current on the broad wall of the waveguide.

Equation (2.36a), (2.37a) and (2.37c) implies that the current is composed of two orthogonal components. These components may be used to realize orthogonal polarization's depending on how the slot is placed [31],[9]. Three categories of slots can be defined based on how they are positioned. The slot types are illustrated in Figure 2.22(a).

Slot (1) in Figure 2.22(a) represents a *longitudinal* slot, i.e. the slot is directed along the waveguide. The vector lines corresponding to equation (2.36b) are superimposed on the figure. It can readily be seen that the longitudinal slot only interrupts the $\vec{J}_x$ component. The slot is therefore excited by this component only and will be linearly polarized. The question is whether the polarization is horizontal or vertical. The slot is horizontally directed with respect to the ground. The complementary dipole of the slot would hence be horizontally polarized. The longitudinal will therefore be vertically polarized in accordance with Babinet's principle [23],[30].

Since a slot act as an antenna is the slot characterized with an antenna impedance (see Section 2.4.3.1). It is also reasonable to characterize the slot with an impedance because the slot interrupts the surface current in the waveguide and thus act as an impedance [23],[29]. It can be shown that the longitudinal slot can be modeled as an shunt admittance Y_s [31],[28],[9]. This admittance, normalized with the admittance of the waveguide, is given by equation (2.38) [9],[31]

$$y = \frac{Y_s}{Y_{TE_{10}}} = \frac{-2s_{11}}{1 + s_{11}} \ , \tag{2.38}$$

where Y_s (y) denote the unnormalized (normalized) slot admittance and s_{11} is the normalized *reflection coefficient* associated with y. The reflection coefficient represents the scattering of the incident TE_{10} mode caused by the slot [32],[31]. The variable $Y_{TE_{10}} = \frac{1}{Z_{TE_{10}}}$

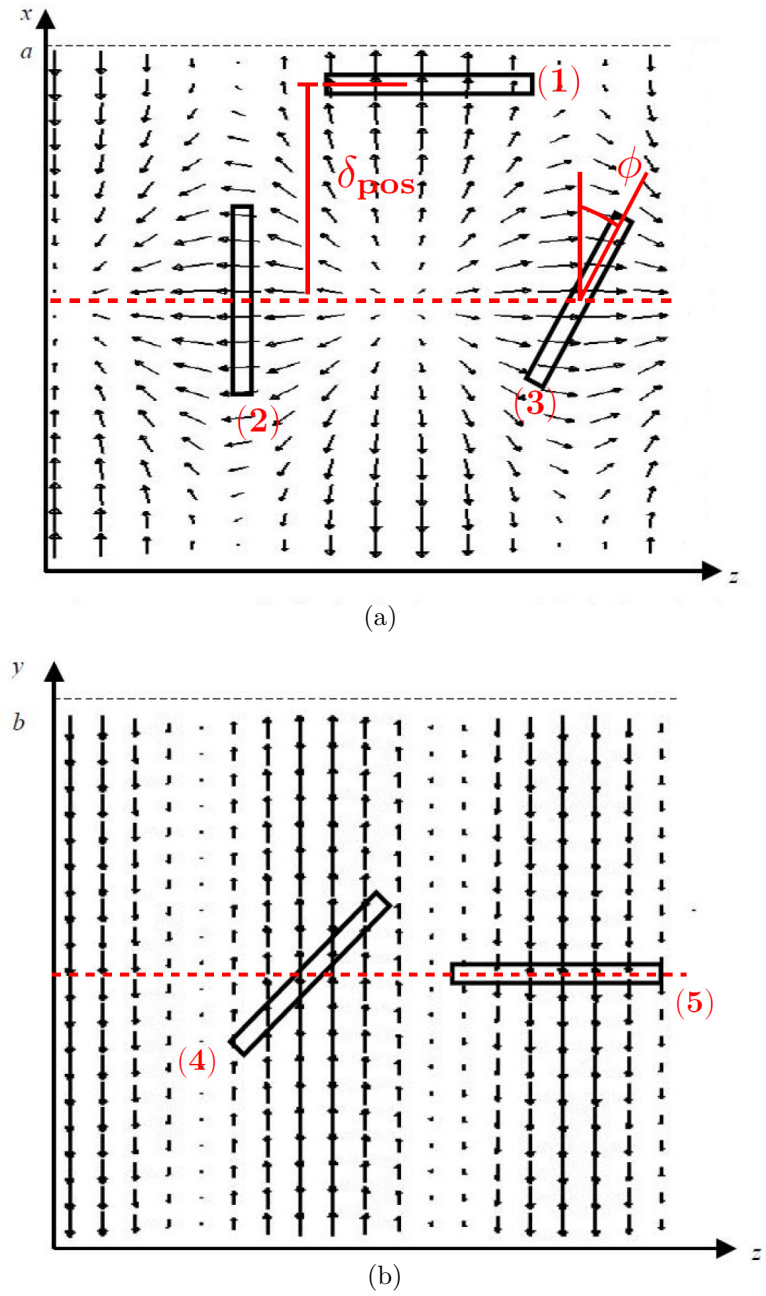

Figure 2.22: Illustration of different slot types [23].The surface currents corresponding to the TE_{10} mode is superimposed on the figures. (a) Three types of slots placed on the broad wall of the waveguide. The type of slots are the longitudinal, transverse and the compound slot that are numbered (1)-(3). Slot (1) and (2) are placed with an offset, δ_{pos}, from the center line, i.e. $x = \frac{a}{2}$, of the broad wall that is indicated by the red dashed line. The offset position is measured between the center line and the middle of the slot, which is indicated by the red solid line on slot (1). Slot (3) is placed at the center line but is rotated with the angle ϕ. (b) A compound slot and a longitudinal slot placed on the center line of the narrow wall of the narrow wall, i.e. $y = \frac{b}{2}$, of the waveguide. The slots are numbered (4)-(5). Note that the indication of the center lines as well as the offset position from the center line, the middle line of slot (1), rotation angle of slot (3) and the individual numbering of the slots has been added to the original Figures.

in equation (2.38) is the admittance of the waveguide when the TE_{10} mode propagate in the waveguide. Note that $Z_{TE_{mn}}$ was defined in equation (2.34).

Slot (2) represent the second category of slots and is called a *transverse* slot, i.e.

the slot is directed transverse to the direction of the guide. This slot interrupts the $\vec{J}_z$ component. It can be seen from equation (2.37) that $\vec{J}_z$ and $\vec{J}_x$ is 90° out of phase. For this reason will the slot yield horizontal polarized radiation [32]. The transverse slot is modelled as a series impedance. The series impedance, Z_s, normalized to the impedance of the waveguide, is given by equation (2.39) [28]

$$\frac{Z_s}{Z_{TE_{10}}} = \frac{2s_{11}}{1 - s_{11}} \ . \tag{2.39}$$

Equation (2.38) and (2.39) are important when designing an array consisting of multiple slots as will be explained in Section 2.4.4.

Slot (3) represent the last category of slots and is called a *compound slot* [31],[28]. A compound slot will interrupt both components in (2.36a) and yield no linear polarization [28]. The equivalent circuit for this slot is a series impedance [28].

Figure 2.22(a) reveals that $\vec{J}_x$ is oppositely directed on either side of the center line. A longitudinal slot placed at the center would hence not be excited by $\vec{J}_x$ as it would cancel at this position [9],[28]. It can also be seen that the strength of $\vec{J}_x$ increases symmetrically from the center position. The excitation of the slot can therefore be increased by increasing the offset, δ_{pos}, from the center position [9],[32]. Note that δ_{pos} refers to the distance between the center line and the middle of the slot (see Figure 2.22(a)). Similarly, it can be concluded from the figure that the transverse slot will be maximally excited by $\vec{J}_z$ at the center position and weaker excited as δ_{pos} is increased. Furthermore, if the transverse slot is rotated and thus becomes a compound slot, will the excitation decrease as the rotation angle ϕ is increased [9],[28],[31].

Figure 2.22(b) shows two slots placed on the center line of the narrow waveguide wall, i.e. $y = \frac{b}{2}$). Note that the slots should be placed on the center line and that $\delta_{pos}= 0$ for these slots. The $\vec{J}_y$ component is superimposed on the figure. It can be seen that the amplitude of $\vec{J}_y$ is constant but that the direction of $\vec{J}_y$ alternates. The alternation occurs when the phase of $\vec{J}_y$ is advanced with $\frac{\lambda_{g10}}{2}$ [29],[23]. Slot (4) is a compound slot and is rotated in the same manner as slot (3). Slot (4) will not yield linearly polarized radiation. The reason is that $\vec{J}_y$ can be decomposed into one vertical and one horizontal vector component, which both are interrupted by the slot [28]. Slot (5) is a longitudinal slot. The slot can be seen to interrupt $\vec{J}_y$ fully and will therefore be more strongly excited than slot (4). The polarization of a longitudinal slot on the narrow wall is however horizontal [28]. The observations made for slot (4) and (5) suggest that the the excitation can be controlled by rotating the slot; slot (5) is maximally excited and by rotating slot (5) 90°, i.e. $\phi= 0°$, can the excitation be decreased towards zero. Slot (4) and (5) are modelled as a shunt impedances [28],[31].

2.4.4 Design of a Slot Array Antenna

A configuration of multiple antennas of the same type, i.e antenna elements, that are excited by the same source is known as an *array antenna* [12]. The antenna elements in the array can be arranged in a *linear* or *planar* configuration, i.e distributed along a line or a over surface [12]. The array antenna can generally achieve higher directivity than the individual antennas constituting the array. Another advantage of array antennas is that the main beam both can be *steered* and *shaped* by controlling the *excitation*, i.e amplitude and phase, of each element in the array [12]. Since the main beam is steerable it is meaningful to introduce the terms *broadside* and *end-fire*. A broadside (end-fire)

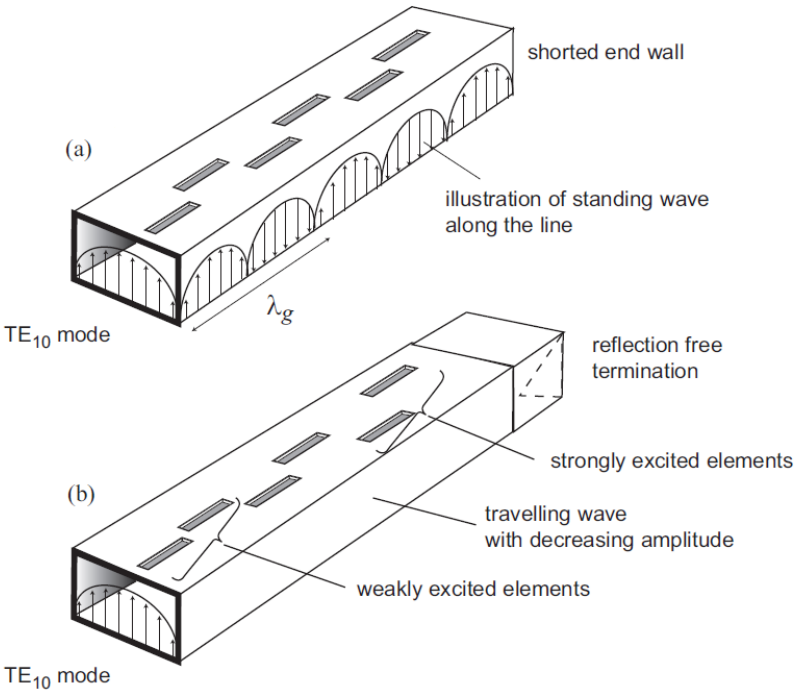

Figure 2.23: Illustration of an (a) standing wave and (b) traveling wave rectangular slot array [12].

array means that the main lobe is located orthogonal (parallel) to the direction of the antenna elements [12]. No further information about array antennas in general will be given other than the following rule, given by equation (2.40), that should be met when designing a slot array of *standing wave* type [12]

$$d < \lambda \ , \tag{2.40}$$

where d is the spacing between the antenna elements. The meaning of a standing wave slot array will be explained shortly. Equation (2.40) states that if the spacing between the elements of the array is larger then the free space wavelength of the exciting source will so called *grating lobes* start to appear in the region of the main-beam. Grating lobes are side-lobes that start to approach the main beam when (2.40) is not fulfilled. Grating lobes can only be observed for array antennas [12].

Introducing multiple slots in a single rectangular waveguide means that the slots will be excited by the fields propagating inside the guide. This configuration may hence be categorized as a *linear* array antenna [9],[28]. For a simplified design should the source field inside the guide only propagate as TE_{10} mode only [9].

Two different types of rectangular slot antennas exist. These are the *standing wave array* (SWA) and the *travelling wave array* (TWA) antenna [28]. The main principle of the SWA and the TWA can be understood from Figure 2.23.
It is apparent from Figure 2.23 that both the SWA and the TWA are excited with a source field propagating as the TE_{10} mode. The propagating mode is however transformed to a standing wave in the SWA. The standing wave is created by introducing a short-circuit, i.e a metallic wall, at the end of the waveguide [32]. Figure 2.23(a) show that the slots are located above the antinodes of the standing wave, which means that each slot becomes

uniformly excited by the TE_{10} mode. In order to place the slots above the anti nodes must the spacing between each slot be the same [32],[9]. This statement will be elaborated shortly.

A matched load is used at the end of the TWA. The matched termination ensures that the mode will not be reflected and thereby transformed to a standing wave [33]. The offset position of the slots is increased progressively between the first and last slot. The reason for this is to ensure that the slots will radiate as much of the incident mode as possible, which otherwise wastefully will be absorbed in the matched load. The slot closest to the feed must be weakly excited in order to not radiate all of the incident mode. The last slot must be strongly excited since the mode has travelled the furthest distance to this slot and will hence be the most attenuated when reaching the slot.

Another main difference between the SWA and the TWA is that the length of the slots should be equal to the resonance length ($\frac{\lambda}{\mathbf{2}}$) in the SWA, while this is not required for the TWA. Note that λ corresponds to the wavelength of the desired center frequency of the array which naturally must be supported by the TE_{10} mode of the waveguide [9],[28]. Another difference between a SWA and a TWA is that the SWA yield a broadside antenna that is not steerable. The TWA on the other hand may yield a steerable main-beam by continuously varying the frequency of the TE_{10} source [33]. Even if the source is not varied will the TWA yield a main-beam not pointing in the broad-side direction [33] The remaining part of this Section will be dedicated to the SWA antenna.

The SWA can be designed for vertical or horizontal polarization by placing the slots in different configurations [9],[32]. The configuration shown in Figure 2.23(a) consist of longitudinal slots on the broad wall of the waveguide. The slots will each yield vertically polarized radiation in accordance with the theory presented in Section 2.4.3.2.

Consider again the standing wave pattern in Figure 2.23(a). The slot that is closest to the metallic wall is placed above the first anti node. As stated in Section 2.4.3.1 is a current null transformed to a max at a distance corresponding to a quarter wavelength of the transmission line. The center of the first slot is therefore placed $\frac{\boldsymbol{\lambda_{g10}}}{\mathbf{4}}$ from the wall.The distance to the next max is $\frac{\lambda_{g10}}{2}$. This distance that is measured from the center of the first slot to the center of the next slot is therefore used. In fact, a spacing of $d = \frac{\lambda_g}{2}$ must be used between all the other slots in the array to ensure that the slots are placed above each antinode. The slot shown in Figure 2.23(a) consist of six slots but the general principle for placing the slots applies for a SWA consisting of any number of slots [28],[32]. The SWA in Figure 2.23(a) is called a *end-fed* SWA as the mode is fed from one end of the waveguide. The standing wave condition can also be achieved by placing short circuiting walls at both ends of the waveguide and instead feed the TE_{10} mode from the middle of the guide. This is known as a *center-fed* SWA [28],[9]. The outer slots must then both be placed $\frac{\boldsymbol{\lambda_{g10}}}{\mathbf{4}}$ from the walls while the intermediate slot distance is $d = \frac{\boldsymbol{\lambda_{g10}}}{\mathbf{2}}$ [28],[9],[34]. An end-fed and a center-fed SWA with longitudinal slots are shown in Figure 2.24. A larger antenna bandwidth can generally be achieved by feeding the array from the center rather than from one end of the waveguide [28]. The meaning of this bandwidth will be explained further down in this section

Consider the configuration of the slots in Figure 2.24. It can be seen that the slots are placed offset from the center line in an alternate manner, i.e. the slots are placed alternately with the offset $\boldsymbol{\delta_{pos}}$ and $-\boldsymbol{\delta_{pos}}$. The reason for this is to ensure that the slots are uniformly excited. The standing wave condition ensures that the slots will be excited with a uniform amplitude of TE_{10} mode. In order for the amplitude to remain uniform must the phase of the TE_{10} mode change by 360° between each slot [33],[32],[34]. A

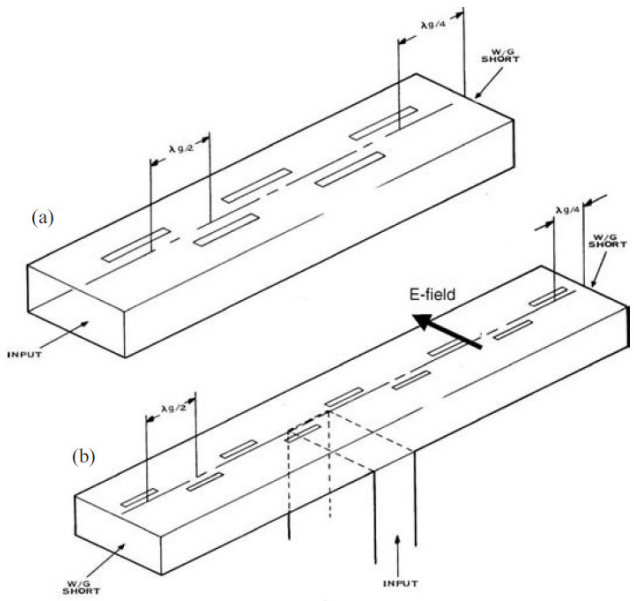

Figure 2.24: Illustration of an end-fed (a) and a center-fed (b) vertically polarized SWA [28]. The direction of the radiated field corresponding to vertical polarized radiation is indicated by the bold arrow.

distance of $\frac{\lambda_{g10}}{2}$ is equivalent to a 180° phase advance of the TE_{10} mode. It can however be seen in Figure 2.22 that $\vec{J}_x$ is oppositely directed along the center line. The phase difference between slots on opposite side of the center line is therefore 180°, which yields that two alternately placed slots spaced $\frac{\lambda_{g10}}{2}$ apart will be excited in phase [32],[34].

A SWA that yields horizontal polarization can be realized by using the same principles when placing the slots, but instead utilize a compound slot placed on the broad wall or on the narrow wall of the guide [35]. A pair of slots on the narrow wall of the waveguide are shown in Figure 2.25.

It is suggested in Figure 2.25 that the slots corresponding to a horizontally polarized SWA are rotated in an alternating fashion, i.e. If the first slot is rotated by the angle $\boldsymbol{\phi}$ should the next slot be rotated by $-\boldsymbol{\phi}$ and so on (see Figure 2.22(b)). The alternating rotation causes the vertical components of $\vec{J}_y$ to cancel and thereby ensure that the polarization will be be horizontal [35],[28]. The full length of the slot will usually not fit on the narrow wall. The slot must therefore "wrap" around or cut into the adjacent broad walls of the waveguide to reach the resonant length [35],[28]. This is shown to be the case in Figure 2.25. For simplicity should the same distance be cut into the top- and bottom walls of the waveguide [35].

It was mentioned in Section 2.4.3.2 that both slots (1) and (4) in Figure 2.24 can be modeled as shunt admittances. An end-fed SWA consisting of N slots of either type shown in Figure 2.25 can therefore be modeled using the equivalent circuit shown in Figure 2.26 [23].
Note that y in Figure 2.26 is the normalize admittance given by equation (2.37). It was stated in 2.4.3.1 that the admittance/impedance of the antenna is proportional to the source that excite the antenna. Since the slot excitation is uniform for an SWA will the admittance of each slot be the same [23],[9]. The normalized admittance of the slots may therefore simply be put in parallel, which means that the they can be summed [23]. The variable y_{in} in Figure 2.26 represent the normalized input impedance of the SWA and can be expressed according to equation (2.41) [23]

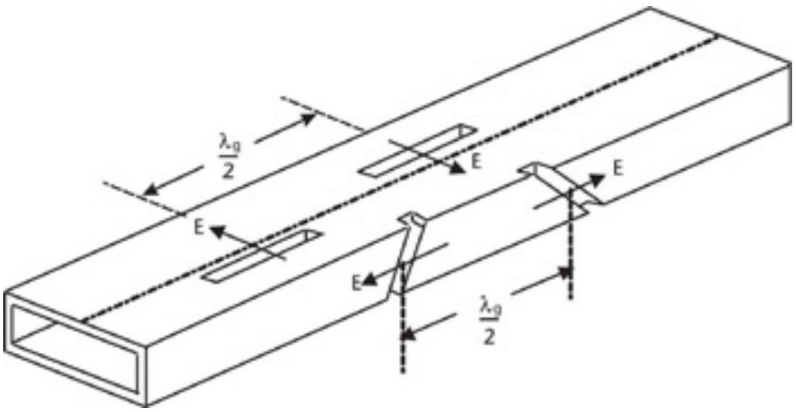

Figure 2.25: Illustration of a pair of longitudinal slots and compound slots on the broad and on the narrow wall of a rectangular waveguide [28].The different types of slots are used to realize a vertically or horizontally polarized SWA. The polarization of each slot is indicated by the arrows superimposed on the slots. The polarization of the compound slots is along the ground, i.e horizontal, while the polarization of the other slots is orthogonal, i.e. vertical.

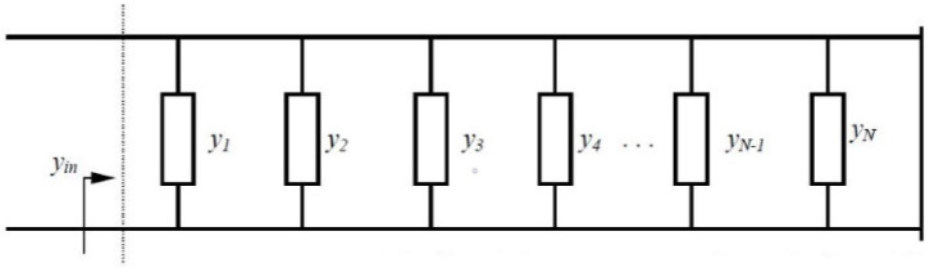

Figure 2.26: Equivalent circuit of an SWA consisting of N slots [23]

$$y_{in} = \sum_{n=1}^{N} y_n, \tag{2.41}$$

Equation (2.41) can be used to formulated the so called *design equation* of the SWA [28],[9],[34]. The design equation is formulated in equation (2.42)

$$y_{in} = \sum_{n=1}^{N} g_n = 1 \ , \tag{2.42}$$

where it can be seen that y_n in equation (2.41) has been replaced by its real part g_n. The reason for this is that the slots in the SWA are at resonance [23]. Equation (2.42) represents a perfect match of y_{in} at the input port. The SWA will then receive all source power at the input without reflections [22]. This will in turn yield infinitely low return loss at the frequency where equation (2.42) is fulfilled [22].In practice can a perfect match not be achieved and equation (2.42) can only be fulfilled reasonably well for a band of frequencies around the resonance frequency of the slots [23],[30]. The S_{11} bandwidth of the the SWA is commonly given at the $-10\,\mathrm{dB}$ level, i.e. the frequency band for which $S_{11} < -10\,\mathrm{dB}$ [30]. This bandwidth will be refereed to with the variable Δf_{-10dB}. It is important to note it is not possible to actually verify that equation (2.42) is fulfilled by

other means than measuring S_{11} at the input port of the SWA and see that it is sufficiently low at the resonance frequency [31],[28]. For a center-fed SWA should equation (2.42) instead be equal to two.

The normalized admittance in equation (2.38) depends on the orientation of the slot, i.e displacement from the center line or rotation. The matched condition may then be achieved by finding the offset, δ_{pos} or rotation, ϕ, that will fulfill equation (2.42) for a given number of slots. This means that if the array consist of N slots should an offset or rotation angle be used such that $g_n = \frac{\mathbf{1}}{\mathbf{N}}$. Since the admittance of each slot is equal in an SWA, it is enough to find the offset or rotation of a single slot that corresponds to $g_n = \frac{\mathbf{1}}{\mathbf{N}}$ and use the principles outlined previously in this Section to place the slots [23],[29],[9].

Analytic formulas for calculating the slot conductance for different offset positions or rotation angles exist [23],[29]. These equations are however not very accurate as they do not account for various factors that influence the admittance in equation (2.38). This includes for example the thickness of the waveguide wall and coupling between the slots [23],[9]. The resonance value of the admittance for a given rotation angle or offset position of the slot must hence be found empirically, i.e by utilizing some EM simulation program followed by practical measurements. [9],[31]. In the SWA is the same offset or rotation used for all slot to ensure that the excitation of the slots are the same. It is also possible to use different values of δ_{pos} and ϕ of the slots and still fulfill the design equation. By varying the excitation it is possible to design the SWA so that a certain sidelobe level is achieved [34]. The excitation of the slots is then typically varied according to some mathematical distribution [34],[35].

A final note regarding the SWA should be made. The longitudinal slots depicted in Figure 2.23, 2.24 and 2.25 are all rectangular sharpened. Normally will the ends of the slots be rounded due to the fabrication process, i.e. milling [28],[9]. Sometimes are the ends of the slot also enlarged. Such a slot is due to its shape known as a *dumbbell slot*. This slot will yield a shorter resonance length than the corresponding rectangular slot for a given offset or rotation. A SWA consisting of dumbbell slots has also show to be more broadband but is also associated with a higher Cross-polar component [28],[23]

3
Methods

This chapter is divided in two main parts. The first part describe the preliminary study that was performed with WSAP and Matlab to investigate the array configuration required to achieve a certain field variation in the test zone. Based on the study in WSAP, was one of the investigated arrays implemented as an rectangular waveguide SWA antenna. The array was design in CST and the design procedure is described in the second part of this chapter.

3.1 Near-Field Simulations Using WSAP

In WASP was the near-field from the array reconstructed by sweeping a z-orientated half-wave dipole in a grid in the xy-plane (see Figure 3.1). The xy-plane where $z = 0$ was used in the simulations in WSAP. The length of the dipole was chosen such that the resonance frequency of the dipole occurred at 28 GHz. The distance between the grid points was set to 5 mm. For a simplified analysis was the field in front of the array not reconstructed by measuring the radiation from the array with the dipole. Instead was the dipole used as a source and the radiation from the dipole in each grid position was sampled at fixed points. The points where the radiation from the dipole was sampled will here on be referred to as the sample points. The position of the sample points were chosen to coincided with the positions of the antenna elements, such that the field from the array could be reconstructed as if the dipole was measuring the radiation from the array. This follows from the reciprocity principle.

For simplicity it was assumed that the array was positioned along the y-axis and that the spacing between the antenna elements were uniform. For an array with even number of antenna element was is assumed that one of the elements coincided with the origo and that $\frac{N}{2} - 1$ elements were placed at the $y < 0$ side and $\frac{N}{2}$ elements at $y > 0$. For an array with odd number of elements was it assumed that the middle element coincided with the origo. The sample-points in WSAP were placed according to these assumptions (see Figure 3.1). It should be noted that practical measurements of near-field always are performed by using a dipole (or some other suitable antenna) to reconstruct the near-field from the AUT and not the other way around. The two ways to reconstruct the near-field are illustrated in Figure 3.2. Note that Figure 3.2(b) essentially shows the same principle for measuring the near-field as illustrated in Figure 2.13. Figure 3.2(b) is mainly shown so that the reciprocal ways to perform near-field measurements easily can be compared in Figure 3.2. It is important to note that due to the reciprocity principle that is utilized will the words “sample point” and “antenna element” be used interchangeably throughout this chapter.

An area of 2 m $\times$ 2 m in front of the linear array was reconstructed by sweeping the dipole in the manner as illustrated in Figure 3.2(a). The sweep was performed automati-

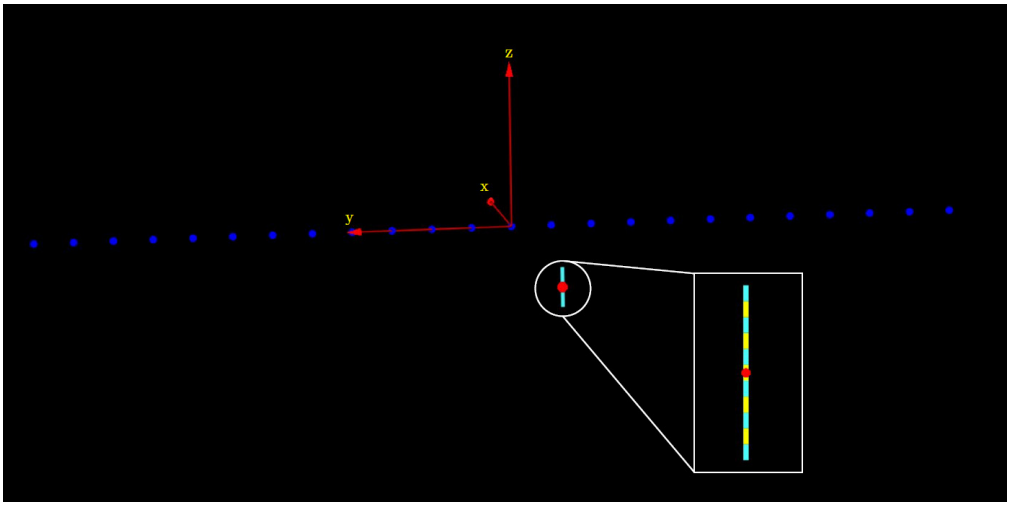

Figure 3.1: Near-field simulation in WSAP using a half-wave dipole excited by a voltage source (indicated by the red dot in the center of the dipole). The sample-points (blue dots) are located on the y-axis and the dipole is swept in a grid (not visible in the figure) in the xy-plane where $z = 0$. The blue and yellow sections covering the dipole represents the basis function associated with MoM.

cally in WSAP by loading a control file into the program. This file contained instructions for how the position of the dipole should be changed in x and y relative to the current position of the dipole. The initial position of the dipole was set in the *geometry* tab in WSAP before the sweep was executed. The control file was created using the Matlab file `MakeInc`, see Appendix A.1 for all Matlab files that were used in this Section.

First was the near-field from a single antenna element simulated, i.e. one sample point was used. This was done so that the FoM's, i.e. power/phase spread, obtained with a single antenna element could be compared with the FoM's obtained with an array. Two different arrays with 24 and 36 elements were considered for the comparison. The spacing between the sample points corresponding to these arrays were chosen as 10.714 mm, which is equivalent to λ at 28 GHz. Figure 3.1 show the near-field simulation of the 24 element array in WSAP.

The dipole was for simplicity excited by a voltage source that was purely real and equal to unity. The same excitation was used in all simulations. The basis functions indicated in Figure 3.1 describe the current on the dipole locally and are used to compute the radiation from the dipole. For accurate computations should a minimum of 10 basis functions cover a section of the dipole that is half a wavelength long. The number of basis function used were 11. The same number of basis functions were used for all simulations. Since the voltage source is located in the middle of the dipole were a odd number of basis functions preferred. The source would then be covered by one basis function and not by two overlapping functions which could cause computational errors.

The radius of the dipole was set to 1 μm which is less than $\frac{1}{1000}$ of the resonance length. A thin dipole was used for two reasons. If the width of the dipole was comparable to the length of a basis function, i.e. $\frac{\lambda}{22}$, could computational errors be introduced. A thin dipole also provides more pure polarization. If the polarization of the dipole was pure could the near-field accurately be reconstructed by only acquire one component, i.e. E_z, of the dipole radiation in the simulations. This simplified the analysis significant as less data had to be collected and processed.

The 24 and 36 element arrays were not considered just to compare with the single antenna element, but also to give an idea of how the performance, i.e. obtainable power-

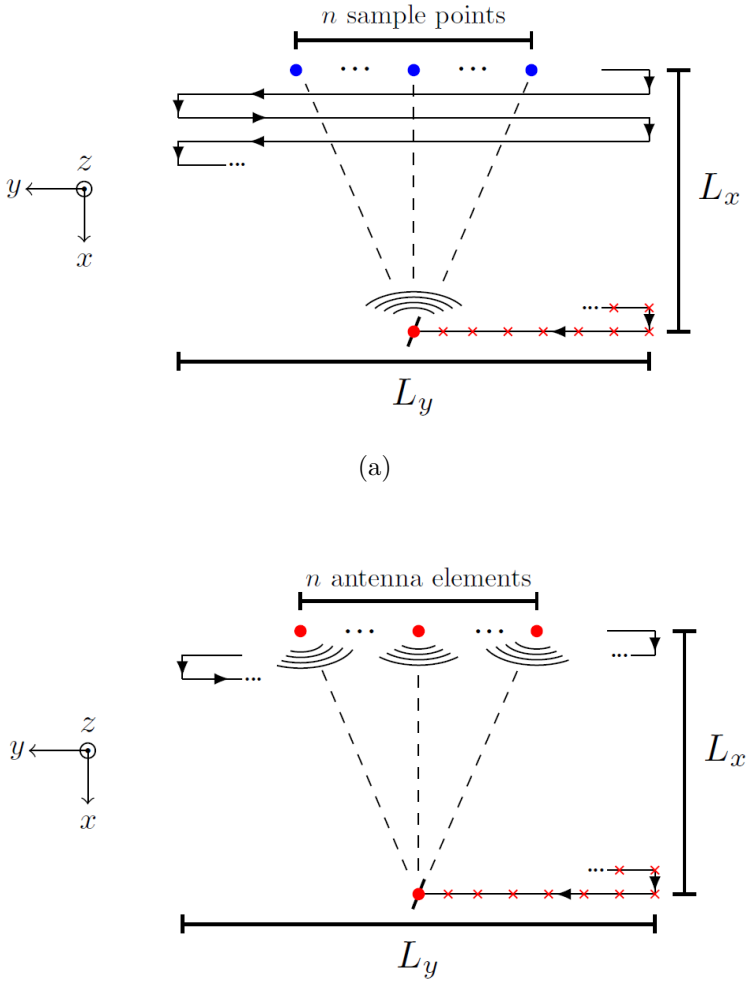

Figure 3.2: Near-field simulation in WSAP (a) and near-field measurement as it is performed practically (b). A z-orientated dipole in the xy-plane is assumed. The dipole is moved in an area in front of the sample points or antenna elements. The lines with arrows indicate how the dipole is moved withing the area. The area has an effective length of L_x and L_y, respectively in the x- and y-direction. Positions where the dipole receive or transmit are marked with a red cross. At these points is the total field given by summing the field in each sample point or from each antenna element according to the superposition principle. Note that the spacing between these points are uniform and that only some the points are marked in order to not make the figure too cluttered.

and phase spread in the test zone, changed as the number of elements were increased. To continue to investigate different array configurations more efficiently, i.e. without performing separate simulations for each configuration, was the near field from a large array of 128 elements reconstructed. The distance between the sample points was set to $\frac{\lambda}{2}$. Sample points could then be removed when processing the near-field data in Matlab so that a variety of smaller arrays could be investigated from the large array. By only including every second, third etc. sample point for the processing could also the effect of element spacing, d, be investigated. It was not possible to process the 2 m $\times$ 2m area in Matlab when 128 points were considered, as the file containing the near-field data became too large. The area was therefore reconstructed by simulating the near-field in

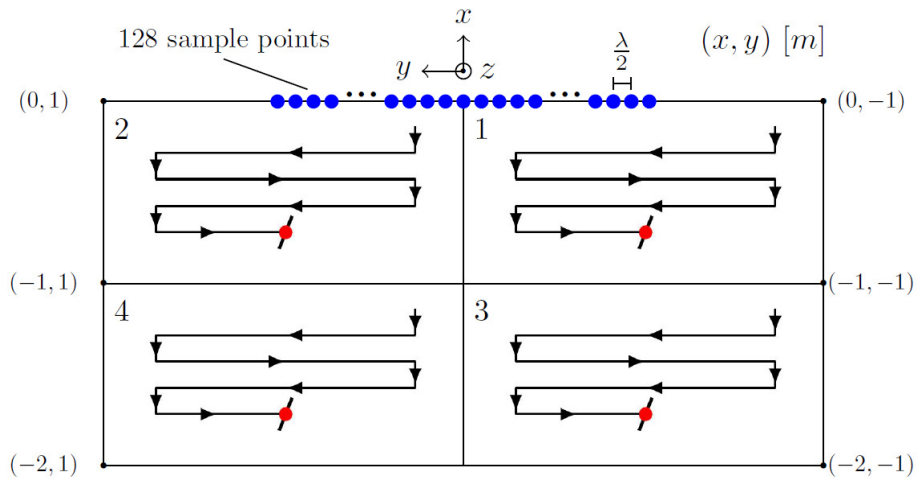

Figure 3.3: Processing of a 2 m × 2 m area in front of the array using 128 sample points. The area was reconstructed by sweeping out four smaller 1 m × 1 m areas located next to each other. The smaller areas are numbered $1 - 4$. The coordinate system and the associated coordinate points represent the coordinate system in WSAP.

four adjacent 1 m × 1 m areas (see Figure 3.3) and then process the data collected form each area separately in Matlab.

3.2 Processing of the Simulated Near-Field Data Using Matlab

The data collected from each 1 m × 1 m area was loaded into Matlab. The data was processed using the file `Read_files_WSAP.m`. This file was used to extract the different types of data that was obtained from WSAP, for example the sampled near-field. The near-field data was stored in a file with the extension *nearfield.dat*. The dipole positions were translated to positions corresponding to the coordinate system in WSAP by the dipole control file and the *.geo*-file that was loaded into the `Read_files_WSAP.m` file. The geo-file was obtained from WSAP and contained information about the initial position of the dipole, see Appendix A.2 and A.3 for information on the nearfield.dat file and the .geo file.

Figure 3.3 shows how the 2 m × 2 m area was reconstructed by concatenating the near-field data collected in each 1 m × 1 m area. The shared borders between the areas represents grid points along lines where the dipole radiation was sampled twice. These duplicated grid points had to be removed since the field otherwise would be twice as strong in these points. The concatenation and removal of duplicated grid points were performed using three different files: `Left_side.m`, `Right_side.m` and `Add_sides.m`. The first file loads the data corresponding to area 1 and 3, reshaped the near-field data to correspond to the actual 1 m × 1 m areas and removes the last sweep line in area 1, i.e. the shared border. The same thing was performed for area 2 and 4 using `Right_side.m`. Finally, was the two sides concatenated and the shared border between area 1-2 and 3-4 was removed using `Add_sides.m`.

The next step was to implement a mask or filter such that sample-points could be excluded from the continued processing in Matlab. For this purpose was `Binary_mask.m`

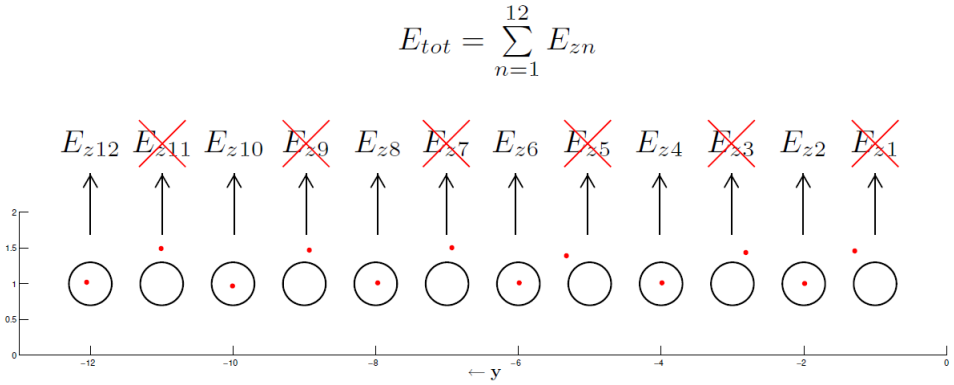

Figure 3.4: Illustration of the `Binary_mask.m` file for a smaller case of 12 antenna elements. The E_z components of the sampled dipole radiation are indicated. The sum of the points give the total field, $\vec{E}_{tot}$, at each position of the dipole. Note that The circles that are plotted by `Binary_mask.m` are shown. The red dots is the marker of the `ginput` function, i.e. where the user has clicked. The inclusion/exclusion of sample-points based on the user clicking inside or outside the corresponding circles are indicated by the excluded sample points being crossed over. Note that the binary mask only was applied for the 128 element array. The 12 element case is only shown to make the figure more clear.

used. This file allowed the user to choose the elements (represented by circles, see Figure 3.4) in the array that should be include. More information about the `Binary_mask.m` file is found in the Appendix.

In total were six smaller arrays investigated besides the 128 element array that is illustrated in Figure 3.5(a). For all of the smaller arrays (Figure 3.5(b) and Figure 3.5(c)) were sampling points on the ends of the array removed. In three of the investigated cases was also every second of the remaining sample points removed. Note that the element spacing in the three cases corresponding to Figure 3.5(c) was λ. Grating lobes may therefore appear for these arrays. All the arrays that were investigated are summarized in Table 3.1.

For each array in Table 3.1, the power- and phase spread in the circular test zone was calculated at the distance $x = D$. A test zone with a 30 cm diameter was considered. The calculations were performed using the file `Calculate_the_FoM.m`. First was the sample points from each dipole position summed so that $\vec{E}_{tot}$ at each dipole position was obtained. Note that $\vec{E}_{tot}$ was defined in (2.19) but that summation is taken over N sample points instead of over N antenna elements. Also, only the E_z-components make up $\vec{E}_{tot}$ at each dipole position as illustrated in Figure 3.4. From $\vec{E}_{tot}$ could the power, P_{samp}, at each position be calculated according to equation (2.22). The P_{samp} values corresponding to dipole positions within the test zone were then extracted by creating a matrix corresponding to the 2 m $\times$ 2 m area containing the calculated power values. From this matrix could the power values corresponding to the test zone be extracted. The mean of the extracted power values was then calculated. The extracted power values were normalized by the mean and the power spread was calculated according to equation (2.20) and (2.21) using the normalized values.

The phase spread was calculated similarly. First was the phase of each $\vec{E}_{tot}$ component calculated according to equation (2.24). After that was the vector containing the calculated phases reshaped to correspond to the 2 m $\times$ 2 m area. The diameter of the test zone located at the distance D (see Figure 3.5(a)) was thereafter extracted. The mean of the extracted phases was calculated and the extracted values were normalized by

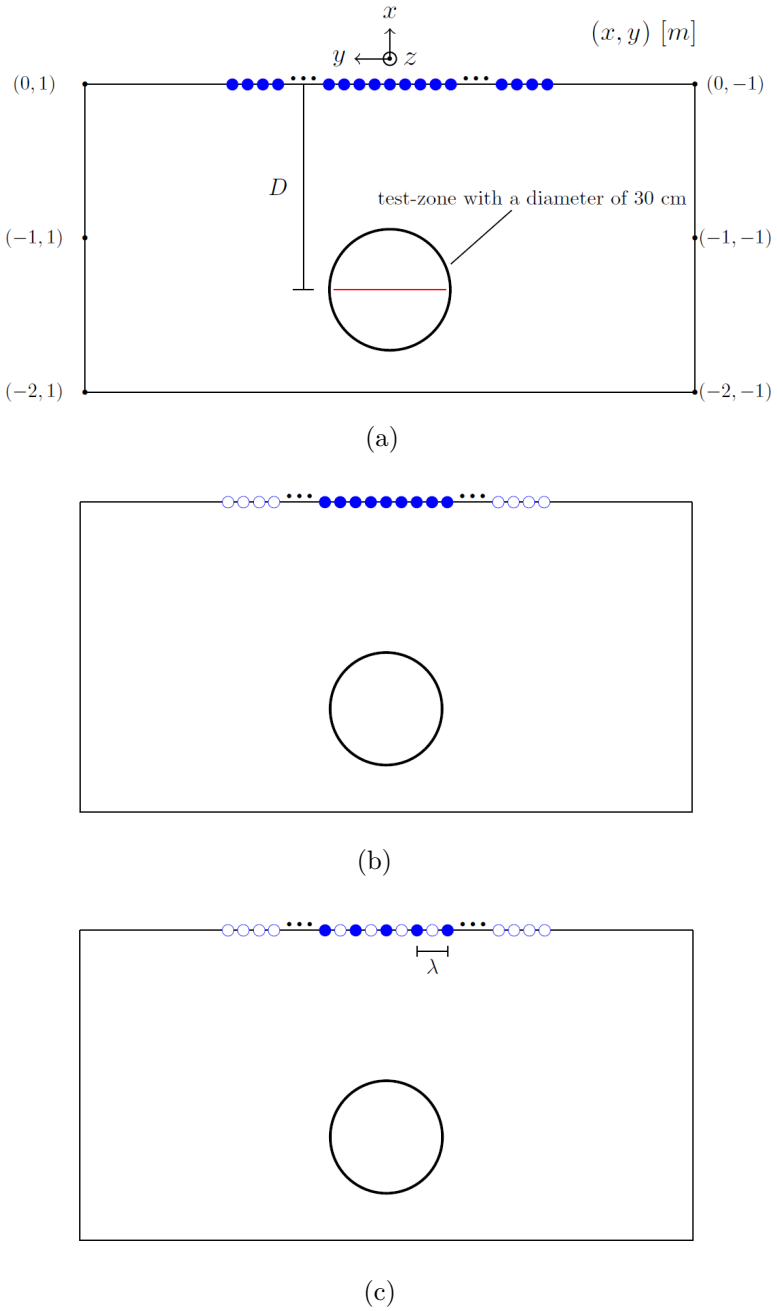

Figure 3.5: Calculation of the FoM's in the test zone for different linear arrays. (a) An array with 128 elements and $d = \frac{\lambda}{2}$ is considered. The center point of the test zone is located at the distance D from the center of the array that coincides with the origo. The diameter of the test zone is also indicated. (b) Three smaller arrays are considered by removing different number of sampling points at the ends of the 128 element array. (c) Thinner arrays are considered by considering the arrays in (b) and removing every second of the remaining sample points. Note that $d = \lambda$ for these arrays.

the mean according to equation (2.23). The phase spread was then found by taking the maximum value of the normalized phases.

The power- and phase spread was evaluated for $D = 1.0$ m, 1.5 m and 1.8 m. This was done to investigate how the performance of the arrays varied within the distance of $1 - 2$ m that was specified (see Section 1.1). However, since D is measured at the center of the test zone ($R = 15$ cm) and a 2 m $\times$ 2 m area was reconstructed, could no longer

Table 3.1: Summary of the arrays that were investigated in WSAP.

	Description	**Number of elements (N)**	**Element spacing (d)**
Array 1	No sample points removed	128	$\frac{\lambda}{2}$
Array 2	16 sample points removed on both ends of the array	96	$\frac{\lambda}{2}$
Array 3	24 sample points removed on both ends of the array	80	$\frac{\lambda}{2}$
Array 4	32 sample points removed on both ends of the array	64	$\frac{\lambda}{2}$
Array 5	Every second sample point removed	64	λ
Array 6	16 sample points removed on both ends of the array and every second of the reaming points removed	48	λ
Array 7	24 sample points removed on both ends of the array and every second of the reaming points removed	40	λ

distances than D= 2 m − 15 cm = 1.85 m be evaluated for the whole test zone to fall within the area. The array in Table 3.1 showing the best trade-off between containing as few elements as possible, while performing according to the specifications in Section 1.1 were then implemented in CST (Studio Suite 2017). An array with fewer elements will likely be less expensive to manufacture and was therefore desirable.

3.3 Simulation of the N-Slot SWA in CST

The linear array that was selected from Table 3.1 had N= 48 elements. The array was implemented as a standing wave slot antenna, where the slots are fed with a rectangular waveguide. The standing wave condition in the waveguide ensured that all slots were uniformly excited. This was important as the analysis performed in WSAP assumed that the linear array consisted of N identical antenna elements. The bandwidth of a SWA will generally start to decrease rapidly when more than just a few slots are used. Since each array in Table 3.1 consisted of tens of slots could the array not be designed using a single waveguide as the array then would become too narrowband. For that reason was it decided that the slot array instead should be realized by designing a smaller array section consisting of n slots (n<N), and then put several such sections in a *end-to-end* configuration (see Figure 3.8). Putting the sections end-to-end should yield uniform spacing between all N slots, which was important as the arrays in Table 3.1 have uniform element spacing. The spacing between the slots will be d= $\frac{\lambda_{g10}}{2}$, where λ_{g10} is the guided wavelength of the TE_{10} mode at 28 GHz. Since the guided wavelength is larger than the free space wavelength, was array 1-4 in Table 3.1 not possible to implement, i.e. the element spacing was too small. Array 5-7 in Table 3.1 could be implemented as the slot distance was smaller than the element distance of these arrays. This also meant that no grating lobes should appear for these arrays.

The smaller array section that will be designed will be refereed to as the ***n***-section.

The n-section was designed for as large S_{11} bandwidth as possible. The bandwidth of the n-section was always taken at the $-10\,\text{dB}$ level. The sidelobe level of the n-section should not be higher than $-9\,\text{dB}$ compare to boresight for reasonable good performance of the 48-slot array. The n-section should operate at a center frequency of 28 GHz.

The first step of designing the n-section was to choose a suitable waveguide. It was decided that a standard waveguide should be used rather than a waveguide with non-standard dimensions. The reason for this was driven by making the solution as cost-efficient and simple as possible. Standard waveguides can be bought directly at retailers while a waveguide with non-standard dimensions require special manufacturing.

Two standard waveguides, i.e. *WR-28* and *WR-34*, could be used at the operating frequency. Due to time constraints was only WR-28 considered for the design. The cut-off frequency of this waveguide is 21.6 GHz and the next mode start to propagate at approximately 42 GHz. The WR-28 guide was first simulated in CST to verify that only the TE_{10} mode was supported at 28 GHz. This was performed by allowing multiple modes to propagate in the guide and utilizing the *Port Mode* tool in CST to study the cut-off frequencies of the modes. The waveguide was simulated using a lossy material of Aluminum. The same material was used for all sections and structures that was constructed in CST. Copper and other more dense metals that are commonly used for waveguide was avoided in order to make the array cheaper to manufacture.

3.3.1 Investigation of the Slot Admittance

The next step of the design was to investigate the admittance of a single slot at resonance for different offset positions/ rotation angles. Three different types of slots were investigated; a longitudinal slot with rounded ends, a longitudinal slot with enlarged rounded ends, i.e. a dumbbell shaped slot and a compound slot placed on the narrow wall of the waveguide. These slot types will from now on be referred to as rounded, dumbbell and rotated slot throughout the thesis. The rounded slot was considered because slots in practical antennas usually have rounded ends due to the milling process used to make the slot. The dumbbell slot was considered for two reasons. The slot can easily be manufactured using the same milling process as for the rounded slot and then enlarge the ends by using a drill. The dumbbell slot has also shown to be more broadband. The rounded slot and dumbbell slots should be placed on the broad wall of the waveguide to yield vertical polarization. The same setup for both these slots could be used to investigate the admittance of the slots. The setup is shown in Figure 3.6.

A WR-28 guide was constructed in CST and the rounded slot or dumbbell slot was placed on the broad wall of the waveguide (see Figure 3.6). The length and width of the slots were controlled by the variables l and w. The distance between the center of the slots and the center line of the waveguide was controlled by δ_{pos}. The length of the slots was set to $\frac{\lambda}{2}$. For different values of δ_{pos} was the length of the slots varied around $\frac{\lambda}{2}$ by changing the value of δ_l. This was done in order to find the admittance of the slots at resonance for different offset positions. The S_{11} parameters was computed for each combinations of δ_{pos} and δ_l by utilizing the *Parameter Sweep* function in CST.

The δ_{pos} variable was swept between 0.1 mm and 1.3 mm while δ_l was swept from -1 mm to 1 mm. δ_{pos} and δ_l was incremented in steps of 0.1 mm and 0.2 mm, respectively. The computed S_{11} parameters were then exported as individual *Touchstone* files using the *Export* menu in CST. The parameters were normalized (note that normalized S_{11} is denoted as s_{11}) by the mean value of the waveguide impedance that was selectable in the

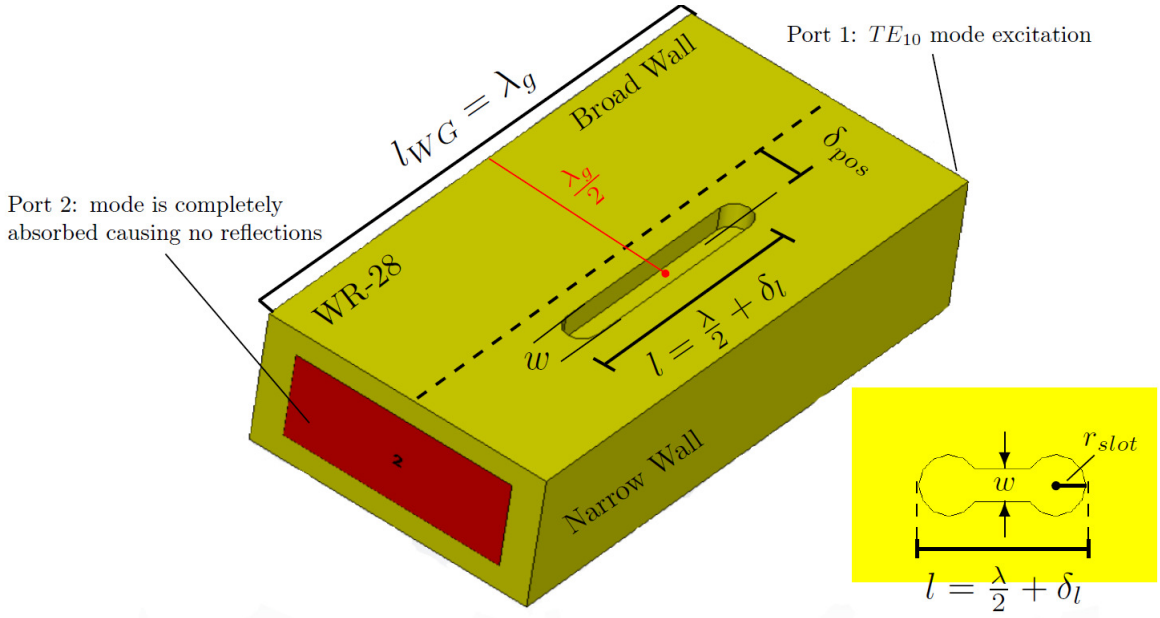

Figure 3.6: The setup in CST used to investigate the admittance of the rounded slot and dumbbell slot at resonance for different offset position δ_{pos}. All important features of the setup is indicated in the figure as well as the parameters describing the geometry of the two slots.

Export menu and automatically calculated by CST.

The Touchstone files were loaded to Matlab and the value of s_{11} at 28 GHz was extracted from each file. The extracted values were then sorted such that values corresponding to the same offset position were assigned to the same vector in Matlab. Thirteen vectors were created in total, i.e. one vector for δ_{pos}= 0.1 mm, δ_{pos}= 0.2 mm and so on. The s_{11}-parameters in each vector were then sorted such that the parameter corresponding to δ_l= −1 mm became the first vector element, δ_l= −0.8 mm the second and so on. The normalized admittance, y, corresponding to each s_{11}-parameter (equation [2.38]) was then calculated iteratively using each vector as input. The imaginary part of the calculated addmitances in the vectors was then studied manually. At resonance should the imaginary part of the slot admittance be equal to zero. The resonance should therefore occur between two consecutive elements in the vectors where the imaginary part change sign. The corresponding two δ_l elements could be used to estimate the value of δ_l corresponding to the resonance length of the slot. A table with the approximated resonance values of δ_l and y for the different offset positions was filled in. This table was used to select appropriate starting values, i.e. with respect to the design equation in (2.42), of δ_{pos} and δ_l when the n-section was designed.

The initial slot width was set to 1 mm for both the rounded, dumbbell and rotated slot. The radius, r_{slot}, of the dumbbell slot (see Figure 3.6) was chosen as 1.8 mm.

The length of the waveguide was set to $\lambda_{g_{10}}$ and the center of the slots were placed in the middle of the waveguide (indicated by the red line). The reason for these choices was that that a voltage maximum then would occur below the slot at the operation frequency. This mean that this particular length of the waveguide ensured that the slot would be excited in the same way as in the SWA (see Figure 2.23(a)). It was important that the TE_{10} mode incident at port 1 was not reflected at the other end of the waveguide, since this would result in a standing wave. The slots would in that case not be excited correctly. In a similar setup presented in [23] was a special absorbing boundary at the

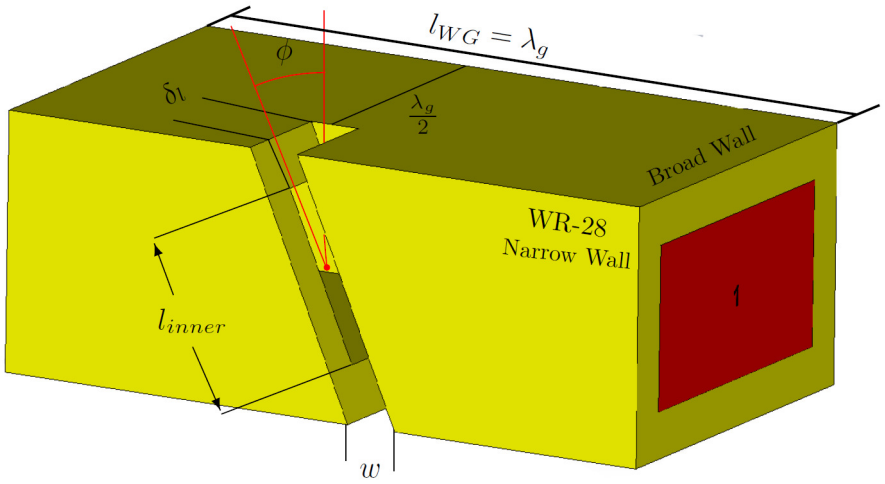

Figure 3.7: The setup in CST used to investigate the admittance of the narrow wall slot at resonance for different rotation angles ϕ. The length of the slot should be $\frac{\lambda}{2}$ and given by $l_{inner}+2\delta_l$, where l_{inner} is the inner length of the slot bounded by the narrow wall of the waveguide and δ_l is the distance that the slot cuts into the adjacent broad walls of the waveguide. w is the width of the slot. The variable l_{inner} depends on the rotation angle of the slot.

other end of the waveguide used to ensure that no standing wave was created. However, *wave ports* in CST absorbs a single incident mode completely. A standing wave was hence avoided by placing a wave port, i.e. port 2 in Figure 3.6, at the output of the waveguide. The admittance of the rotated slot was investigated in a similar manner. The setup is illustrated in Figure 3.7. The slot was placed on the narrow wall in the middle of the waveguide. The slot was rotated by the variable ϕ and for each rotation angle was the slot length varied around $\frac{\lambda}{2}$ by δ_l. The variable δ_l represents the distance that is cut into the broad walls by the slot. The total length of the slot was set to $\frac{\lambda}{2} = l_{inner}+2\delta_l$. A parameter sweep of ϕ and δ_l was preformed. Rotation angles between $10\,^\circ$ and $30\,^\circ$ with a step of $2\,^\circ$ were investigated. For each angle was l_{inner} measured by utilizing the *Picks* function in CST. The corresponding value of δ_l, yielding a slot length of $\frac{\lambda}{2}$, was then calculated. δ_l was varied $\pm 0.5\,\text{mm}$ from this value in order to find the resonance length of the slot. The s_{11}-parameters corresponding to the different combinations of ϕ and δ_l were then exported as Touchstone files. These files were processed and studied in the same manner as outlined in the previous paragraph. A table with resonance values of δ_l and y for the swept rotation angles of the slot were also created to be used in the design of the n-section.

3.3.2 The Configuration of the 48-Slot array

The next step of the design was to investigate the number of n-sections that could be used to implement the 48-slot array. The number of slots should yield an integer number of sections, i.e. $\frac{48}{n}$ should be an integer number. The number of slots that are used for each n-section determines whether the sections can be fed from the center or from the end. Figure 3.8 illustrate how the 48-slot array can be implemented depending on how many slots that are used for each section. If 48 or 24 slots are used in the n-section can the n-sections be fed from the center or from the end. If less elements in each n-section are used must each n-section be fed from the center. The reason for this is that the n-sections must be placed end-to-end in order to make the spacing between the slots

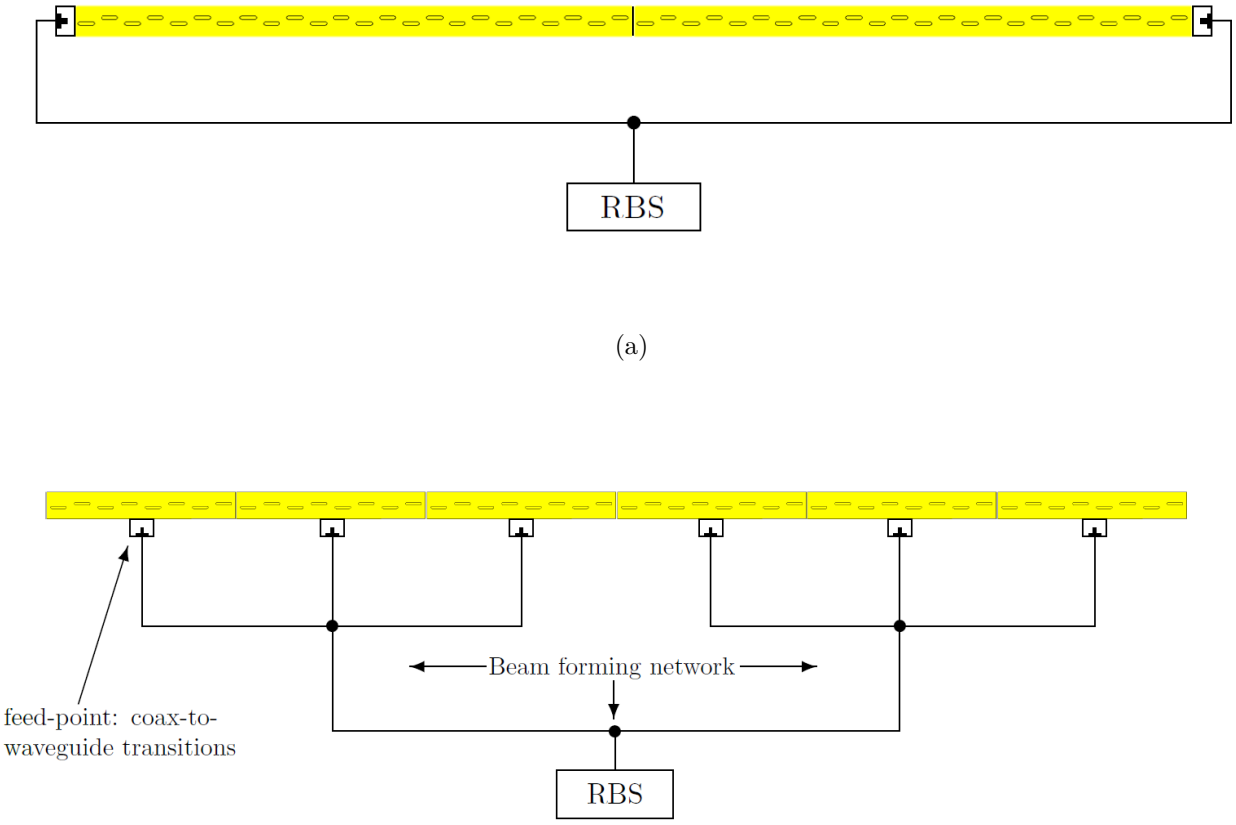

Figure 3.8: Illustration of an array with 48 slots being implemented by n-sections with different number of slots. (a) The array is implemented using two sections with 24 slots. Each section can be fed from the center or from the end. The end-fed case is illustrated. (b) The array is implemented by 6 sections, where each section has 8 slots. A schematic of the beamforming network and the RBS emulator used in the Random-LOS test setup are shown. A schematic of the transitions between the coaxial cables of the beamforming network and waveguides are also indicated.

uniform. This requirement make it impossible to use end-fed n-sections unless only one or two n-sections are used. In Figure 3.8, can it also be seen that each n-sections must be fed with a beamforming network that distribute signals from the RBS (see Section 2.3).

The largest section that was investigated had 12 slots. The other sections that were investigated had n= 4, 6 and 8 slots. Rounded slots were used for the n-sections. The reason for not consider the dumbbell and rotated slot at this stage was that only one of the n-sections were selected.

The n-sections were constructed and simulated in CST. The values of δ_{pos} and δ_l that gave as good match as possible, i.e. Re(y) closest to $\frac{1}{n}$, was selected from the table corresponding to the rounded slot. Short circuiting walls were placed at the ends of each section. An opening corresponding to the cross section of the WR-28 guide was made in the middle of each section (see Figure 3.9). The opening was made at the bottom wall of the waveguide and a wave port was placed at the opening. The length of the n-sections were set so that the general principles of placing the slots in a SWA could be adhered to, i.e. the two outer slots were placed $\frac{\lambda_{g_{10}}}{4}$ from the walls and $n-1$ slots were placed at the

intermediate distance of $d = \frac{\lambda_{g10}}{2}$ yielding a length of $l_{WG} = \frac{n}{2}\lambda_{g10}$ for each section.

The values of δ_{pos} and δ_l and the slot width, w, was tuned for each n-section using the *Optimization* tool in CST. The variables were optimized for maximal bandwidth. The bandwidth of the sections with 4 or 6 slots should be larger than sections with 8 or 12 slots. However, the sections with 8 or 12 slots should give a less expensive design as fewer sections need to be manufactured and a smaller beamforming network is required. The trade-off between bandwidth and cost was considered when the n-section was chosen. For clarity will the array section with the selected number of slots now be refereed to as the $\boldsymbol{n_s}$-section, where $\boldsymbol{s}$ denotes *selected*. $n_s = 8$ slots were considered for the remaining steps of the design.

3.3.3 Design of the n_s-Section

n_s-sections with dumbbell slots and rotated slots were first constructed and optimized for maximal bandwidth. Suitable values of δ_{pos} and δ_l were selected from the tables corresponding to the two slot types. These values along with the width of the slots were used in the optimization. For the dumbbell slot was the variable r_{slot} also used (see Figure 3.6). The bandwidth of the n_s-sections was characterized by three different frequencies denoted: f_{upper}, f_{lower} and f_{center}. The first two frequencies are the upper- and lower frequencies of the band. The third frequency are the center frequency of the band that was chosen at 28 GHz for each section. *Field Monitors* in CST was defined at these frequencies. The Field Monitors automatically generated plots of different far-field characteristic for one frequency of interest. One of the plots that was studied was the CO-polar radiation pattern from which the SLL could be read. The graphs generated by the Field Monitor also allowed one to check the polarization of each n_s-section. This was performed by studying the XP at two specific far-field cuts. The XP within $\phi_{az} = \pm 53\,^\circ$ and $\theta_{pol} = \pm 45\,^\circ$ from the boresight direction was studied for each n_s-section. This was done since only the radiation within this beam will illuminate the reflector. These angles assumed a reflector scaled for 28 GHz with dimensions $L_r = 80$ cm and $h_r = 60$ cm and that the linear feed is placed at $F = 30$ cm and is tilted θ_{feed} such that the boresight direction points at the center of the reflector. Note that a reflector with these particular dimensions has been suggested by RanLOS.

In order to compare the performance was end-fed versions of each n_s-section constructed and optimized for maximal bandwidth. A comparison revealed that the center-fed array sections actually were more narrowband than the end-fed counterparts. Since this contradicted the results from the open literature was a suspicion raised that the input port of the center-fed n_s-sections was poorly matched. In order to mitigate the mismatch should the waveguide impedance near the port be changed. This was done by introducing a metallic structure in the vicinity of the port (see Figure 3.9)

Three different structures were considered for each n_s-section. The first structure was a rectangle or *post* with height P_h, depth P_d and width P_w, placed just above the port on the inner top- and sidewall of the waveguide (see (1) in Figure 3.9). The other two structures considered was a *wedge* oriented according to the (2) and (3) in Figure 3.9. The depth, height and width of the wedge was changed by the variables W_d, W_h and W_w. Since the structures mainly effect the impedance locally, i.e. by changing the width of the guide, should the slots closest to the port be more effected by the structures than the other slots. The variables $\delta_{pos,c}/\phi_c$ and $\delta_{l,c}$ were introduced so that the offset position/rotation angle and the length of these slots could be changed separately from

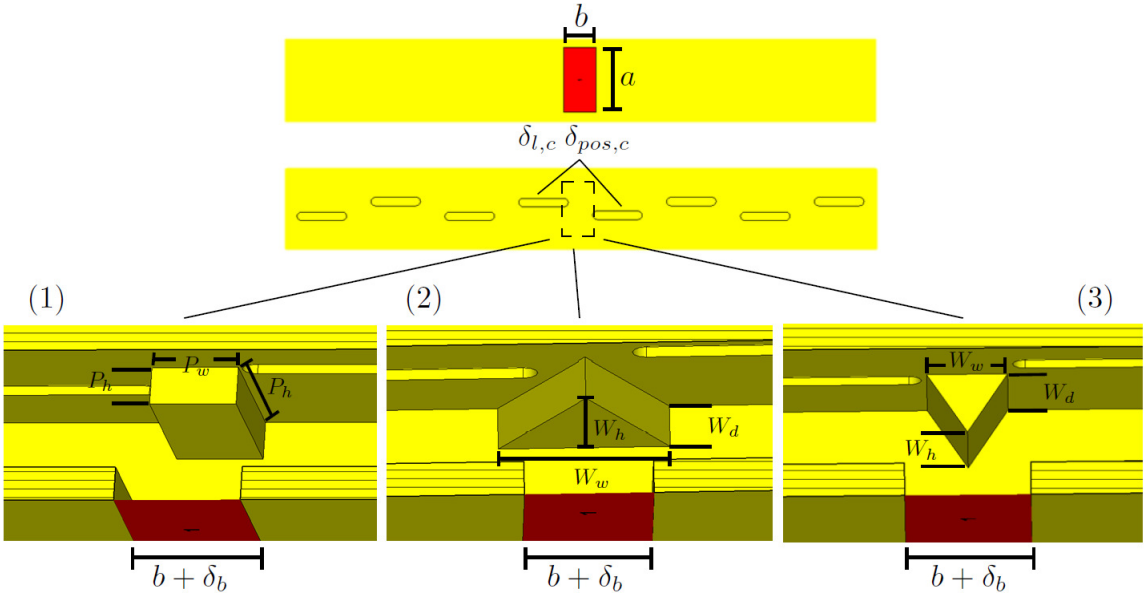

Figure 3.9: Mitigation of port mismatch of a center-fed n_s-section with rounded slots. A top and bottom view of the array section is shown. Three different structures (1)-(3) were placed above the port (red square) of the waveguide. The variables used to control the shape and size of each structure is indicated. To further mitigate the mismatch was the variable δ_b introduced so that the width of the wave port could be varied. The variables $\delta_{pos,c}$ and $\delta_{l,c}$ were also introduced so that the offset angle and length of the slots located closest to the port could be changed separately.

the other slots. The subscript c denotes the *center* position of the two slots. The port was set by the variables a and b corresponding to the cross sectional dimensions of the WR-28 guide (see Figure 2.15). The variable δ_b was introduced so that the port width could be varied. Each n_s-section was then optimized for maximal bandwidth using the variables mentioned in the previous paragraph along with the variables introduced in this paragraph. The structure yielding the largest bandwidth for respectively n_s-section was considered for the next step of the design.

The last step in the design was to put several n_s-sections with rounded, dumbbell, or rotated slots in the end-to-end configuration to implement the final 48-slot arrays (see Section 3.3.4). Before this was done was it however necessary to account for the thickness of the walls that were placed at the end of each n_s-section to yield the standing wave condition inside each waveguide.

Consider Figure 3.10 which show three n_s-section with rounded slots placed end-to-end. The distance between two outer slots placed on adjacent n_s-sections is indicated in the figure. The distance between all slots should be equal to $\frac{\lambda_{g10}}{2}$. However, the finite thickness of the metallic walls that are placed at the ends of each section, will cause the distance between the outer slots to be $\frac{\lambda_{g10}}{2}+\delta_d$. The variable δ_d is the total thickness of two walls. The walls are assumed to have the same thickness so that the thickness of one wall is $\frac{\delta_d}{2}$. In the simulations that has been performed previously has infinitely thin walls been used for each n_s-section. In order to account for the finite wall thickness was the ends of each section made shorter by $\frac{\delta_d}{2} = 0.508\,\text{mm}$, which corresponded to half the wall thickness of the WR-28 guide. Note that this distance was not selected for any particular reason and that another distance could also have been considered. The distance of $\frac{\delta_d}{2}$ that was removed on the ends of each section are indicated by the dashed lines in Figure 3.10.

After each n_s-section was made shorter was the bandwidth simulated again. The general result of shorting each n_s-sections were that the bandwidth decreased and that

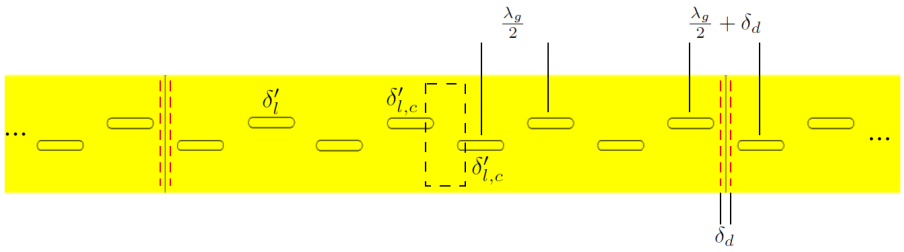

Figure 3.10: Three n_s-sections with rounded slots placed in an end-to-end configuration. The intermediate distance between the slots is $\frac{\lambda_{g10}}{2}$. To account for the larger intermediate distance between the outer slots on adjacent n_s-sections, was the ends of each section shorted by $\frac{\delta_d}{2}$. This distance is indicated by the dashed lines. The variables δ_l and $\delta_{l,c}$ were also changed in order to make the resonance of the shorted n_s-sections to occur at 28 GHz.

f_{center} was shifted towards 29 GHz. It was concluded that the shorted waveguide itself introduced a shift of the resonance frequency of the slots and increased the mismatch at the port. To compensate for the shift was the lengths of the rounded, dumbbell and rotated slots in the n_s-sections shorted so that the resonance would occur at 28 GHz again. This was done by changing the values of δ_l and $\delta_{l,c}$ that were optimized for each n_s-section so that the resonance would occur at 28 GHz and the bandwidth would be as large as possible.

3.3.4 The final 48-slot arrays

Each n_s-section with rounded, dumbbell and rotated slots were placed in an end-to-end configuration to implement 48-slot arrays with respectively slot type. This was done by copying and translating each n_s-section with the *Translate* tool in CST. The simulation of each 48-slot array was performed by exciting the wave ports of the constituent n_s-sections simultaneously with uniform excitation. This setting was chosen in *Selection* under the *Setup Solver* menu in CST. The radiative performance of each 48-slot array, i.e. the CO-polar radiation patter, was then investigated in the same way as outlined in Section 3.3.3.

4
Results

The results presented in this chapter are divided into two main parts. In the first part, are the results obtained from the preliminary study presented. In the second part, are designs of the 48-slot arrays in CST presented. In the first part are the results weighted according to importance, meaning that the results that are most significant for the second part are presented first, followed by less significant results. In the second part are the results not weighted in this fashion. Rather are the results presented chronologically, meaning that the results are presented in the order that they would be obtained when following the design steps that are outlined in Section 3.3.

4.1 WSAP and Matlab

The calculated power- and phase spread corresponding to the linear arrays in Table 3.1 are shown in Table 4.1.

Table 4.1: Calculated power- and phase spread for the linear arrays in Table 3.1.

	D= 1.0 m		D= 1.5 m		D= 1.8 m	
	σ_{dB}	$\Delta\phi_{max}$	σ_{dB}	$\Delta\phi_{max}$	σ_{dB}	$\Delta\phi_{max}$
Array 1	0.6 dB	6 °	0.6 dB	7 °	0.6 dB	8 °
Array 2	0.7 dB	9 °	0.8 dB	11 °	0.9 dB	8 °
Array 3	0.9 dB	12 °	0.9 dB	16 °	0.9 dB	14 °
Array 4	1.1 dB	15 °	1.3 dB	12 °	1.3 dB	15 °
Array 5	0.9 dB	7 °	1.1 dB	8 °	1.0 dB	10 °
Array 6	0.8 dB	9 °	0.8 dB	9 °	0.9 dB	9 °
Array 7	0.9 dB	14 °	1.0 dB	17 °	0.9 dB	15 °

It can be seen that Array 6 gives the best performance relative to the number of elements, i.e. N= 48. As stated in Section 3.2 is a low number of antenna elements desirable for cost reasons if the array were to be constructed in the future. This array is therefore chosen to be implemented as an standing wave slot array in CST.

In addition to the arrays listed in Table 3.1, are some smaller linear arrays investigated in order to estimate the minimum number of antenna elements that is required to achieve acceptable variation of the field within the test zone. The smaller arrays that are investigated consist of 24 and 36 elements with an spacing of λ. A single antenna element is also studied to compare with the performance of the smaller arrays. The power- and phase variation of the radiated field corresponding to the single antenna element and the arrays with 24 and 36 elements are shown in Figure 4.1.
Note that P_{norm} is displayed on the bar scales next to the power plots in Figure 4.1. This implies that the power of each field samples, P_{samp}, is normalized with the mean of all

Table 4.2: Calculated power and phase spread when an array with $N = 1$, $N = 24$ and $N = 36$ antenna elements is considered in WSAP.

	$N = 1$		$N = 24$		$N = 36$	
	σ_{dB}	$\Delta\phi_{max}$	σ_{dB}	$\Delta\phi_{max}$	σ_{dB}	$\Delta\phi_{max}$
$D = 1.0\,\mathrm{m}$	0.7 dB	198 °	2 dB	33 °	1.2 dB	16 °
$D = 1.5\,\mathrm{m}$	0.6 dB	186 °	2.9 dB	24 °	1.8 dB	16 °
$D = 1.8\,\mathrm{m}$	0.5 dB	179 °	3.2 dB	16 °	2.1 dB	15 °

P_{samp} values corresponding to positions within the test zone. The reason for normalizing the field samples is so that the power variations of the test zone will appear more clear. It can also be seen in Figure 4.2 that the radius of the test zone is $R = 15\,\mathrm{cm}$ and the diameter is indicated by red line. The blue dot(s) represents the sample points for the different case; one sample point for $N = 1$ and multiple sample point for the arrays. The distance, D, between the diameter and the sample point(s) is 1 m in the figures. The power-and phase spread achievable at this distance and at $D = 1.5\,\mathrm{m}$ and $D = 1.8\,\mathrm{m}$ are displayed in Table 4.2.

The achievable phase variation along the diameter when the linear arrays in Table 4.2 are used, is illustrated in Figure 4.2. A distance of $D = 1\,\mathrm{m}$ is considered in this figure. It can be seen that ϕ_{norm} is displayed on the vertical axis. This indicate that the phase of the field samples are normalized by their mean.

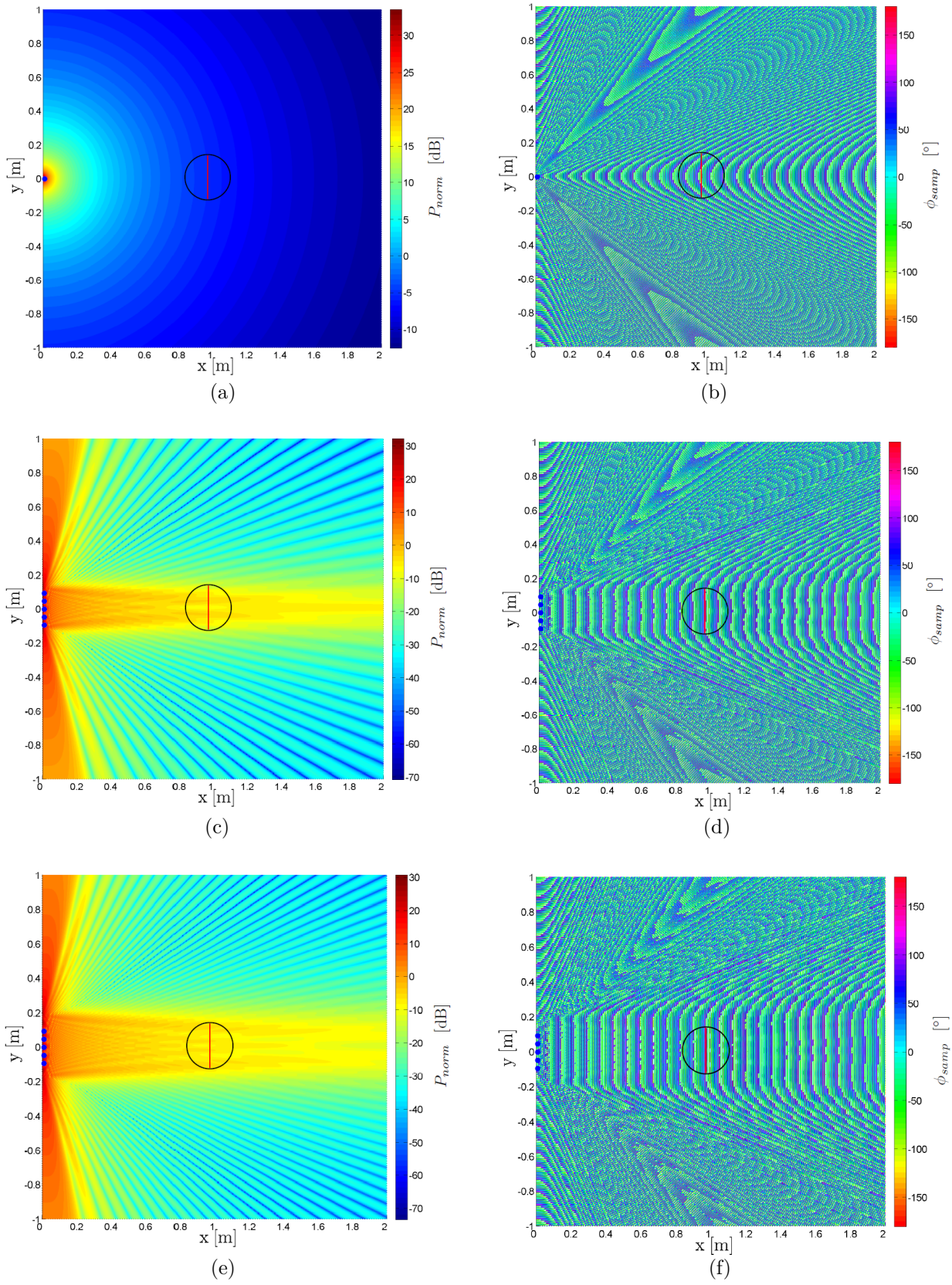

Figure 4.1: Plot of power and phase over a 2 m × 2 m area from a linear array located in front of the area. (a) and (b) Power and phase from an array with one antenna element. (c) and (d) Power and phase from an array with 24 antenna elements. (e) and (f) Power and phase from an array with 36 antenna elements.

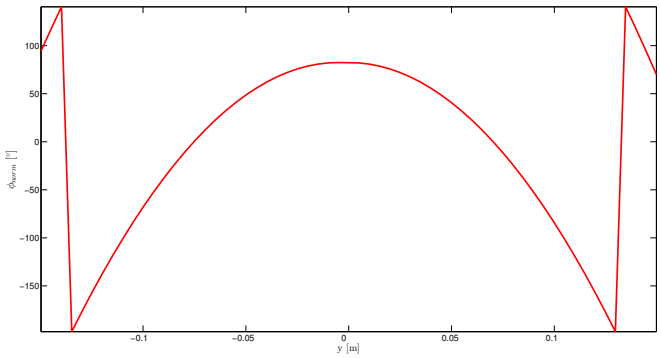

(a)

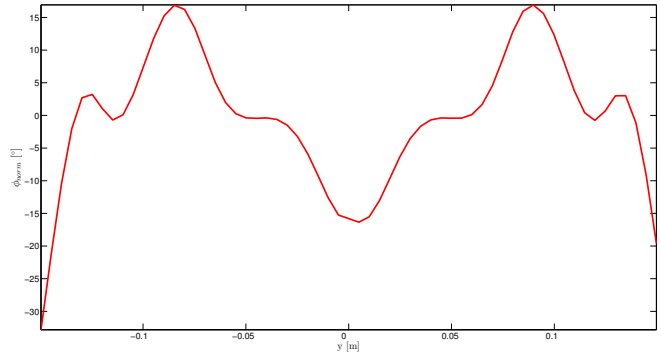

(b)

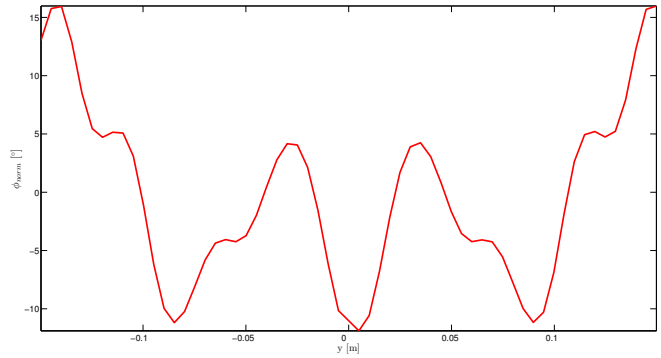

(c)

Figure 4.2: Achievable variation along the diameter of the test zone located at $D = 1\,\mathrm{m}$ when (a) single antenna element is used. (b) Array with 24 elements is used. (c) Array with 36 elements is used.

4.2 The N-Slot SWA in CST

The first step of the design is to investigate the resonance of the slot impedance. This is done for different offset positions or rotation angles of the slot types. This step is performed so that an appropriate value of δ_{pos}/ϕ with respect to (2.42) may be chosen for the initial design of the SWA sections with different number of slots. The impedance of the rounded, dumbbell and rotated slots for different combinations of the δ_{pos}/ϕ and slot lengths are shown in Table 4.3,4.4 and 4.5. Note that the lengths are not shown explicitly in the Tables. Instead is the offset, δ_l, from the nominal resonance length of the slot, i.e. $\frac{\lambda}{2}$, displayed. Consequently, $+(-)\delta_l$ in the Tables means that the slot is δ_l longer (shorter) than the nominal length. The third and fourth column show the real- and imaginary part of the slot impedance for each δ_{pos}/ϕ and δ_l combination. Note that two values of δ_l, corresponding to subsequent points in the Parameter Sweep where resonance occurs between the points, are displayed for each value of δ_{pos}/ϕ. This allow for the value of δ_l, corresponding to resonance of the each slot, to be estimated. Table 4.3 displays a larger set of values than the other two Tables. The reason for this is that Table 4.3 is used for the design of array sections with 4, 6, 8 and 12 slots, while the other Tables only are used for sections with 8 slots.

Table 4.3: Investigation of the resonance addmittance of a rounded slot. The values correspond to a parameter sweep of δ_{pos} and δ_l that is performed in CST using the setup depicted in Figure 3.6.

δ_{pos} [mm]	δ_l [mm]	Re(y) [S]	Im(y) [S]
0.4	−0.2	0.030	0.002
	0	0.064	−0.062
0.5	−0.2	0.047	0.023
	0	0.100	−0.010
0.6	0	0.140	0.006
	0.2	0.124	−0.090
0.7	0	0.184	0.028
	0.2	0.173	−0.104
0.8	0	0.237	0.051
	0.2	0.256	−0.111
0.9	0	0.283	0.081
	0.2	0.299	−0.117
1.0	0	0.325	0.117
	0.2	0.366	−0.123
1.1	0	0.365	0.161
	0.2	0.440	−0.099
1.2	0	0.401	0.217
	0.2	0.523	−0.081
1.3	0	0.447	0.267
	0.2	0.607	−0.057

Table 4.4: Investigation of the resonance addmittance of a dumbbell slot. The values correspond to a parameter sweep of δ_{pos} and δ_l that is performed in CST using the setup depicted in Figure 3.6.

δ_{pos} [mm]	δ_l [mm]	Re(y) [S]	Im(y) [S]
0.7	−0.8	0.165	0.036
	−0.6	0.180	−0.125
0.8	−0.8	0.206	0.067
	−0.6	0.228	−0.137
0.9	−0.8	0.254	0.003
	−0.6	0.291	−0.072

Table 4.5: Investigation of the resonance addmittance of a rotated slot. The values correspond to a parameter sweep of ϕ and δ_l that is performed in CST using the setup depicted in Figure 3.7.

ϕ [°]	δ_l [mm]	Re(y) [S]	Im(y) [S]
18	0.22	0.184	0.104
	0.24	0.203	−0.121
20	0.22	0.217	0.009
	0.24	0.238	−0.074
22	0.22	0.262	0.092
	0.24	0.288	−0.134

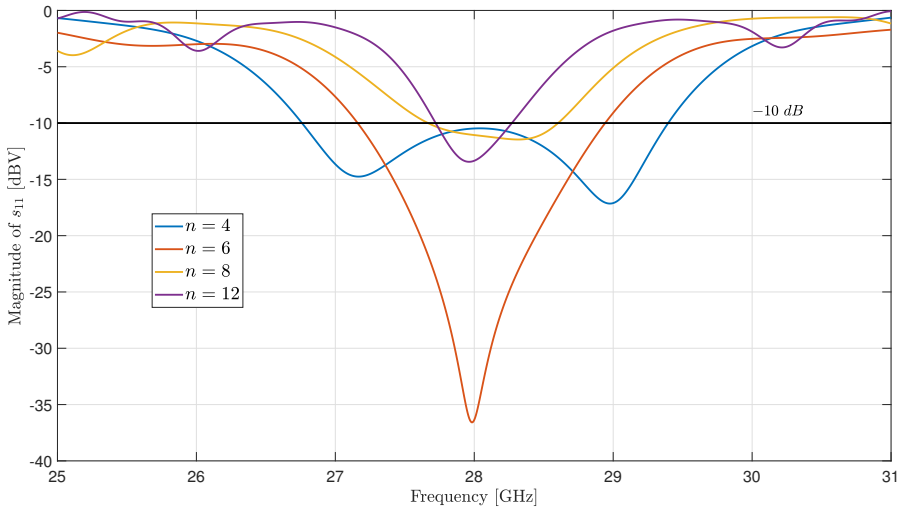

Figure 4.3: Return loss of a center-fed SWA section with n= 4, 6, 8 and 12 slots.

The next step of the design is to determine the number of slots, n, to use for each section. The return loss, i.e. the −10 dB bandwidth, Δf_{-10dB}, for one center-fed section with n= 4, 6, 8 and 12 slots is shown in Figure 4.3. Note that only rounded slots are considered for these sections and that the geometry of each section is optimized in CST to yield as large Δf_{-10dB} as possible.

After the appropriate number of slots is decided, i.e. n=n_s= 8, see Section 3.3.2, are n_s-sections with dumbbell and rotated slots also constructed. The design parameters of the n_s-section with the different slot types are displayed in Table 4.6. Design parameters that are deterministic, i.e. not optimized in CST, are not displayed in the Tables. This includes the slot spacings (see Section 2.4.4), length of the waveguide (l_{WG}= $\frac{n_s}{2}\lambda_{g10}$) and the cross sectional dimension of the waveguide (WR-28). The parameters in Table 4.6

Table 4.6: Optimized parameters for the n_s-sections.

Type of slot used for n_s-section	Parameter Name	Parameter Value
Rounded	δ_{pos}	0.70 mm
	δ_l	0.10 mm
	l	5.45 mm
	w	1.00 mm
Dumbbell	δ_{pos}	0.73 mm
	δ_l	−0.63 mm
	l	4.72 mm
	r_{slot}	1.72 mm
	w	0.95 mm
Rotated	ϕ	18.20 °
	δ_l	0.25 mm
	l_{inner}	3.74 mm
	l	4.59 mm
	w	0.70 mm

are optimized to yield the largest possible value of Δf_{-10dB} of each section. The return loss of the n_s-section with rounded, dumbbell and rotated slots is shown in Figure 4.4(a), 4.4(c) and 4.4(e). Note that the return loss of the section with rounded slots is shown both in Figure 4.3 and 4.4(a)
It can be seen that f_{lower}, f_{center} and f_{upper}, are used to characterize Δf_{-10dB}. The center frequency (marked in red color) is set at 28 GHz even though it clearly in Figure 4.4(a) and 4.4(c) can be seen to not represent the actual center frequency of the bands. The bandwidth of the n_s-section with rounded, dumbbell and rotated slots is Δf_{-10dB}= 1.03 GHz, Δf_{-10dB}= 0.95 GHz and Δf_{-10dB}= 0.61 GHz.

The radiative performance, i.e. radiation pattern and XP, are evaluated for each section at f_{lower}, f_{center} and f_{upper}. The CO-polar radiation pattern of the n_s-section with rounded, dumbbell and rotated slots are shown in Figure 4.4(b), 4.4(d) and 4.4(f). Note that the ϕ_{az}= 0 ° cut is displayed for the n_s-section with rounded/dumbbell slots, while the ϕ_{az}= 90 ° cut is shown for the n_s-section with rotated slots. To keep the number of plots in this Section to a reasonable level is only the pattern at f_{center} shown. This does also apply in generally for all other plots that are part in evaluating the radiative performance of the n_s-sections and the final 48-slot arrays. The SLL in Fig.4.4(b), 4.4(d) and 4.4(f) is −12.3 dB, −13.0 dB and −17.4 dB

The quality of the polarization, i.e. how linear it is, is determined from studying the XP. The XP is displayed in Figure 4.5 for each section. Two far-field cuts, one with constant values of ϕ_{az} and one with constant value of θ_{pol}, are considered. Note that the specific cut values of ϕ_{az} and θ_{pol} are indicated in the captions to each Figure. The boresight direction is indicated with a red dashed line. The black dashed line(s) in the figures indicate the angle from boresight for which the XP is studied. These angles, i.e. ϕ_{az}= ±53 ° and θ_{pol}= 45 °, defines the beam of interest (see Section 3.3.3) that is assumed to illuminate the reflector used in the test setup.

End-fed n_s-sections are also built and optimized in CST. The return loss of the end-fed sections and the center-fed sections are compared in Figure 4.6. The consistently larger value of Δf_{-10dB} achievable with the end-fed counterparts suggest that the center-fed sections are poorly matched at the input port. In order to mitigate the mismatch

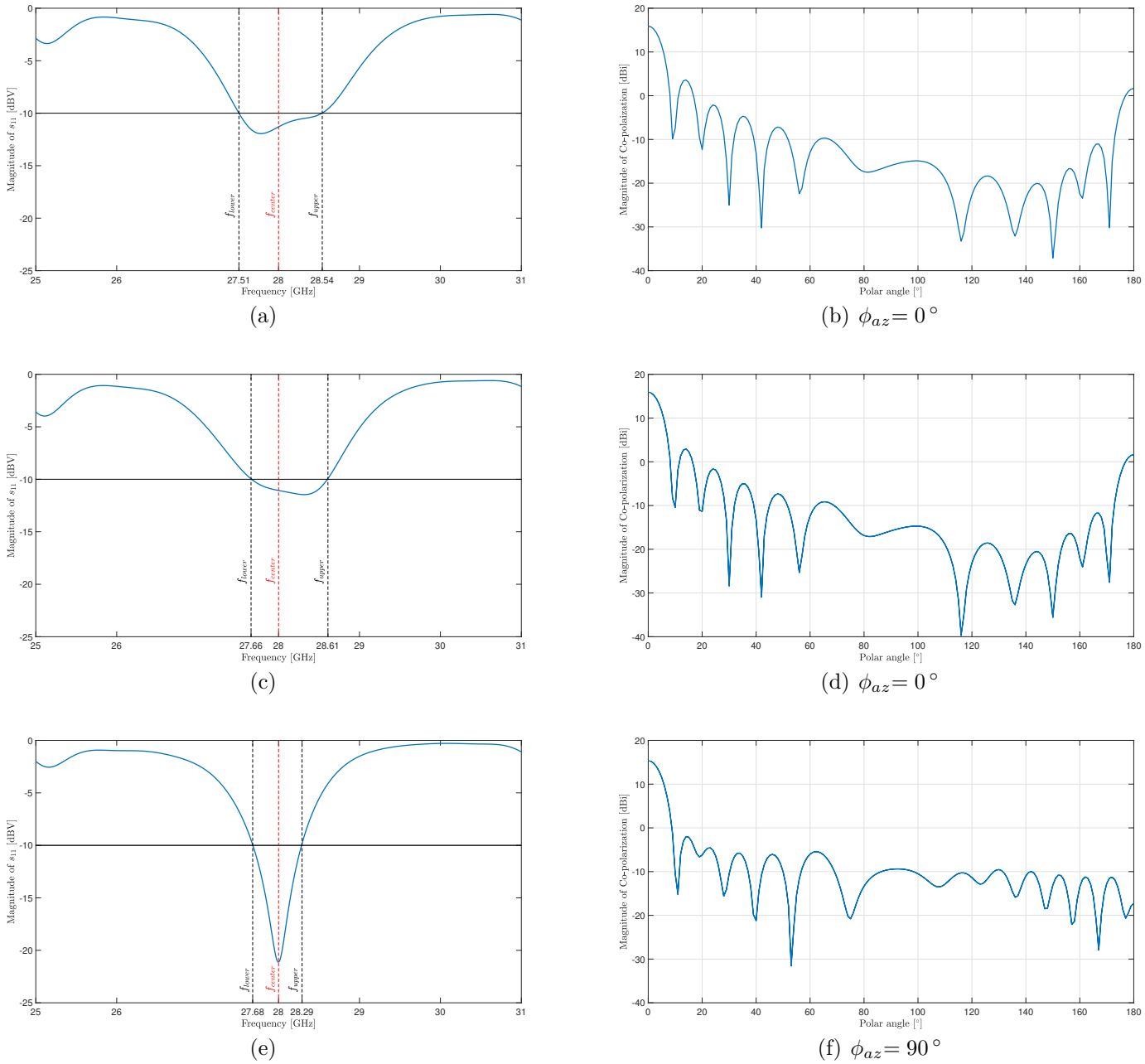

(a) (b) ϕ_{az}= 0 °

(c) (d) ϕ_{az}= 0 °

(e) (f) ϕ_{az}= 90 °

Figure 4.4: Return loss (a,c,e) and CO-polar radiation pattern (b,d,f) for the n_s-section with (a)-(b) rounded slots, (c)-(d) dumbbell slots and (e)-(f) rotated slots. The three frequencies, f_{lower}, f_{center} and f_{upper}, used to characterize Δf_{-10dB} are marked. The radiation pattern is plotted for ϕ_{az}= 0 ° or ϕ_{az}= 90 °.

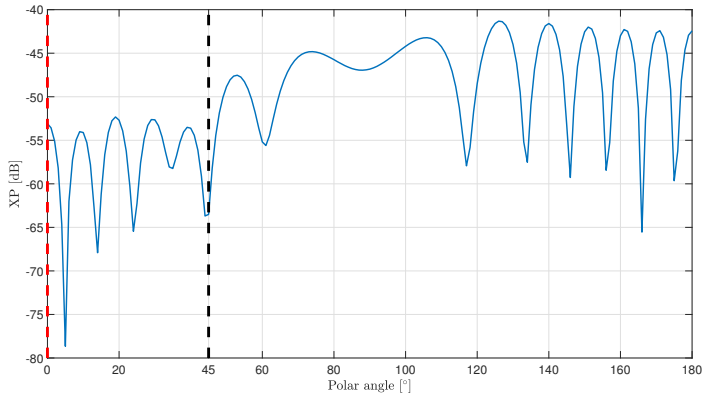

(a) ϕ_{az}= 0 °

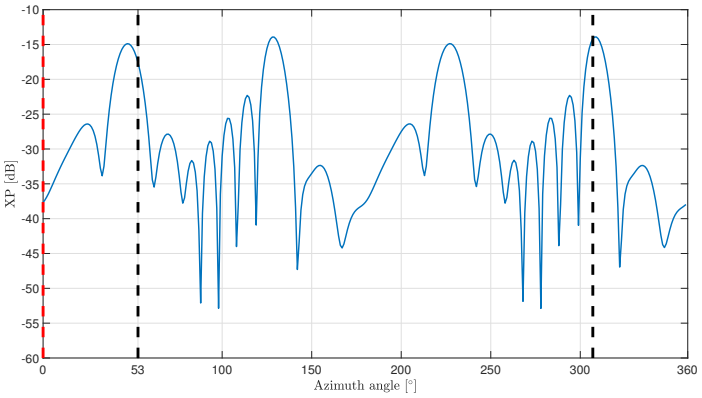

(b) θ_{pol}= 90 °

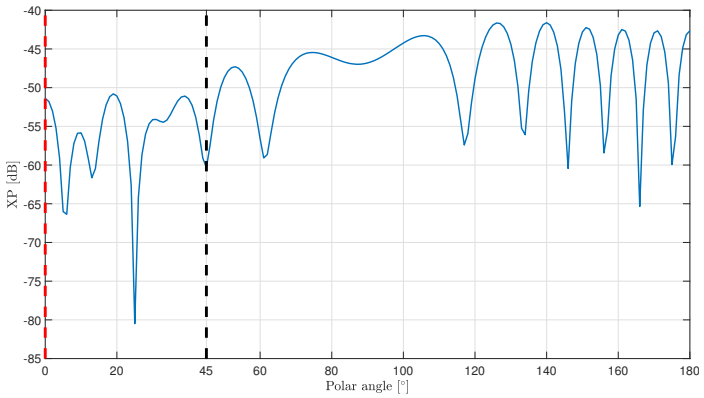

(c) ϕ_{az}= 0 °

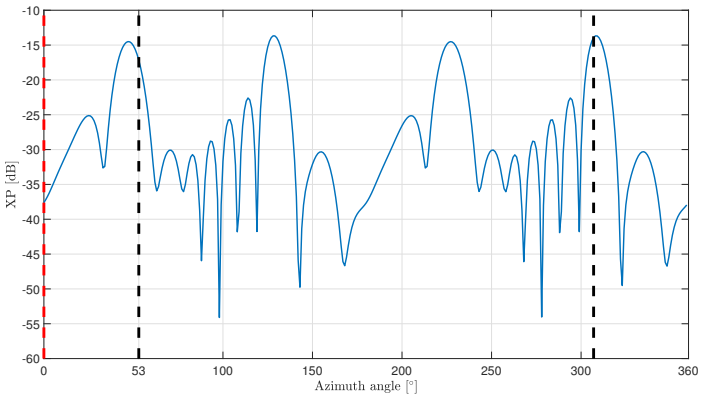

(d) θ_{pol}= 90 °

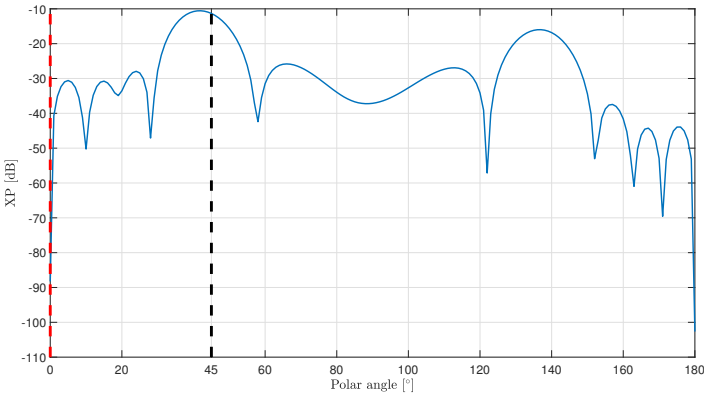

(e) ϕ_{az}= 90 °

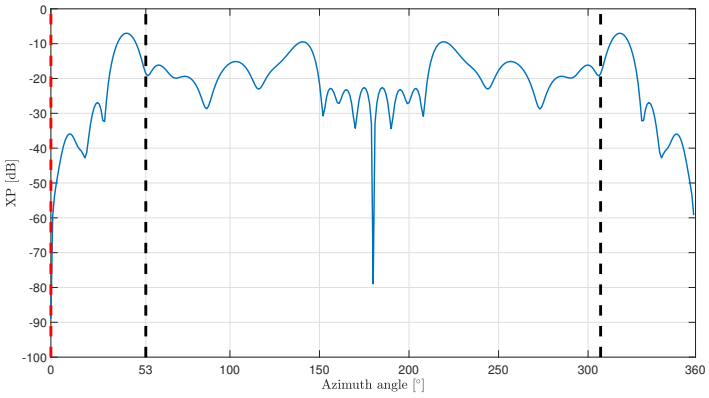

(f) θ_{pol}= 90 °

Figure 4.5: XP for the n_s-section with rounded, dumbbell and rotated slots. The ϕ_{az}= 0 ° and θ_{pol}= 90 ° cuts are considered for the sections with rounded (a)-(b) and dumbbell (c)-(d) slots, while the ϕ_{az}= 90 ° and θ_{pol}= 90 ° cut are considered for the section with rotated slots (e)-(f). The red dashed line represent the boresight direction and the black line/lines represents the angles ϕ_{az}= ±53 ° or θ_{pol}= 45 ° from boresight for which the XP is studied.

is a metallic structure introduced at the port. The variables $\delta_{pos,c}/\phi_c$, $\delta_{l,c}$ and δ_b (see Section 3.3.3) are also introduced for the n_s-sections. The new variables are optimized together with the variables listed in Table 4.6. The variables of the mitigated n_s-sections are displayed in Table 4.7. The return loss of the the mitigated n_s-sections are displayed

Table 4.7: Optimized parameters of the n_s-sections that is mitigated for port mismatch.

Type of slot used for n_s-section	Parameter Name	Parameter Value
Rounded	δ_{pos}	0.86 mm
	$\delta_{pos,c}$	0.86 mm
	δ_l	0.10 mm
	$\delta_{l,c}$	0.12 mm
	l	5.46 mm
	l_c	5.48 mm
	w	0.95 mm
	δ_b	0.1 mm
	P_d	4.57 mm
	P_h	1.11 mm
	P_w	2.50 mm
Dumbbell	δ_{pos}	0.82 mm
	$\delta_{pos,c}$	0.82 mm
	δ_l	−0.64 mm
	$\delta_{l,c}$	−0.61 mm
	l	4.72 mm
	l_c	4.75 mm
	r_{slot}	1.55 mm
	w	0.86 mm
	δ_b	0.15 mm
	W_d	5.98 mm
	W_h	2.46 mm
	W_w	3.02 mm
Rotated	ϕ	19.98 °
	ϕ_c	20.90 °
	δ_l	0.22 mm
	$\delta_{l,c}$	0.22 mm
	l_{inner}	3.80 mm
	$l_{inner,c}$	3.78 mm
	l	4.59 mm
	l_c	4.57 mm
	w	0.70 mm
	δ_b	0.16 mm
	W_d	5.00 mm
	W_h	1.43 mm
	W_w	2.75 mm

in Figure 4.6. The bandwidths for the mitigated section with rounded, dumbbell and rotated slots are Δf_{-10dB}= 1.68 GHz, Δf_{-10dB}= 1.66 GHz and Δf_{-10dB}= 0.78 GHz.

When multiple n_s-sections are put in the end-to-end configuration to implement the 48-slot array, will the arrays be longer than L_f. This is due to the finite thickness of the metallic walls at the ends of each section. In order to account for the wall thickness are each section shorted at the ends. The return loss of the shortened n_s-sectioned is shown in Figure 4.7.

It can be seen that the shorter waveguides introduces a shift of the bands towards 29 GHz and that it particularly affects the longitudinal slots in Figure 4.7(a) and 4.7(b). It

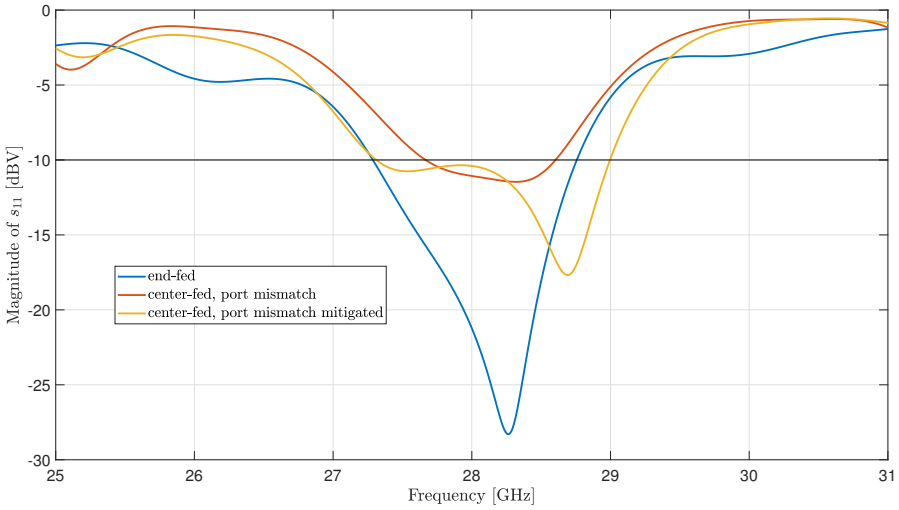

(a)

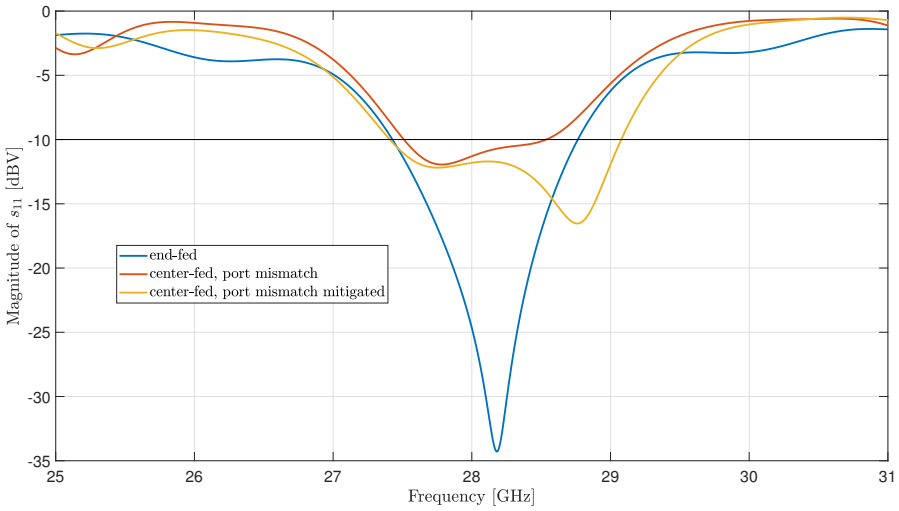

(b)

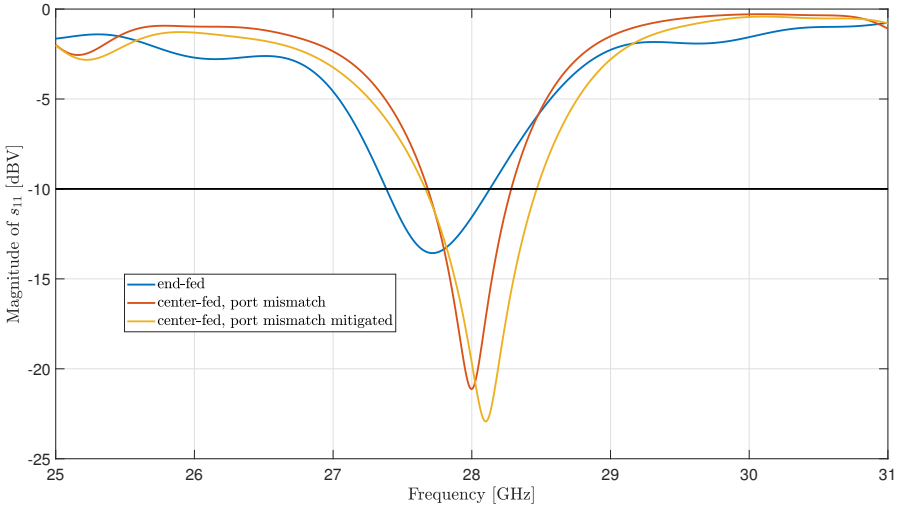

(c)

Figure 4.6: Return loss for end-fed n_s-section, center-fed n_s-section and center-fed n_s-section mitigated for port mismatch. (a) n_s-section with rounded slots. (b) n_s-section with dumbbell slots. (c) n_s-section with rotated slots.

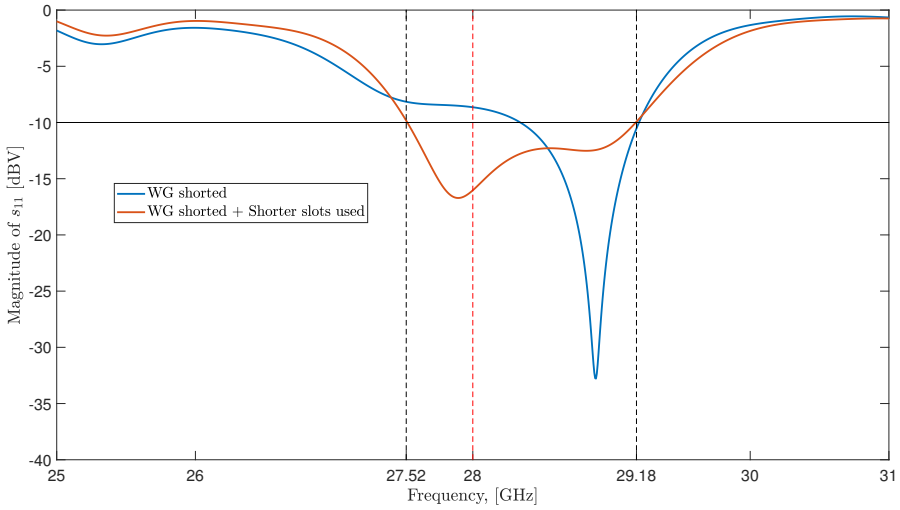

(a)

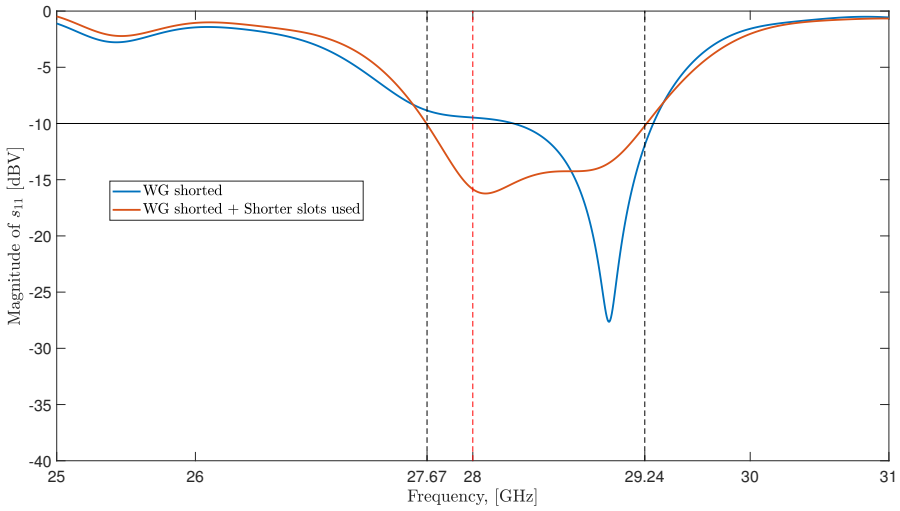

(b)

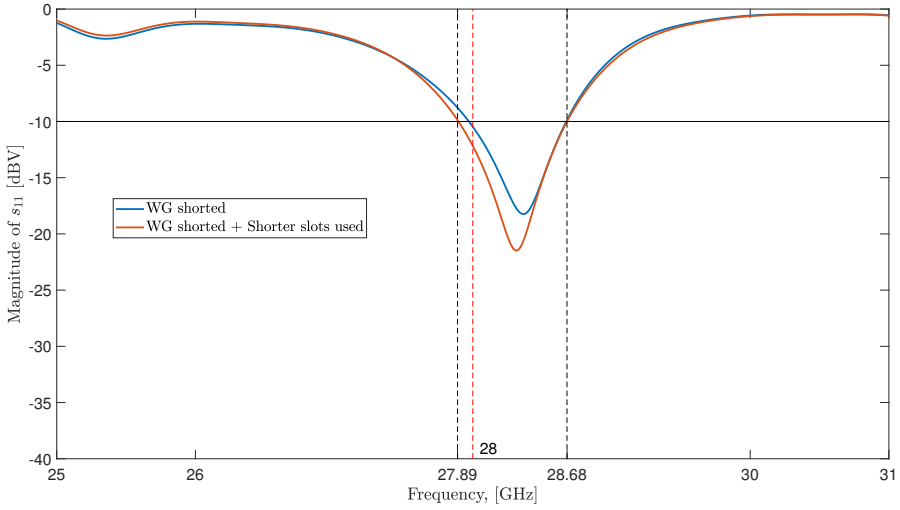

(c)

Figure 4.7: Return loss for when the n_s-section has been made shorter by $\frac{\delta d}{2}$ at both ends and when the slots also has been made shorter. (a) n_s-section with rounded slots. (b) n_s-section with dumbbell slots. (c) n_s-section with rotated slots.

Table 4.8: Optimized parameters for the shorter n_s-sections.

Type of slot used for n_s-section	Parameter Name	Parameter Value
Rounded	δ_l	0 mm
	$\delta_{l,c}$	−0.1 mm
	l	5.35 mm
	l_c	5.25 mm
Dumbbell	δ_l	−0.7 mm
	$\delta_{l,c}$	−0.8 mm
	l	4.65 mm
	l_c	4.55 mm
Rotated	δ_l	0.20 mm
	$\delta_{l,c}$	0.19 mm
	l	4.55 mm
	l_c	4.51 mm

can also be seen that the shortening increase the mismatch making the bands more narrow. These two problems can be solved by making the slots shorter so that they resonate at a higher frequency. The shift toward the higher resonance frequency partially counteracts the shift introduced by the shorter waveguides. The return loss after the slots has been made shorter is displayed in Figure 4.7. The bandwidth of the n_s-section with rounded, dumbbell and rotated slots are seen to be Δf_{-10dB}= 1.66 GHz, Δf_{-10dB}= 1.57 GHz and Δf_{-10dB}= 0.79 GHz. The parameters corresponding to the shorter slots are given in Table 4.8. Note that the other parameters that are given in Table 4.7 also are used for the shorter waveguide sections.

Finally, the radiative performance of the 48-slot array is evaluated. The array are implemented by placing 6 shorted n_s-sections with respectively slot type end-to-end. The CO-polar radiation pattern and XP is shown for each 48-slot array in Figure 4.8 and 4.9. A set of three or six graphs is displayed in these figures. The order of the graphs, from top to bottom, is as follows; the 48-slot array with rounded slots is displayed first, followed by the 48-slot array with dumbbell slots and finally the 48-slot array with rotated slots. Note that the CO-polar radiation pattern in Figure 4.8(a),4.8(b) and 4.8(c) is plotted for θ_{pol} ranging from −180 ° to 180 °. The SLL in these figures is −14.7 dB, −14.6 dB and −17.8 dB.

4.3 Simulated result when using the 48-slot array with an reflector

The results that were obtained when using one of the arrays with a cylindrical reflector scaled for 28 GHz, are presented in Appendix A.4. The results was obtained using the embedded radiation pattern of one of the slots in the arrays. The results are thus relevant too, but nonetheless outside the scope of this thesis. Furthermore, the results was generated using Matlab code that was written by Aidin Razavi and Madeline Schilliger Kildal does so not belong in this Chapter where results produced at least partly by the author should be presented.

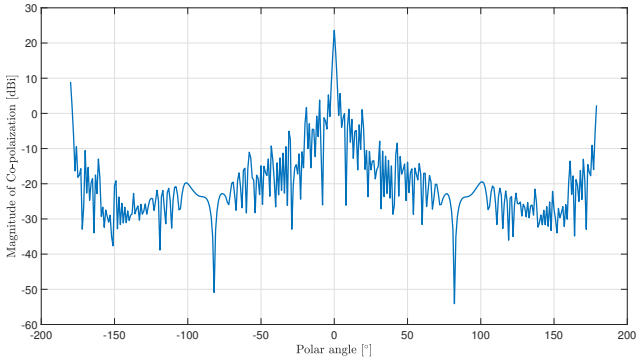

(a) $\phi_{az} = 0\,°$

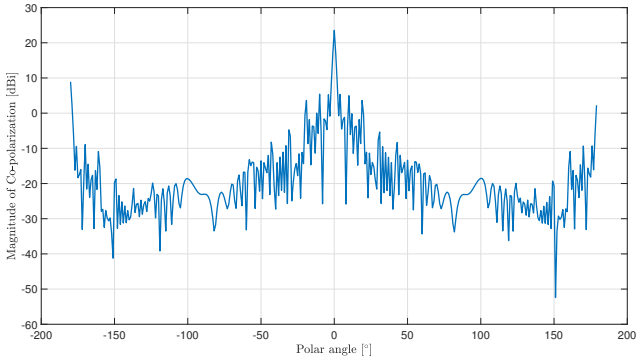

(b) $\phi_{az} = 0\,°$

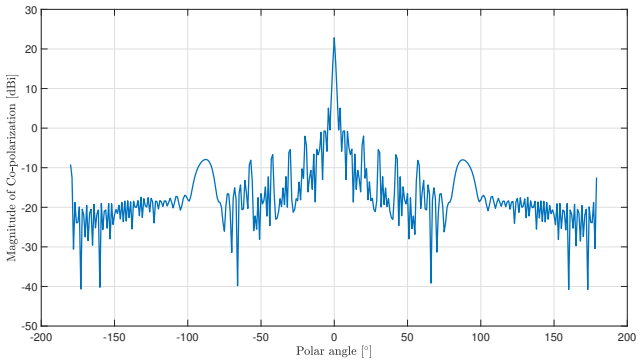

(c) $\phi_{az} = 90\,°$

Figure 4.8: Return loss of the CO-polar radiation pattern for the 48-slot array with (a) rounded slots, (b) dumbbell slots and (c) rotated slots. The radiation pattern is plotted for $\phi_{az} = 0\,°$ or $\phi_{az} = 90\,°$.

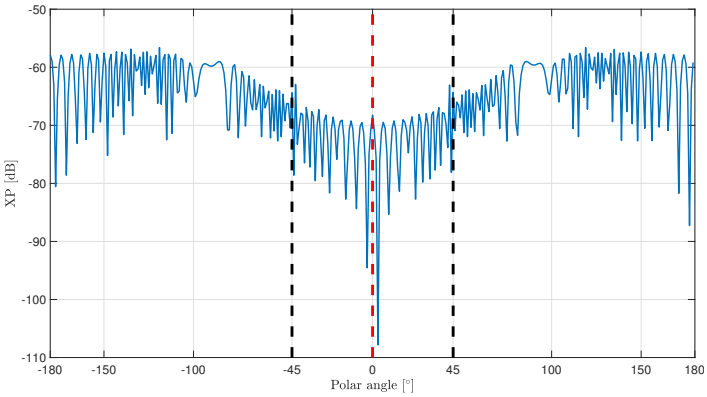

(a) $\phi_{az} = 0\,°$

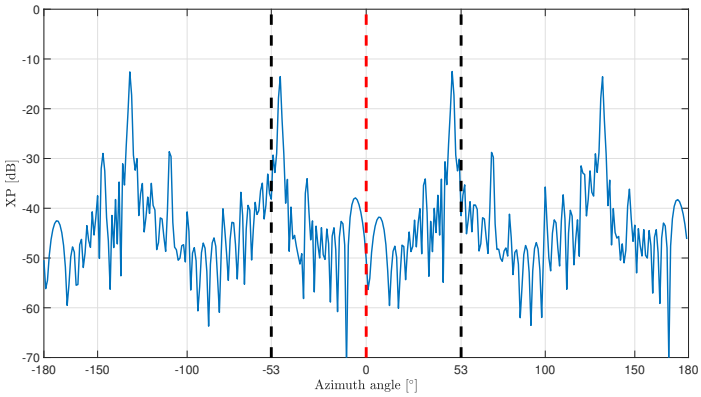

(b) $\theta_{pol} = 90\,°$

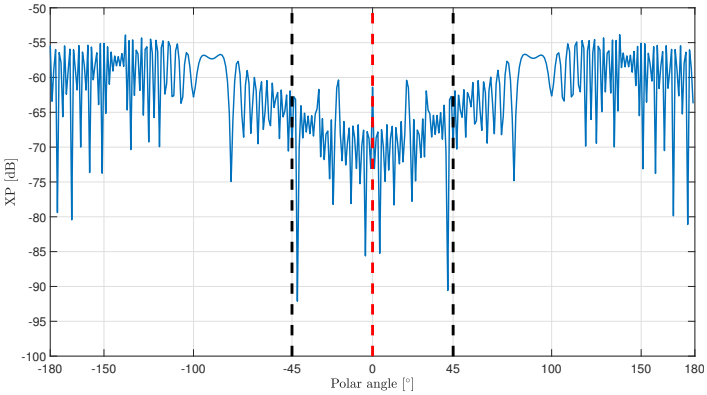

(c) $\phi_{az} = 0\,°$

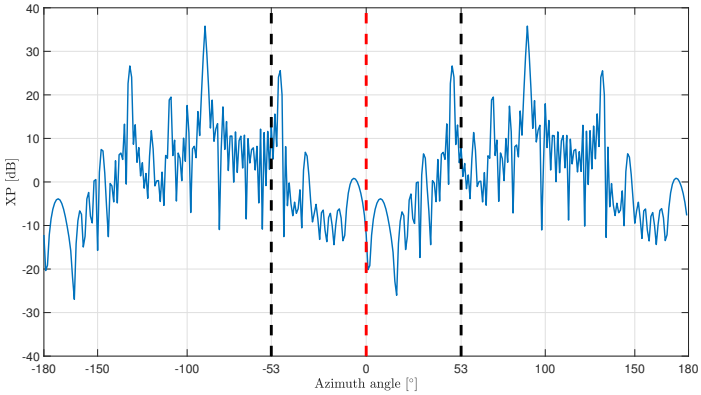

(d) $\theta_{pol} = 90\,°$

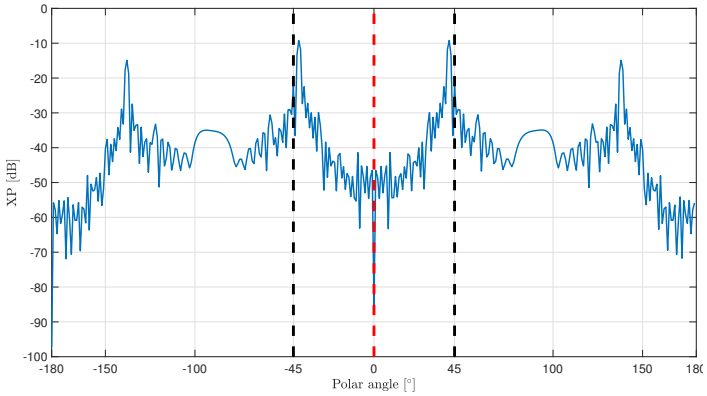

(e) $\phi_{az} = 90\,°$

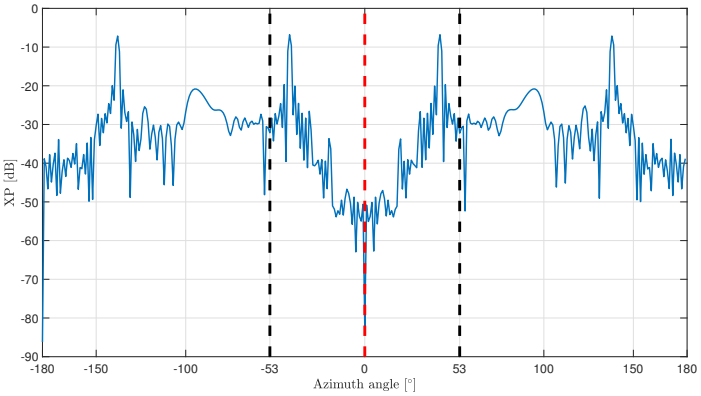

(f) $\theta_{pol} = 90\,°$

Figure 4.9: XP for the n_s-section with rounded, dumbbell and rotated slots. The $\phi_{az} = 0\,°$ and $\theta_{pol} = 90\,°$ cuts are considered for the sections with rounded (a)-(b) and dumbbell (c)-(d) slots, while the $\phi_{az} = 90\,°$ and $\theta_{pol} = 90\,°$ cut are considered for the section with rotated slots (e)-(f). The red dashed line represent the boresight direction and the black line/lines represents the angles $\phi_{az} = \pm 53\,°$ or $\theta_{pol} = \pm 45\,°$ from boresight for which the XP is studied.

5

Discussion of the Results

The preliminary study and the design of the slot arrays are discussed in two separate Sections. Furthermore, aspects of the task that were not investigated in this thesis are discussed in the Section called "Future Work". The topics that are highlighted in this Section only concerns the slot feeds and what actions that can be undertaken to enhance the bandwidth of the feeds. All focus is put on this topic, since broadband performance of the feeds was the most important design criteria. Remember that the design criteria of slot feeds were that the bandwidth simply should be as large as possible, see Section 1.1.

5.1 Discussion of the preliminary study in WSAP

The preliminary study performed in WSAP is a very flexible and time efficient way to analyze different array configurations. From simulating a single linear array with 128 elements and a spacing of $\frac{\lambda}{2}$, a very big set of thinner array configurations, i.e with fewer elements and with the same spacing or larger, could be analyzed retroactively in Matlab. In this study, a methodological mistake was made. The element spacing used in WSAP was $\frac{\lambda}{2}$ for array 1-4 and λ for array 5-7. However, the slot spacing in an array of standing wave type must be $\frac{\lambda_g}{2}$. For this reason, array 1-4 could not be considered for implementation in CST because the element spacing used for these arrays in WSAP was too short ($\frac{\lambda}{2} < \frac{\lambda_g}{2}$). Array 5-7, on the other hand, could be considered since the element spacing used for these arrays was less than $\frac{\lambda_g}{2}$. Since different spacing was used, will there be a difference between the values of the power/phase spread that is obtained with the slot array and the corresponding array in WSAP. It is not evident whether the fact that a smaller spacing was used for the 48-slot array than the corresponding array in WSAP, would result in better or worse power/phase spread than what is predicted in Table 4.1. If a distance of $\frac{\lambda_g}{2}$ were used in WSAP, would there have been a direct similarity between the arrays studied in WSAP and the array that then was implemented in CST. Therefore, the preliminary study should rather be considered as an indication of which array configuration that is needed to achieve a certain field variation in the test zone rather than a definitely answer to this. Also, given that the other simplifications made in WSAP cannot practically be satisfied (free space and that the test zone are located in exactly the same plane as the feed), the power/phase spread achieved with the slot array may nonetheless not be very accurately predicted. It may therefore not have mattered too much that a spacing $\frac{\lambda}{2}$ instead of $\frac{\lambda_g}{2}$ was used in WSAP. However, it disqualified several of the arrays from being implemented.

An explanation of why this mistake was committed is that it initially was not known for the author which antenna element that was to be considered in CST. This was specified by RanLOS a few weeks after the Thesis begun. This, and initial lack of knowledge by the author that a element spacing of $\frac{\lambda_g}{2}$ was necessary for an SWA, made so that this mistake

was discovered when there was no longer enough time to perform a new simulation.

Another part of the preliminary study in WSAP, was to analyze a couple of smaller arrays configuration consisting of 1, 24 and 36 elements. The result of this study (see Figure 4.1-4.2 and Table 4.2) is in line with what is expected, in that the FoM's, especially in the phase spread, decreases as more elements are used. This indicate in turn that a more planar LOS-component is created. In Figure 4.1 (a), the spherically radiation of the power/phase suggest that a single antenna element acts like a point-source. In the other subfigures in 4.1, it is clear that a beam take form when more elements are used. It can also be seen that two sidelobe are formed. The sidelobes are expected since the element spacing used for these arrays is λ. This spacing do not satisfy the condition in (2.40). At first glance on the power spread values in Table 4.2, it can be perceived as counterintuitive that the lowest spread is achieved with a single antenna element. However, a single antenna element will only provide a strong field at small distances from the element and over almost the entire $2\,\mathrm{m} \times 2\,\mathrm{m}$ area, the power is generally small, resulting in a small variation of the power and consequently a small power spread in the test zone. However, when more antenna elements are used, the power variation will be larger over the whole $2\,\mathrm{m} \times 2\,\mathrm{m}$ area, which also gives larger values of the power spread. Table 4.1 suggest that the power/phase spread generally decrease as more elements are considered. This trend is also suggested in Table 4.2. It can be seen how the phase varies along the diameter of the test zone for the three array configurations in Figure 4.2. The observant reader would see that the variations, which is read as the largest absolute value of the curve, are consistent with the corresponding values of the phase-spreads that are listed in Table. 4.2. The spherical variation of the phase associated with a single element can clearly be seen in Figure 4.2 (a). In Figure 4.2 (b)-(c), it can clearly be seen that the variation along the diameter decreases when more elements are used.

5.2 Discussion of the Slot Feed Design in CST

First, let us discuss the parameter values of the final optimized n_s-sections in Table 4.7 and 4.8. Both these tables indicate that a longer slot length is used for the rounded slot than the dumbbell slot, which is expected. If a rounded slot and a dumbbell slot would have the same length, the perimeter of the rounded slot would be shorter than the dumbbell slot because it has enlarged ends. For this reason, the dumbbell slot will resonate at a length that typically is shorter than the corresponding length of the rounded slot. Furthermore, if we look at Table 4.7, we can see that the smallest slot width is used for the rotated slot. Before we discuss the importance of this, let us first discuss the overall performance of the three n_s-sections and the differences between them. In table 5.1, the final designed array sections (the shorted ones) are compared with some other rectangular waveguide slot arrays that are reported in the open literature. Note that only linear slot arrays of standing wave type are considered in these references. In addition, with the exception of reference [23], only measured results are referred to in the Table.

Note that the level that the bandwidth refers to in the Table is indicated with the indices of Δf. Although the bandwidth for many of the references does not refer to the same level as used in this Thesis, the Table still gives an idea of how the performance of the arrays stands in relation to other works. It is apparent from the Table that the results obtained in this Thesis are in line with the other results. Practical slot array that can achieve significantly larger bandwidths has also been reported (1.86 GHz in [40] and 2.91 GHz in [41]). However, in these references, the arrays has specifically been designed to

Table 5.1: Comparison of the finally designed array sections (the shorted ones) with similar arrays that has been reported in the open literature.

Reference	Polarization	Bandwidth	Sidelobe level	Other remarks
This Thesis	Vertical	$\Delta f_{-10\,\mathrm{dB}} = 1.66\,\mathrm{GHz}$	$-12.3\,\mathrm{dB}$ at $f_{center} = 28\,\mathrm{GHz}$	8 rounded slots used, center-fed.
This Thesis	Vertical	$\Delta f_{-10\,\mathrm{dB}} = 1.57\,\mathrm{GHz}$	$-13.0\,\mathrm{dB}$ at $f_{center} = 28\,\mathrm{GHz}$	8 dumbbell slots used, center-fed.
[23]	Vertical	$\Delta f_{-12\,\mathrm{dB}} = 1.75\,\mathrm{GHz}$	$-13.0\,\mathrm{dB}$ at $f_{center} = 2.45\,\mathrm{GHz}$	10 rounded slots used, end-fed.
[36]	Vertical	$\Delta f_{-14\,\mathrm{dB}} = 0.94\,\mathrm{GHz}$	$-12.1\,\mathrm{dB}$ at $f_{center} = 14.3\,\mathrm{GHz}$	7 rectangular slots used, end-fed
[37]	Vertical	$\Delta f_{-12\,\mathrm{dB}} = 1.24\,\mathrm{GHz}$	$-12.7\,\mathrm{dB}$ at $f_{center} = 10\,\mathrm{GHz}$	8 rounded slots used, center-fed
This Thesis	Horizontal	$\Delta f_{-10\,\mathrm{dB}} = 0.79\,\mathrm{GHz}$	$-17.4\,\mathrm{dB}$ at $f_{center} = 28\,\mathrm{GHz}$	8 rotated narrow wall slots used, center-fed
[35]	Horizontal	$\Delta f_{-12\,\mathrm{dB}} = 0.32\,\mathrm{GHz}$	$-21.9\,\mathrm{dB}$ at $f_{center} = 9.37\,\mathrm{GHz}$	12 rotated narrow wall slots used, end-fed
[38]	Horizontal	$\Delta f_{-14\,\mathrm{dB}} = 0.66\,\mathrm{GHz}$	$-15.5\,\mathrm{dB}$ at $f_{center} = 9.5\,\mathrm{GHz}$	8 non-rotated narrow wall slots used, center-fed
[39]	Horizontal	$\Delta f_{-10\,\mathrm{dB}} = 0.38\,\mathrm{GHz}$	$-15.3\,\mathrm{dB}$ at $f_{center} = 9.4\,\mathrm{GHz}$	12 rotated narrow wall slots used, end-fed

achieve broadband performance. The results in Table 5.1 also indicate that it is expected that the slot feed with rotated slots is more narrowband than the feed with rounded slots or dumbbell slots. However, in the literature used in this Thesis, no explanation is given why the rotated slot on the narrow wall typically is more narrowband than longitudinal slots on the broad wall. Two things may explain the more narrowband performance of the rotated slot.

Consider the geometry of the rotated slot (see Figure 3.7) and compare it with the geometry of the rounded/dumbbell slots (see Figure 3.6). The narrow wall is usually so short that the slot partially must wrap-around the adjacent broad walls in order to reach the resonance length. The slightly more complicated "wrap-around" geometry used for this slot makes it harder, both in practice and in simulations, to use other slot shapes than the rectangular one. The rectangular shape of the slot as well as the "wrap-around" of the slot, makes so the overall geometry of this slot is made up of many more sharp corners than the rounded/dumbbell slots. It is a well-known phenomenon that sharp edges of an RF structure cause larger changes of the structure's characteristic impedance. This, in turn, would yield a greater impedance mismatch of the rotated slot and would so explain the more narrowband performance of the array as a whole. Alternatively, a sharp edge in an RF structure can be modeled with a capacitance in parallel with the equivalent circuit of the structure. The more narrowband performance can thus be explained as follows. More sharp corners of the slot yields an overall larger parallel capacitance of the equivalent circuit of the slot (parallel capacitances are additive). The larger capacitance of the rotated slot yields a larger Q-factor of its equivalent circuit. This will in turn yield sharper resonating performances of the slot compare to the rounded/dumbbell slots, but also narrower bandwidth (the Q-factor is inversely proportional to the bandwidth). Resonating performance means radiative characteristics of the slot, which would indicate that the radiative performances can be expected to be better for the array with rotated slot compared to the arrays with rounded/dumbbell slots. This is also suggested in Figure 4.4 (a), (b) and (c) where it can be seen that lower SLL, and so sharper main lobe, is

achieved with array with rotated slots.

The second reason for the more narrowband performance of the rotated slot, may be explained if we look at the parameter values for the different sections in Table 4.7. The Table shows that the smallest slot width is used for the rotated slot. We have in the previous paragraph established a link between a higher capacitance of a slot and more narrowband performance. Since surface current flows along the perimeter of the slot, the width of a slot can be viewed as a parallel plate capacitance, where a wider slot width simply yields a smaller capacitance of the equivalent circuit of the slot. As a result, the narrower slot width used for the rotated slot may provide more narrowband performance and better radiative characteristics according to the trade-off that we have established.

At the end of Section 2.4.4, it was noted that the dumbbell slot should provide more broadband performance than the more conventional rounded/rectangular slots. In Figure 4.4 (a) and (c), we can see that this is not the case. According to the trade-off, we expect that the rounded slot should yield better radiative performances and narrower bandwidth, but the SLL and the bandwidths of these arrays partially indicate the opposite. How can this be understood? If we look again at the parameter values in Table 4.7, then we may find an explanation for this. We can see that a slightly smaller slot width was used for the dumbbell slot. The slightly smaller width may have yield narrower bandwidth of the array and improved its radiative characteristics in accordance with what was discussed in the last paragraph in the previous Section. Consequently, if the same width were used for the two slots, we might have had results that more goes in line with what is expected.

Finally, let's discuss the results that concern the shortening of the array sections. In Figure 4.8, we can note that the shortening of the array sections has a negative impact on the bandwidths. By "negative impact" means that the bandwidth of each section became centered at a frequency higher than 28 GHz and narrowed. It seems like the shortening of the waveguide increased the frequency of the TE_{10} wave that excites the slots, which shifts the bandwidths. The question then is what causes the bandwidth of each array section to narrow? We may find a possible explanation for this if we consider that the positions of the slots in each section actually remains unchanged in relation to the shortened waveguide. The slots are placed with an offset/rotation angle, has a certain width etc. so that the bandwidth are maximized around 28 GHz. When the waveguide is shortened, will the position and the geometrical dimension of the slot not be optimal for the higher frequency of the exciting wave, which will cause greater mismatch and narrower bandwidth. In Figure 4.7, we can see that the problems associated with shortening each section can be mitigated by also shortening the slots of each section. The slots will then resonate with a higher frequency that better matches the frequency of the shortened waveguide, which partially restores the original shift. The shorter slot are then more optimally adapted to the the shortened waveguide which decreases the mismatch and increases the bandwidth. Shifting the resonance frequency of a slot by changing the length of the slot, can be understood if we remember that the resonance frequency of a dipole is determine by its length - longer lengths yields lower resonating frequencies and vice versa. Since there is an analogue between a slot and a dipole through Babinet's principle, the resonance frequency of the slot can similarly be changed via the slot length. It is clear from Figure 4.7 that the shift of the bandwidth is insignificant for the section where rotated slots are used. It can also be seen the bandwidth of this section could not so effectively be shifted back to 28 GHz as it could for the other two sections where rounded/dumbbell slots are used. What could be the reason behind this? One possible explanation can be found if we consider how the slots are excited and compare

the excitation of the rounded/dumbbell slot with the excitation of the rotated slot. The excitation of a slot is proportional to the current flow that is interrupted by the slot. The rotated slot interrupts both the normal (vertical) and tangential (horizontal) components of the surface current component $\vec{J}_y$. To achieve the horizontal polarization with an array of rotated slots on the narrow wall, each slot must be rotated alternately so that the vertical component of $\vec{J}_y$ is canceled. The part of the rotated slots that cuts into the adjacent broad walls also interrupts the $\vec{J}_z$ component. The rounded and dumbbell slots, on the other hand, interrupts the $\vec{J}_x$ component only, and these slots is therefore more purely excited than the rotated slots. The more pure excitation of the rounded/dumbbell slots could explain why the bandwidth of the corresponding arrays are more "sensitive" when the length of the waveguide is shortened. For the same reason does it also explain why the bandwidth of these sections are more “responsive” when the length of the slots are shorted. The excitation of the rotated narrow wall slot, on the other hand, is less pure, i.e. excited by $\vec{J}_y$ and $\vec{J}_z$. The bandwidth of the corresponding array may therefore be more “resilient” for frequency shifts, both when the waveguide is shortened and when the length of the slots are shortened.

5.3 Future work

The implementation of the 48-slot arrays require in practice a beamforming network that feeds each n_s-section and a component for the transition between the network and each section. The next natural step would therefore be to design and simulate the distributing network and the transitional component.

The Random-LOS test setup require the use of two orthogonal LOS-components by using two feeds with linear polarizations that are orthogonal. Since the two feeds must function over the same range of frequencies, will the effective range over which the feeds may be used be limited by the feed that is most narrowband. We have found in this thesis that the horizontally polarized feed is more narrowband. One possibility of improve the bandwidth performance of the horizontally polarized feed would be to use another type of slot on the narrow wall. We have previously seen that the dumbbell slot requires a shorter length in order to resonate at 28 GHz (see Table 4.6, 4.7 and 4.8). This mean that the entire slot possibly could fit on just the narrow wall, which means that the more narrowband "wrap-around" geometry of the slot may be avoided. However, if we look at the Table 4.8, we see that the shortest length actually already is used for the rotated slot. The ends of the dumbbell slot must be enlarged in that case, which likely yields a higher Cross-polar level. The dumbbell slot may also improve the bandwidth as it is inherently more broadband than a rectangular slot. Another advantage of using a dumbbell slot at the narrow wall instead of a rectangular slot, is that the array then may be able to withstand higher signal powers before voltage breakdown occur. Let us elaborate what is meant by this statement. In case we can avoid using the "wrap-around" geometry, we don’t have to consider the corners of the slot that is constituted by the narrow wall and the top/bottom broad wall. In addition, a dumbbell slot itself consist of fewer sharp corners than the rectangular slot as the ends of the dumbbell slot. It is well known that charges tend to accumulate on sharp edges, which would cause a voltage breakdown to occur at a lower power of the exciting TE_{10} wave than for the rounded/dumbbell slots. Another aspect that would have been interesting to investigate is if it would have been possible to use rotated slots on the broad wall (refer to slot 2 in Figure 2.22) to also yield

the horizontal polarization. In that case, the rounded/dumbbell slot may then be used. Due to the same reason, that is, avoiding the use of a "pointier" slot geometry, we may then expect to achieve more broadband performance.

6
Conclusions

An array with 48 elements and a spacing of λ can yield a power/phase spread below $1\,\mathrm{dB}/10\,^\circ$ at distances 1 m, 1.5 m and 1.8 m. We may from these results conclude that this array configuration may yield sufficiently good LOS-components.

Three different slots arrays with this configuration were designed in CST. The sidelobe level for all array sections/arrays was below the required $-9\,\mathrm{dB}$ level. We can conclude from studying the XP that the feeds are indeed able to provide orthogonal linear polarizations. Finally, it can be concluded that the vertical polarized array section/array where rounded slots were used was more broadband than the array section/array where dumbbell slots were used. Based on this result, it is recommended that the array with rounded slots are used instead of the array with dumbbell slots to provide the vertical polarization in the Random-LOS test setup.

Bibliography

[1] D. Anamina, N. Ananya, "Self-Driving Vehicles (SDVS) and GEO-Information", Geonovum and Geospatial Media and Communication, 2017. vol.1, pp.15-18

[2] M.S. Kildal, J. Kvarnstrand, J. Carlsson, A.A. Glazunov, A. Majidzadeh and P.S. Kildal, "Initial Measured OTA Throughput of 4G LTE Communication to Cars with Roof-Mounted Antennas in 2D Random-LOS", *IEICE*, pp. 1. 2015.

[3] M.S. Kildal, A.A. Glazunov, J. Carlsson J. Kvarnstrand, A. Majidzadeh and P.S. Kildal, "Measured probabilities of detection for 1- and 2 bitstreams of 2-port car-roof antenna in RIMP and Random-LOS", *10th European Conference on Antennas and Propagation, EuCAP 2016*, pp. 1. 2016.

[4] A. Razavi, A.A. Glazunov, P.S. Kildal, R. Maaskant , "Array-fed cylindrical reflector antenna for automotive OTA tests in Random Line-Of-Sight", pp. 1-2. 2016.

[5] P.S. Kildal, A.A. Glazunov, J. Carlsson, A. Majidzadeh, "Cost-effective measurement setups for testing wireless communication to vehicles in reverberation chambers and anechoic chambers", *IEEE Conference on Antenna Measurements and Applications, CAMA 2014*, pp. 1-3. 2014.

[6] P.S. Kildal and J. Carlsson, "New Approach to OTA Testing: RIMP and pure-LOS as Extreme Environments & a Hypothesis". *7th European Conference on Antenna and Propagation, EuCAP 2013*, Gothenburg, Sweden, 8-12 April 2013

[7] P.S. Kildal, X. Chen, M. Gustafsson and S. Zhengzhao, "MIMO characterization on system level of 5G microbase stations subject to randomness in LOS", *IEEE Access*, vol.2, pp. 1066-5. 2014.

[8] C. Parini, S. Gregsson, and J. McCormic, *Theory and Practice of Modern Antenna Range Measurements*, 3rd ed. London: The Institution of Engineering and Technology, 2014, pp. 93-96.

[9] J.Hirokawa and M.Zhang, "Waveguide Slot Array Antenna" in *Handbook of Antenna Technologies*. Singapoure: Springer, 2016, pp. 551-552, 1391-1403, 2030-2039.

[10] P.S. Kildal, "Preparing for GBit/s coverage in 5G: Massive MIMO, PMC packaging by gap waveguides, OTA testing in random-LOS", *Loughborough Antennas and Propagation Conference, LAPC 2015*, pp. 3-4. 2015.

[11] D.M. Pozar, *Microwave And RF Design of Wireless Systems*. Hoboken: Whiley, 2001, pp. 138-139,144-146.

[12] P.S. Kildal, *Foundations of Antenna Engineering: A Unified Approach for Line-of-Sight and Multipath*, 2nd ed. Gothenburg: Kildal Antenn AB, 2015, pp. 22-37, 40-42, 65-67,75-78,100-106,193-201, 333-344.

[13] M.S. Kildal, "Evaluation of the Random-LOS Measurement System for Vehicular Communication Applications", Lic. thesis, Dept. of Electrical Engineering, Chalmers University of Technology, 2017, pp. 5-7, 10-14, 19-23, 49-53, 56-62.

[14] A. Razavi, "Characterization and Design Requirements for Antennas in the Near-field and the Random-LOS Propagation Environment", PhD thesis, Dept. of Electrical Engineering, Chalmers University of Technology, 2016, pp. 2-3, 19-24.

[15] A.A. Glazunov, P.S. Kildal, M.S. Kildal, "Devising a Horizontal Chamber Array for Automotive OTA Tests in Random Line-Of-Sight", *IEICE*, pp. 1-4. 2015.

[16] A.A. Glazunov, A. Razavi and P.S. Kildal, "Simulations of a planar array arrangement for automotive Random-LOS OTA testing", *10th European Conference on Antennas and Propagation, EuCAP 2016*, pp. 1-3. 2016.

[17] M.S. Kildal, A.A. Glazunov, J. Carlsson, A. Majidzadeh, "Evaluation of a simplified Random-LOS measurement setup for characterizing antennas on cars", *11th European Conference on Antennas and Propagation, EUCAP 2017*, pp. 3008-3009. 2017.

[18] M.S. Kildal, J. Carlsson, A.A. Glazunov, "Measurements and Simulations for Validation of the Random-LOS Measurement Accuracy for Vehicular Applications",*IEEE Transactions and Antennas Propagation*, 2017, pp. 1-12.

[19] M.S. Kildal, J. Carlsson, A. Majidzadeh, "Evaluation of a Simplified Random-LOS Measurement Setup for Characterizing Antennas on Cars",*11th European Conference on Antennas and Propagation, EuCAP* , 2017, pp. 1-7.

[20] M.S. Kildal, J. Kvarnstrand, A.A. Glazunov, "",*International Symposium on Antennas and Propagation*, 2015, pp. 1-6.

[21] D. Fleisch, *A Student's Guide to Maxwell's Equations*. New York: Cambridge University Press, 2008, pp. 1-57.

[22] D.M. Pozar, *Microwave Engineering*, 4th ed. Hoboken: Whiley, 1998, pp. 6-8, 10-18, 96-102, 110-114.

[23] S. Stančulović, "Theoretical Synthesis and Experimental Measurements of Slotted Waveguide Feeding Systems For 2.45 GHz Industrial Microwave Heating Installations", PhD thesis, Faculty of Electronic and Information Technology, Karlsruhe Institute of Technology, 2006, pp. 5-18, 36-39, 52-58.

[24] dos Santos, Guliherme.B, Akamine, Cristianos, dos Santos , Edson T.C. *Dual-Polarized Indoors Antenna for Digital TV Reception*. SET INTERNATIONAL JOURNAL OF BROADCAST ENGINEERING, 2017. vol.3, pp. 45-51.

[25] P.S. Kildal, K.Rosengren, "Study of the Distribution of Modes and Plane Waves in Reverberation chamber for the Characterization of Antennas in a Multipath Environment", *Microwave and Optical Technology Letters*, vol.30, no.6, pp.386-388. Sep, 2001.

[26] R.C. Johnson, H.A. Ecker and R.A. Moore, "Compact Range Techniques and Measurements", *IEEE Transactions of Antennas and Propagation*, vol.5, pp. 568-576. 1969.

[27] T.A. Milligan, "DIPOLES, SLOTS, AND LOOPS" in *Modern Antenna Design*, 2nd ed. Whiley, 2005, pp. 218-219.

[28] T.A. Milligan, "Waveguide Slot Antenna Array" in *Antenna Engineering Handbook*, 4th ed. McGraw-Hill, 2007, pp. 1-14.

[29] A.J.N. Maritz, "Investigation and Design of a Slotted Waveguide Antenna with Low 3D Sidelobes", M.A. thesis, Dept. of Electrical and Electronic Engineering, Stellenbosh Univeristy, 2010, pp. 6-13, 15-18.

[30] J.W. Mcknight, "A cavity-backed coplanar waveguide slot antenna array", M.T. thesis, Univeristy of South Carlifornia, 2009, pp. 2-3, 19-24.

[31] P.S, Kildal and J.Yang, "Microwave Antennas Laboratory Exercise 2: Measurement of waveguide slot admittance". Gothenburg: Department of Electromagnetics, Chalmers University of Technology, 2004, pp. 2-11.

[32] S. Rozenberg and A. Yaholm, "A THz Slot Antenna Optimization Using Analyticaly Techniques", *Radio Engineering*, vol.25,No. 1, pp. 1-7. 2016.

[33] M. Grabowski, "Non-Resonant Slotted Waveguide Antenna Design Method: Inclusive Internal and External Electromagnetic Coupling Between Slots", *High Frequency Electronics*, pp. 35-38. 2012.

[34] H.M.El. Misilmani, A.H. Mohammed and K.Y. Kabalan, "Design of Slotted Waveguide Antennas with Low Sidelobes for High Power Microwave Applications", *IEEE Transactions of Antennas and Propagation*, vol.56, pp. 15-18. 2015.

[35] K.E. Rodrigo and BP. Marcelo, "Slotted Waveguide Antenna Design Using 3D EM Simulation", *Microwave Journal*, pp. 1-5. 2013.

[36] Hamadallah, Mazen, "Frequency Limitations on Broad-Band Performance of Shunt Slot Arrays", *IEEE TRANSACTIONS ON ANTENNAS AND PROPAGATION*, vol.31, no.7, pp.817-823. Jul, 1989.

[37] Wang, Wei and Zhong, Shun Shi and Zhang, Yu Mei and Liang, Xian Ling, "A broadband slotted ridge waveguide antenna array", *IEEE Transactions on Antennas and Propagation*, vol.54, no.8, pp.2416-2420. Aug, 2006.

[38] Liu, A. Q. and Palei, W. and Tang, M. and Alphones, A., "AN UNTILTED EDGE-SLOTTED WAVEGUIDE ANTENNA ARRAY WITH VERY LOW CROSS-POLARIZATION", *Microwave and Optical Technology Letters*, vol.44, no.1, pp.91-93. Jun, 2005.

[39] Lubis, Amanta K.S. and Apriono, C. and Zulkifli, Fitri Y. and Rahardjo, Eko T., "Design of narrow wall slotted waveguide antenna for X-band application", *Progress in Electromagnetics Research Symposium, Singapore*, pp. 2625-2628. 2017.

[40] Zhao, H C and Xu, R R and Wu, W, "Broadband waveguide slot array for SAR", *Electronic Letters*, vol.47, no.6, pp.1-2. Jan, 2011.

[41] Jha, Hare Ram and Singh, Shiva Nand, "Design and Analysis of Waveguide-Fed Broad-Wall Longitudinal Log Periodic Slotted Array Antenna for 8.2 ˜ 11.11 GHz Frequency Applications", *Microwave and Optical Technology Letters*, vol.1, no.6, pp.15-23. Nov, 2014.

A

Appendix: WSAP

A.1 Matlab Files Used for the Simulation in WSAP

In this Section are the Matlab files that was used to perform the analysis in WSAP shown. The files are presented in chronological order, which means that they are presented in the order they were used during the analysis. File 1 was used before the simulation in WSAP, while the other files were used to process the results from the simulation. Each file are continuously commented.

File 1: `MakeInc.m`

```
% This file creates a .txt file with instructions that was loaded
% into WSAP in order to control how the dipole was sweeped.

% The file was created by Madeleine Schilliger Kildal
% Industrial PhD student, Antenna Systems Group
% Department of Electrical Engineering
% Chalmers University of Technology. Used with permission.

clearvars
clc

nx = 201; % Steps in x corresponding to 1 m (402 for 2 m) when a dipole spacing of 5 mm is used.
dy = 0.005; % Dipole spacing
ny = 201; % Steps in y corresponding to 1 m (402 for 2 m) when a dipole spacing of 5 mm is used.
dx = -dy; % To increment x in negative direction (see Fig.3.1)

inc = [0 dy 0]; % Single instruction corresponding to moving the dipole one position in y
inc_mat_y = repmat(inc,nx-2,1); % Repeated set of instructions (corresponds to moving
                                % the dipole along a line in y that is 1 m long)
inc_mat_x = [dx 0 0];           % Single instruction corresponding to move the dipole
                                % one dipole spacing down in x


inc_mat_part = [inc_mat_y; inc_mat_x; -inc_mat_y; inc_mat_x]; % Concatenate a set of instructions
                                    % (move 1 m in y, move down one space in x etc., see Fig.3.3)
inc_mat_all = repmat(inc_mat_part, (ny-2)/2,1); % Repeat instructions (ny-2)/2 times
inc_mat_all = [inc_mat_all; inc_mat_y]; % Concatenate the first set of instructions with the
                        % the same set of instructions that has been repeated (ny-2)/2 times to
                        % yield the final set of instructions corresponding to sweeping the dipole
                        % over an 1 m × 1 m or 2 m × 2 m area

inc_mat = inc_mat_all;

% Write the instructions to a .txt file
dlmwrite('WsapIncPlane2mx2m5mmGrid_WSAP2103_v5.txt',inc_mat,'delimiter',' ','newline', 'pc')
```

File 2: `Read_files_WSAP.m`

```
% This file reads some of the files obtained during the simulation in WSAP,
% processes these WSAP-files and store the results in a Matlab file.
% The Matlab file was then processed using file 3-7


% The file was created by Madeleine Schilliger Kildal
% Industrial PhD student, Antenna Systems Group
% Department of Electrical Engineering
% Chalmers University of Technology. Used with permission.

clearvars
clc

filepath = 'file/path/to/the/WSAP/files'; % To open the nearfield.data WSAP-file
filename = 'filename.nearfield.dat';
find_extension = find(filename == '.'); % To automatically name the Matlab
                                        % file with the same name as the WSAP files
original_filename = filename(1:find_extension(1)-1);
savename = [original_filename '.mat'];

sweeppath = 'file/path/to/the/sweep/file'; % To open the sweep file
sweep_filename = 'sweep_file.txt';
data = [];
data_temp = [];
fileinfo = [];

% Read the nearfield.dat file. The file header must first be removed to be able to read the file
fid = fopen([filepath '\' filename]);               % Open the nearfield.dat file.
first_line = fgetl(fid);                            % Read/discard file header.
if first_line == 'x y z ExRe ExIm EyRe EyIm EzRe EzIm HxRe HxIm HyRe HyIm HzRe HzIm' % File header
    buffer = fread(fid, Inf);                       % Read rest of the file.
    fid2 = fopen([filepath '\' 'tr' filename], 'w');% Open destination file.
    fwrite(fid2, buffer) ;                          % Save to destination file.
    fclose(fid2) ;
    filename = ['tr' filename];
end
fclose(fid);

% Read the naerfield.dat file. Determine the number of dipole positions
% for the entire simulation and the number of sampling points
n_dp_pos = length(find(M(:,2) == [-1])); % Dipole positions
n_nearfield = size(M,1)/n_dp_pos;       % Sample points
M_cell = mat2cell(M, [n_nearfield*ones(1,n_dp_pos)], [15]);
for pos = 1:n_dp_pos
    M_mat_part = cell2mat(M_cell(pos));
    M_mat_part = M_mat_part(2:end,:);
    data(:,:,pos) = M_mat_part;
end
n_nearfield = n_nearfield - 1;

% Translate the sweep coordinates (relative coordinates) of the dipole positions
% to global coordinates corresponding to the coordinate system in WSAP.
% This is done by using the sweep file.
sweep = dlmread([sweeppath '\' sweep_filename]); % Read the sweep file

% Read the .geo WSAP-file
filename2 = [original_filename '.geo'];
geo_info = 'x1, y1, z1, x2, y2, z2, n_basefunctions, thickness, name';
fid2 = fopen([filepath '\' filename2]);
geo_cell = textscan(fid2,'%f32 %f32 %f32 %f32 %f32 %f32 %f32 %f32 %s');
fclose(fid2);

% Determine the starting coordinates of the dipole from the .geo WSAP-file
positions = cell2mat(geo_cell(1:8));
x_start = (positions(2,1) + positions(2,4))/2;
y_start = (positions(2,2) + positions(2,5))/2;
z_start = (positions(2,3) + positions(2,6))/2;
pos_start = [x_start y_start z_start];
dp_pos_all = [pos_start; zeros(size(sweep,1),3)];
```

```
70
71 for ii = 1:size(sweep,1)
72     dp_pos_all(ii+1,:) = dp_pos_all(ii,:) + sweep(ii,:); % Translate to global coordinates
73 end
74
75 % Determine the number of dipole positions in x,y and z
76 % for the dipole positions that now is expressed with global coordinates
77 n_dp_x = length(unique(round(dp_pos_all(:,1)*1000)));
78 n_dp_y = length(unique(round(dp_pos_all(:,2)*1000)));
79 n_dp_z = length(unique(round(dp_pos_all(:,3)*1000)));
80
81
82 % Check that the correct sweep file is used:
83 if n_dp_pos ≠ n_dp_x*n_dp_y*n_dp_z
84     fprintf('Warning: Not the correct sweep file is used!!!\n')
85     return
86 end
87
88 % Remove variables that should not be saved in the Matlab file
89 clearvars ans data_temp fid freqInd num_ang radInd space tline val find_extension ...
90     fid2 filename2 ii original_filename positions x_start y_start z_start pos_start ...
91     buffer first_line M M_cell M_mat_part pos sweep
92
93 save(savename, '-v7.3') % Save the data to an Matlab file
```

File 3: `Left_side.m`

```
% This file concatenate the near-field data (i.e the E_z-components) and the corresponding
% dipole positions from area 1 and 3 (see Fig.3.3) and remove data corresponding to the
% common sweep line (i.e the first sweep line in area 3 which is the same sweep line
% as the last line in area 1)

clearvars
clc

savename = 'left_side_concatenation_area_1_and_3.mat';

f1 = load('matlab_construct_file_area_1.mat'); % Load data corresponding to area 1
f3 = load('matlab_construct_file_area_3.mat'); % Load data corresponding to area 3


% Concatenate near-field data corresponding to area 1 and 3 vertically
data = cat(3, f1.data, f3.data);
data(:,:,40402:40602) = []; % Remove near-field data corresponding to the
                            % common sweep line (i.e. last line in area 1)


dp_pos_1 = f1.dp_pos_all; % Extract the dipole positions corresponding to area 1
dp_pos_3 = f3.dp_pos_all; % Extract the dipole positions corresponding to area 3

% Remove dipole positions corresponding to the common sweep line (i.e. last line in area 1)
dp_pos_3(1:201,:,:)= [];
dp_pos_left = vertcat(dp_pos_1, dp_pos_3);% Concatenate the dipole positions
                                          % corresponding to area 1 and 3 vertically

clearvars f1 f3  dp_pos_1 dp_pos_3

save(savename)
```

File 4: `Right_side.m`

```
% This file concatenate the near-field data (i.e the E_z-components) and the corresponding
% dipole positions from area 2 and 4 (see Fig.3.3) and remove data corresponding to the
% common sweep line (i.e the first sweep line in area 4 which is the same sweep line
% as the last line in area 2)

clearvars
clc

savename = 'right_side_concatenation_area_2_and_4.mat';

f2 = load('matlab_construct_file_area_2.mat');  % Load data corresponding to area 2
f4 = load('matlab_construct_file_area_4.mat');  % Load data corresponding to area 4

% Concatenate near-field data corresponding to area 2 and 4 vertically
data = cat(3, f2.data, f4.data);
data(:,:,40402:40602) = []; % % Remove near-field data corresponding to the
                            % common sweep line (i.e. last line in area 2)

dp_pos_2 = f2.dp_pos_all; % Extract the dipole positions corresponding to area 2
dp_pos_4 = f4.dp_pos_all; % Extract the dipole positions corresponding to area 4

% Remove dipole positions corresponding to the common sweep line
dp_pos_4(1:201,:,:)= [];
dp_pos_right = vertcat(dp_pos_2, dp_pos_4); % Concatenate the dipole positions
                                            % corresponding to area 2 and 4 vertically

clearvars f2 f4 dp_pos_part2 dp_pos_4

save(savename)
```

File 5: `Add_side.m`

```
% This file concatenate the near-field data and the corresponding
% dipole positions from the left- and right side of the 2 m × 2 m area
% and removes the data along the row that is common for both sides (see Fig.3.3).
% The common row is located at the origo corresponding to the coordinate system in WSAP.

% This file was created by Madeleine Schilliger Kildal
% Industrial PhD student, Antenna Systems Group
% Department of Electrical Engineering
% Chalmers University of Technology. Used with permission.

clearvars
clc

savename = 'full_2mx2m_area_no_binary_mask_applied_yet.mat';

f1 = load('left_side_concatenation_area_1_and_3.mat'); % Data corresponding to the
                                                       % left side (area 1 and 3)
f2 = load('right_side_concatenation_area_2_and_4.mat'); % Data corresponding to the
                                                        % right side (area 2 and 4)

zero_ind = find(abs(f1.dp_pos_left) < 1e-5); % Find dipole positions corresponding
                                             % to the common row at origo
dp_pos_1 = f1.dp_pos_left; % Dipole positions corresponding to area 1 and 3
dp_pos_1(zero_ind) = 0;
zero_ind = find(abs(f2.dp_pos_right) < 1e-5); % Find dipole positions corresponding
                                              % to the common row at origo
dp_pos_2 = f2.dp_pos_right; % Dipole positions corresponding to area 2 and 4
dp_pos_2(zero_ind) = 0;
same_pos = ismember(dp_pos_1,dp_pos_2, 'rows'); % Identify the duplicated dipole positions
                                                % along the common row

dp_pos_all = cat(1, dp_pos_1(¬same_pos,:), dp_pos_2); % Remove dipole positions corresponding
                                                      % to the common row between area 1-2 and 3-4


Data = cat( 3, f1.data(:,:,¬same_pos), f2.data); % Remove near-field data corresponding
                                                 % to the common row between area 1-2 and 3-4

clearvars f1 f2 zero_ind dp_pos_1 dp_pos_2 same_pos
save(savename, '-v7.3')
```

File 6: `Apply_the_binary_mask.m`

```
% This file allow the user to chose which near-field data from the sample points to
% include/exclude from the processing (i.e calculation of FoM's) that is performed with
% file 7. The file plots 128 circles with equal radius that each corresponded
% to one of the sample points in WSAP. The Axis of the figure where the circles is plotted has
% no correspondence to the actual sample point spacing that was used in the WSAP. The clicking
% functionality is realized by the built-in ginput function in Matlab. The distance between each
% clicked point recorded with ginput and the center of each circle is calculated iteratively.
% If the distance is larger (smaller) then the radius of the circle is a value of 0 (1) assigned
% to the filter variable, v. This variable is then multiplied by the variable, Ez, which
% stores the near-field data from all dipole positions in the 2m x 2m area. Since the total field
% at each grid point is given by superposition of the sample points, will all
% sample points that is multiplied with zero not contribute to the field in the area.

% HOW THE FILE SHOULD BE USED:
% The plotted circles MUST be filled out from right to left if 1 x N sample points was used.
% All points must be filled out AND in the this order for the code to work. If a sample point
% should be included, click anywhere INSIDE the corresponding circles, otherwise click anywhere
% outside the circle. Clicking on the rim of a circle will generally lead to an inclusion
% of the point but may potentially lead to an exclusion, so avoid this behaviour.


close all
clearvars
clc; clf;

load('full_2mx2m_area_no_binary_mask_applied_yet.mat')
savename = 'full_2mx2m_area_applied_binary_mask.mat';

Ez = squeeze(Data(:,8,:)+1i*Data(:,9,:)); % Extract the Ez-components


sample_length = 128; % Number of sample points along the y-direction in WSAP
sample_height = 1;   % Number of sample points in the positive z-direction in WSAP
                     % (used for planar arrays with M x N elements).
                     % This variable is set to 1 for linear arrays

% Check that the correct number of sampling points is used.
% The filter should ONLY be applied to an linear array with 128 elements
if 128 ≠ sample_length*sample_height
    fprintf('Warning: the number of sample points is larger/smaller than 128')
    return
end

ii = 1:sample_length;
jj = 1:sample_height;
[x,y] = meshgrid(ii,jj);

a = sort(reshape(x,[sample_length*sample_height,1])); % Center points of the circles
b = repmat(y(:,1),[sample_length,1]);

centers = horzcat(-a,b);
radii = (1:length(centers))';

for i = 1:length(centers)
   radii(i) = 0.3; % Set the radius of the circles
end

figure(1)

for i = 1:sample_height*sample_length
viscircles(centers(i,:),radii(i)); % Plot the circles corresponding to the sample points
end

sample_length_lim = 50; % Use different axis if more than 50
                        % sample points was used in the simulation (for better visibility)


if sample_length ≥ sample_length_lim
    set(gca,'XLim',[-max(max(x))-1 -min(min(x))+1], 'YLim',[min(min(y))-10 max(max(y))+10]);
```

```
else
    set(gca,'XLim',[-max(max(x))-1 -min(min(x))+1], 'YLim',[min(min(y))-1 max(max(y))+1]);
end

daspect([1 1 1])

hold all

xx = zeros(length(Ez),1);
yy = zeros(length(Ez),1);

counter = 1:1:sample_length*sample_height; % Set counter to keep track of the number of clicks
% First loop activates if more than 50 sample points was used
if sample_length ≥ sample_length_lim % This file should be apply to 128 element array,
    for i=1:sample_length*sample_height % so this loop should always activate

        zoom on; % Allow the user to zoom in/out and drag with the mouse between each click
        pause()  % A pause for an indefinite long time between each click. Pause is inactivated
                 % by the user pressing any key or click with the mouse

        % Record/store each clicked position
        [x_gin,y_gin] = ginput(1);
        xx(i) = abs(x_gin);
        yy(i) = y_gin;

        scatter(x_gin(:),y_gin(:),'r', 'filled') % Plot each clicked position so that
                                                 % the user can see were he/she has clicked

        % Update and display counter so that the user can keep track of the number of clicks
        str = ['#', num2str(counter(i)),'/' num2str(sample_length*sample_height)];
        title(str)
        xlabel('$\bf \leftarrow y$', 'interpreter', 'latex');
        ylabel('$\bf  z\rightarrow$', 'interpreter', 'latex');
        xLimits = get(gca,'XLim');
        yLimits = get(gca,'YLim');
    end
else
    for i = 1:sample_length*sample_height % Second loop activates if less
                                          % than 50 sample points was used
        [x_gin,y_gin] = ginput(1);
        xx(i) = abs(x_gin);
        yy(i) = y_gin;

        scatter(x_gin(:),y_gin(:),'r', 'filled')

        str=['#', num2str(counter(i)),'/' num2str(sample_length*sample_height)];
        title(str)
        xlabel('$\bf \leftarrow y$', 'interpreter', 'latex');
        ylabel('$\bf  z\rightarrow$', 'interpreter', 'latex');
        xLimits = get(gca,'XLim');
        yLimits = get(gca,'YLim');
    end
end

hold off
close all

r = zeros(1,128);

% Calculate the distance from the center of the circles to the recorded clicked positions
for i = 1:numel(x)
   r(i) = sqrt((xx(i)-a(i))^2+(yy(i)-b(i))^2 );
end

tol = max(radii); % Limit to determine whether the users clicking will lead to an
                  % inclusion/exclusion of the corresponding sample point
                  % The limit is set to the radius of the circles.

v = zeros(size(Ez)); % Initialize filter variable

```

```
% Create the filter variable v. If the distance r(i) corresponding to a certain sample point
% is greater than the circle radius, will v = 0 (excluded point). Otherwise v = 1 (included point).
for i = 1:sample_length*sample_height
    if r(i) < tol
        v(i,:,1) = 1;
    end
end

Ez_masked = Ez.*v; % Apply the filter on the near-field data

clearvars ans Data sample_length sample_length_lim sample_height ii jj x y a b ...
          centers radii xx yy counter x_gin y_gin xLimits yLimits str r tol

save(savename)
```

File 7: Calculate_the_FoM.m

```
% This file plot the power-and phase of the near-field data over the 2 m × 2 m area
% and calculate the FoM's (i.e. power-and phase spreads) in the 30 cm test-zone. The center of
% the test-zone is located in the xy-plane at x = D m and y = 0 m (see Fig.3.3) from the sample points.

close all
clearvars
clc; clf

load('full_2mx2m_area_applied_binary_mask.mat')

%%%%%%%%%%%%%%%%%%%%%%%%%%%%%%%%%%%%%%%%%%%%%%%%%%%%%%%%%%%%%%%%%%%%%%%%%%%%
%                              Plot power                                    %
%%%%%%%%%%%%%%%%%%%%%%%%%%%%%%%%%%%%%%%%%%%%%%%%%%%%%%%%%%%%%%%%%%%%%%%%%%%%

% Calculate power of the near-field data for each dipole position,
% i.e. P = sum_{i=1}^{N} |E_z|^2, where the summation is taken over N sample points.
% First is values of P that are unusually large handled.
% Large values arise when the dipole was very close to
% the sample points in the simulations (i.e. at dipole positions
% along the first sweep line close to origo). This condition yields
% large E_z-values (r very small and E_z ∝ 1/r).
% The power values are normalized. The plot will therefore
% look weird if these values are not averaged out

Ez_masked = squeeze(Data(:,8,:)+1i*Data(:,9,:)); % Extract the E_z-components

power_sample = abs(Ez_masked)^2;          % Line of code used for array with
                                          % single sample-point (i.e N = 1)
power_sample = abs(sum(Ez_masked,1)).^2;  % Line of code used for array with
                                          % multiple sample-point
threshold=1e7;  % The threshold value was empirically chosen

% If P-value at a certain dipole position is larger than threshold, average the value out.
for i = 1:length(power_sample)
    if power_sample(i) > threshold
      power_sample(i) = ( power_sample(i-1)+power_sample(i-2) )/2;
    end
end

power_mean = mean(power_sample); % Calculate the mean of all P-values in the area
power_norm = 10*log10(power_sample/power_mean); % Normalized the P-values

% Create matrix (used for plotting the power and phase)
pos_x = double(dp_pos_all(:,1));
pos_y = double(dp_pos_all(:,2));
% Spacing (i.e 0.001) is arbitrary, but should be small for better accuracy of the calculated FoM's
pos_x_grid = double(min(dp_pos_all(:,1)):0.001:max(dp_pos_all(:,1)));
pos_y_grid = double(min(dp_pos_all(:,2)):0.001:max(dp_pos_all(:,2)));
[X,Y] = meshgrid(pos_x_grid,pos_y_grid);

% Plot power
Z_power = griddata(pos_x,pos_y,power_norm,X,Y);
figure(2)
colormap jet
surf(-X,Y,Z_power,'linestyle','none'); % -X to "flip" the plot in x
view(2);
name_of_figure = 'WSAP: f=28GHz, 2mx2m sweep, 1x48 sample point, spacing = $\lambda$';
title(name_of_figure,'Interpreter', 'latex')
xlabel('$\bf x,\ [m]$', 'interpreter', 'latex');
ylabel('$\bf y,\ [m]$', 'interpreter', 'latex');
h = colorbar;
ylabel(h, '$P_{norm},\ [dB]$','interpreter', 'latex')

% Draw the circular test zone
hold on;
center = horzcat(1,0); % Center point of test-zone. D = 1.0 m considered in this case
radius = 0.15; % Radius of test-zone in m
```

```
viscircles(center,radius); % Plot test-zone
daspect([1 1 1])
hold off

%%%%%%%%%%%%%%%%%%%%%%%%%%%%%%%%%%%%%%%%%%%%%%%%%%%%%%%%%%%%%%%%%%%%%%%%
%                          Plot phase                                    %
%%%%%%%%%%%%%%%%%%%%%%%%%%%%%%%%%%%%%%%%%%%%%%%%%%%%%%%%%%%%%%%%%%%%%%%%

% Calculate phase of the near-field data for each dipole position, i.e. ϕ = sum_{i=1}^{N} arg(E_z)
phase_sample = angle(Ez_masked);        % Line of code used for array with
                                        % one sample points (N = 1)
phase_sample = angle(sum(Ez_masked,1)); % Line of code used for array with
                                        % multiple sample points
phase_sample = rad2deg(phase_sample);   % Convert from radiance to degrees
phase_sample = unwrap(phase_sample);    % Unwrap phase

% Plot phase
Z_phase = griddata(pos_x,pos_y,phase_sample,X,Y);
figure(3)
surf(-X,Y,Z_phase,'linestyle','none'); % -X to "flip" the plot in x
colormap hsv
view(2);
name_of_figure = 'WSAP: f=28GHz, 2mx2m sweep, 1x48 sample point, spacing = $\lambda$';
title(name_of_figure,'Interpreter','latex')
xlabel('$\bf x,¬[m]$', 'interpreter', 'latex');
ylabel('$\bf y,¬[m]$', 'interpreter', 'latex');
h = colorbar;
ylabel(h, '$\phi,¬¬[^{\circ}]$','interpreter', 'latex')

daspect([1 1 1])

%%%%%%%%%%%%%%%%%%%%%%%%%%%%%%%%%%%%%%%%%%%%%%%%%%%%%%%%%%%%%%%%%%%%%%%%
%  Extract P-values within the test-zone       %
%%%%%%%%%%%%%%%%%%%%%%%%%%%%%%%%%%%%%%%%%%%%%%%%%%%%%%%%%%%%%%%%%%%%%%%%

% Extraction is performed by creating an circular mask, where the
% size and position of the mask corresponds to the test-zone
 z = griddata(pos_x,pos_y,power_sample,X,Y);
[rows, columns] = size(z);

% Initialize parameters for the circular mask
circleCenterY = (1.0/2.0)*length(z); % Column of z where the center of the test-zone is located,
                                     % D = 1.0 m considered in this case
circleCenterX =  1000;               % Row of z where the center of the test-zone is located
                                     % circleCenterX= length of z / 2
                                     % length of z varies according to x_pos and y_pos above

circleRadius = 150;     % Radius of the test-zone in terms of number of vector element of z
                        % Derivation of circleRadius for 2 m × 2 m area:
                        % Length of one vector element in z, step = 2 m / (0.5 × length of z).
                        % Radius (R) of test-zone, R = 0.15 m,
                        % CircleRadius= R / step = 150

% Initialize the circular mask
circleImage = false(rows,columns);
[XX, YY] = meshgrid(1:columns, 1:rows);
circleImage((XX - circleCenterX).^2 + (YY - circleCenterY).^2 ≤ circleRadius.^2) = true;

% Mask the data
maskedImage = z;
maskedImage(¬circleImage) = 0; % Filter out the P-values outside the test-zone

% Extract values from the masked region
[¬,¬,values] = find(maskedImage);
```

```
136
137 %%%%%%%%%%%%%%%%%%%%%%%%%%%%%%%%%%%%%%%%%%%%%%%%%%%%%%%%%%%%%%%%%%%%%%%
138 % Extract ϕ-values located along the diameter line     %
139 %%%%%%%%%%%%%%%%%%%%%%%%%%%%%%%%%%%%%%%%%%%%%%%%%%%%%%%%%%%%%%%%%%%%%%%
140
141
142 % In order to correctly extract the ϕ-values along the the diameter line must an matrix
143 % first be created. The matrix should correspond to the 2 m × 2 m area that was simulated.
144
145 Ez_summed = squeeze(Data(:,8,:)+1i*Data(:,9,:)); % Line of code used for array
146                                                   % with one sample point (N = 1)
147 Ez_summed = sum(Ez_masked).';                     % Line of code used for array
148                                                   % with multiple sample point
149
150 Ez1 = Ez_summed(1:40200,1); % Extract values from area 1
151 Ez3 = Ez_summed(40201:80200,1); % Extract values from area 3
152 Ez1 = reshape(Ez1,[200,201]).'; % Reshape area 1 to 1 m × 1 m area
153 Ez3 = reshape(Ez3,[200,200]).'; % Reshape area 3 to 1 m × 1 m area
154
155 Ez_left = vertcat(Ez1, Ez3); % Concatenate area 1 and 3
156
157 Ez2 = Ez_summed(80201:120601,1); % Extract values from area 2
158 Ez4 = Ez_summed(120602:160801,1); % Extract values from area 4
159 Ez2 = reshape(Ez2,[201,201]).'; % Reshape area 2 to 1 m × 1 m area
160 Ez4 = reshape(Ez4,[201,200]).'; % Reshape area 4 to 1 m × 1 m area
161
162 Ez_right = vertcat(Ez2, Ez4); % Concatenate area 2 and 4
163 Ez_tot = horzcat(Ez_left, Ez_right); % Concatenate both sides to yield matrix containing
164                                      % Ez-components corresponding to the 2 m × 2 m area
165
166 % Find the center-position of the test-zone in the matrix corresponding to the 2 m × 2 m area
167 step1 = 2/length(Ez_tot); % Length of one vector element of Ez,tot in m
168 d_line = round(30e-2/step1); % Length, in terms of number of vector elements,
169                              % of the diameter line of the test-zone
170 line_col = ceil(length(Ez_tot)/2); % Center column of test-zone located at y = 0 m
171 line_row = line_col;  % Center row of test-zone located at x = Dm
172                       % line_row= round(Dm/step1).
173
174 phase_tot = angle(Ez_tot); % Calculate of the P-values in the 2 m × 2 m area
175
176 phase_line_whole = phase_tot(line_row,:);     % Extract entire row where test-zone lies
177 phase_line_whole = unwrap(phase_line_whole);  % Unwrap the phase
178 phase_line_whole = rad2deg(phase_line_whole); % Convert from radiance to degrees
179
180 % Extract ϕ-values lying on the diameter (center) line of the test-zone
181 phase_line = phase_line_whole(ceil(line_col-d_line/2)+1:floor(line_col+d_line/2));
182 phase_line_mean = mean(phase_line); % Calculate mean value of the extracted
183                                     % ϕ-values along the diameter line of the test-zone
184 phase_line_norm = phase_line-phase_line_mean; % Normalize the extracted phase samples in the test-zone
185
186 %%%%%%%%%%%%%%%%%%%%%%%%%%%%%%%%%%%%%%%%%%%%%%%%%%%%%%%%%%%%%%%%%%%%%%%
187 %                       Calculate the FOM's                             %
188 %%%%%%%%%%%%%%%%%%%%%%%%%%%%%%%%%%%%%%%%%%%%%%%%%%%%%%%%%%%%%%%%%%%%%%%
189
190 power_mean_circular_region = mean(values); % Calculate mean of the extracted
191                                            % P-values inside the test-zone
192 power_norm_circular_region = (values/power_mean_circular_region)'; % Normalize the extracted values
193 STD = std(power_norm_circular_region);
194 power_spread = 5*log10((1+STD)/(1-STD));
195
196 phase_spread = max( abs( phase_line-phase_line_mean ) );
```

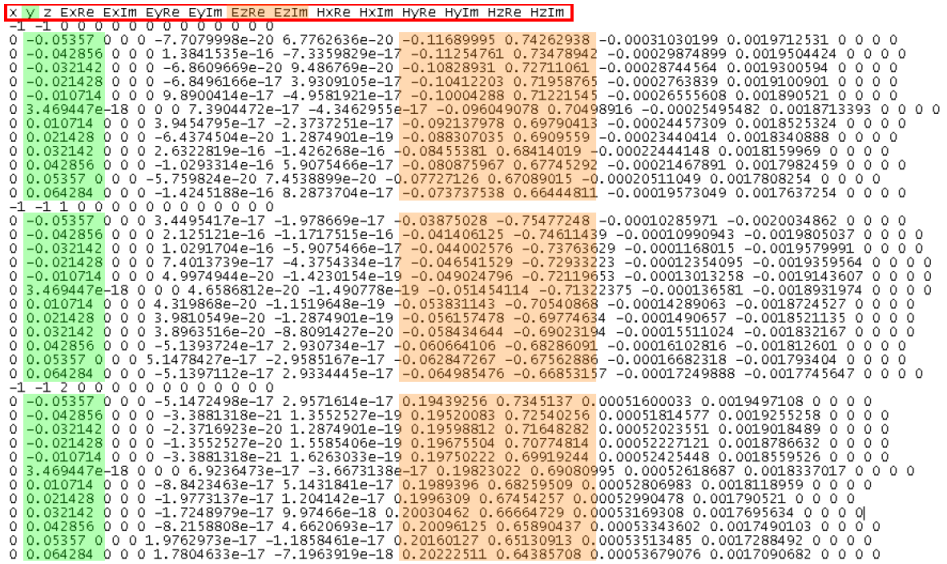

Figure A.1: Screenshot of the nearfiled.dat file.

A.2 The Nearfield.dat File

The near-field points sampled at each dipole position in WSAP are stored in the nearfield.dat file. Figure A.1 show a screenshot of the file. The file header is marked with the red rectangle. Two categories of data are stored in the file. The first one is the coordinates of the sample points (marked with a transparent red color), while the other one is the real- and imaginary parts of the near-field components. All sample points corresponding to the same dipole position are grouped together in the file. It can hence be seen that data from three different dipole positions are shown. The sample points are located along the y-axis ($x = z = 0$) and are ordered from y_{min} to y_{max}, where y_{min} (y_{max}) is the position of the sample point located furthest away from the origo on the negative (positive) y-axis. A very thin dipole was used in the simulations. It was therefore sufficient to only use the E_z-components to accurately reconstruct the near-field from the linear array. The real- and imaginary parts of E_z are marked with a transparent orange color.

A.3 The .geo File

The .geo file contains information about the geometry of the dipole that was used in WSAP. A summary of the data that is contained in the .geo file is shown in Table A.1. Numerical values of the data in the .geo files corresponding to area 1-4 are also displayed. Note that the coordinates refer to the initial position of the dipole. For the smaller arrays with 1, 24 and 36 elements were $x_1 = x_2 = 0$ m, $y_1 = y_2 = -1$ m used. For the remaining parameters were the same numerical values as listed in Table A.1 used.

A.4 Simulated results of the 48-slot array used with a reflector

As explained in the Section 4.3, was one of the 48-slot arrays simulated with a cylindrical reflector. The array with rounded slots was considered for this simulation. The code

Table A.1: Summary of the data that is contained in the .geo file.

Variable	Description	Value (128 element array)
x_1	Start position in x, end 1 of the dipole	0 m for area 1-2 and 1 m for area 2-4 (see Figure 3.3)
y_1	Start position in y, end 1 of the dipole	-1 m for area 1-3 and 0 m for area 1-4
z_1	Start position in z, end 1 of the dipole	$-\frac{\lambda}{4}$, $\lambda = 0.1071$ m for area 1-4
x_2	Start position in x, end 2 of the dipole	0 m for area 1-2 and 1 m for area 2-4
y_2	Start position in y, end 2 of the dipole	-1 m for area 1-3 and 0 m for area 1-4
z_2	Start position in z, end 2 of the dipole	$\frac{\lambda}{4}$ for area 1-4.
n_{basis}	Number of basis functions used to calculate the current on the dipole	11
t_{dipole}	Thickness of the dipole	1×10^{-6} m
name	String containing the name of the dipole as defined by the user	

used to generate the graphs that will be displayed in this Section utilized the embedded radiation pattern from the array. The embedded pattern is the radiation pattern from an excited slot in the array when the other slots are passive, i.e. terminated with matched loads. This means, unlike the isolated radiation pattern, that the effect of mutual coupling from the other slots in the array is taken into account. The embedded radiation pattern was obtained in CST by placing waveguide ports inside one of the waveguides. The waveguide ports were placed to delimit an area inside the waveguide that only covered the slot for which the embedded patter should be obtained (see Figure A.2). Note that two ports with opposite orientation (indicated by the surface normals in the figure) were used on either side of the delimited area. The orientation of the ports was set in the menu of each waveguide port. A field monitor was defined at 28 GHz and the embedded radiation pattern was obtained by selecting the CO-polar radiation pattern corresponding to any one of the ports with surface normal pointing inward towards the area, i.e. port 2 and 3 in the Figure. The same setting of the polarization and the orientation of the waveguide as described in Section 3.3.3 was used.

Two arrays with different number of slots were considered. The first array had 48 slots, while the other array had 64 slots. The arrays will be referred to as the 48-case and 64-case throughout this Section. The power and phase over a $1\,\text{m} \times 1.5\,\text{m}$ (y m $\times$ z m) area is shown in Figure A.3 for the two cases. Note that distance from the reflector is measured in z and that the linear array is extended along y in Figure A.3. The same does also apply for the other Figures that is presented in this Section. Also note that all Figures shown in this Section were simulated at 28 GHz.

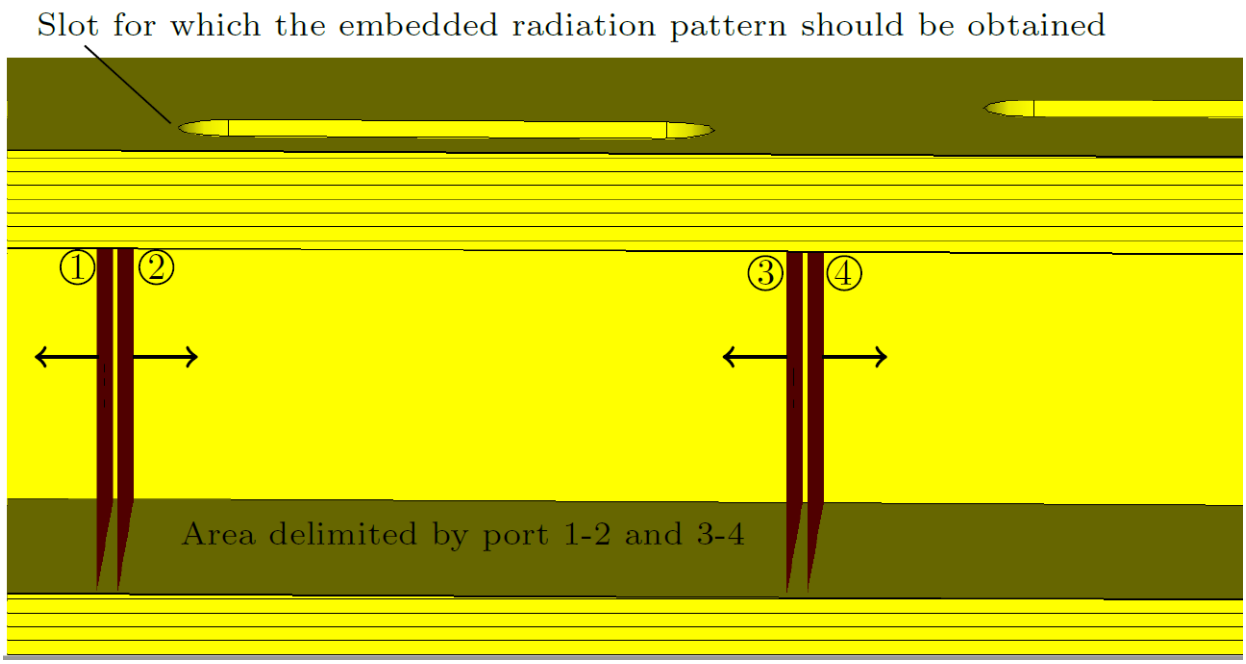

Figure A.2: Setup used to obtain the embedded radiation pattern from one rounded slot in the n_s-section. The orientation of the waveports is indicated with the surface normals. The distance between the ports is highly exaggerated. A considerably smaller distance (0.01 mm) was used when the embedded radiation pattern of the slot was obtained.

Figure. A.4 show the power spread as function of the distance from the reflector to the center of the test zone and as a function of the radius of the test zone for the two cases. Note that a radius, R= 15 cm is considered in A.4(b) and A.4(d) and that a distance of $z = 1$ m from the reflector is considered. The distance in A.4(a) and A.4(c) is the sum of the focal distance, F, and the distance D, which is measured from the linear array to the center of the test zone (see Figure 2.11). It can clearly be seen in the figure that the overall performance is better for the 64-case.

The variation of the phase (note: much related to but not the same as the phase spread) across the 1 m × 1.5 m area at a distance of $z = 1$ m from the reflector is show in Figure A.5. It can be seen that the phase variation is smaller for the 64-case, which should imply that the phase spread also is smaller for this case.

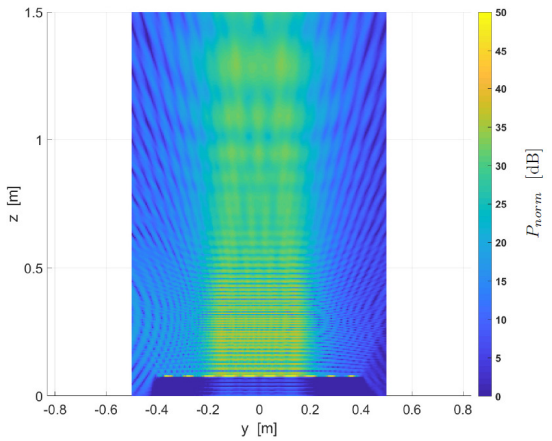

(a) $N = 48$

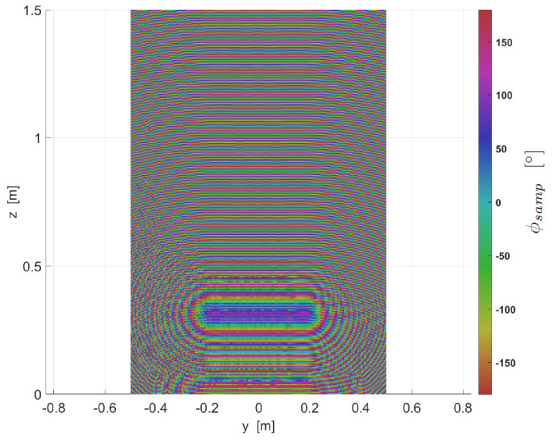

(b) $N = 48$

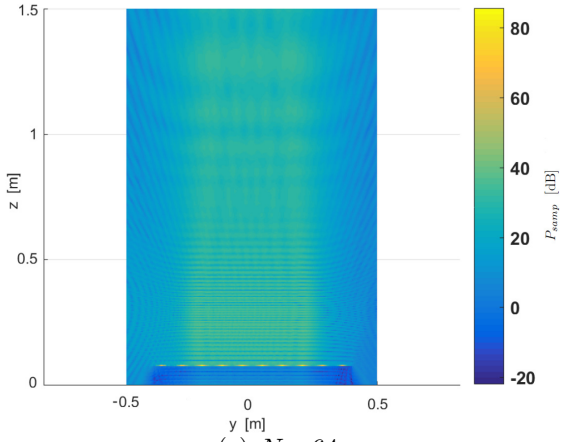

(c) $N = 64$

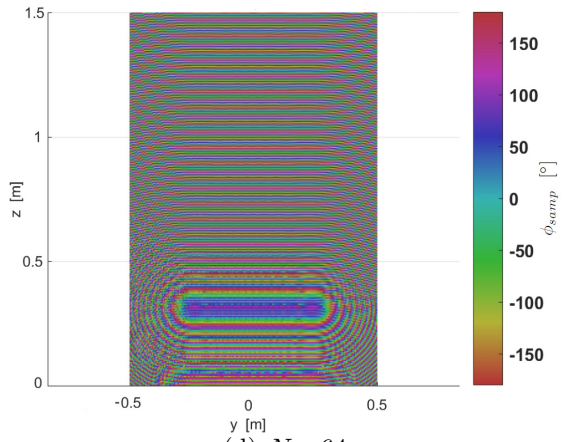

(d) $N = 64$

Figure A.3: power (a) and (b) and phase (b) and (d) over a $1\,\mathrm{m} \times 1.5\,\mathrm{m}$ area. The 48-case is displayed in (a) and (b) and the 64-case in (b) and (d).

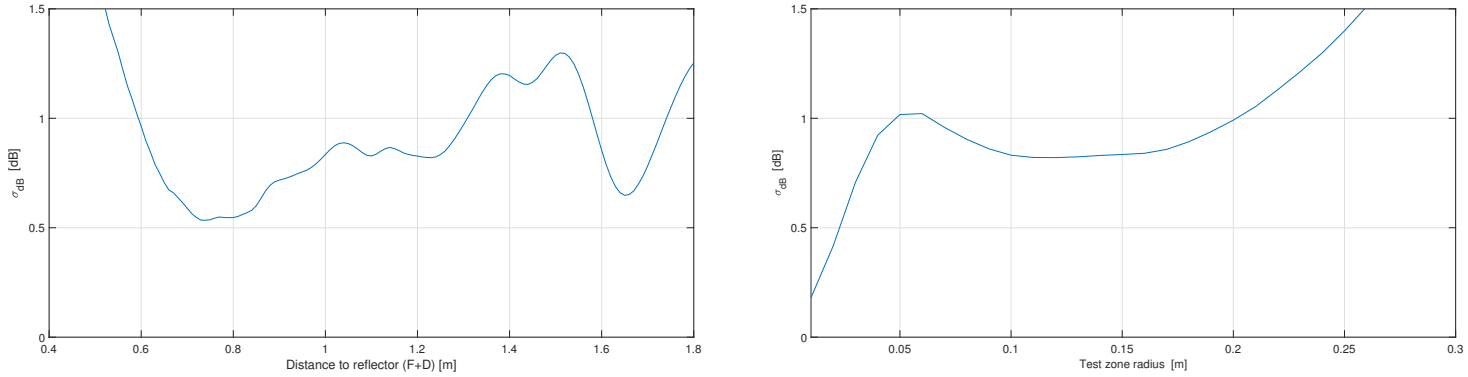

(a) $N = 48$

(b) $N = 48$

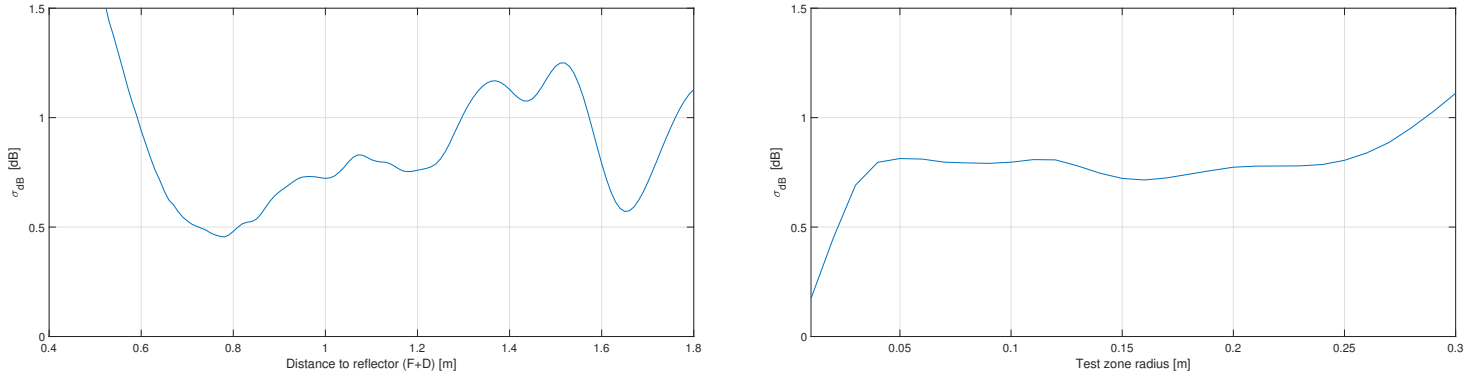

(c) $N = 64$

(d) $N = 64$

Figure A.4: Power spread as a function of the distance from the reflector (a) and (c) and as a function of the radius of the test-zone (b) and (d). The 48-case is displayed in (a) and (b) and the 64-case in (c) and (d). Note that (b) and (d) are evaluated at a distance of $z = 1\,\mathrm{m}$.

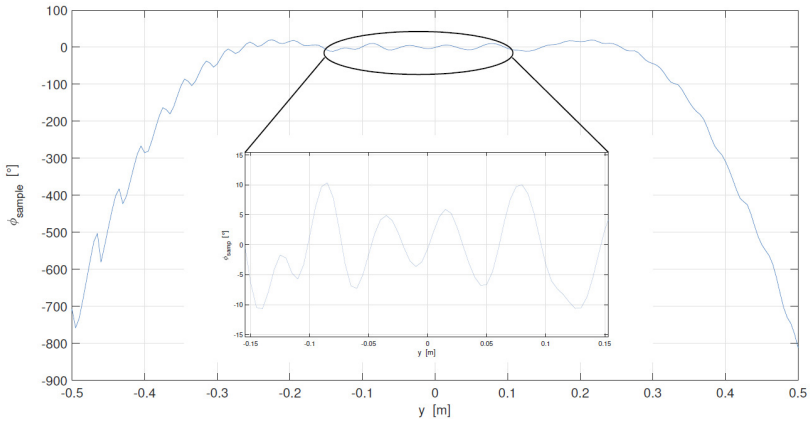

(a) $N = 48$

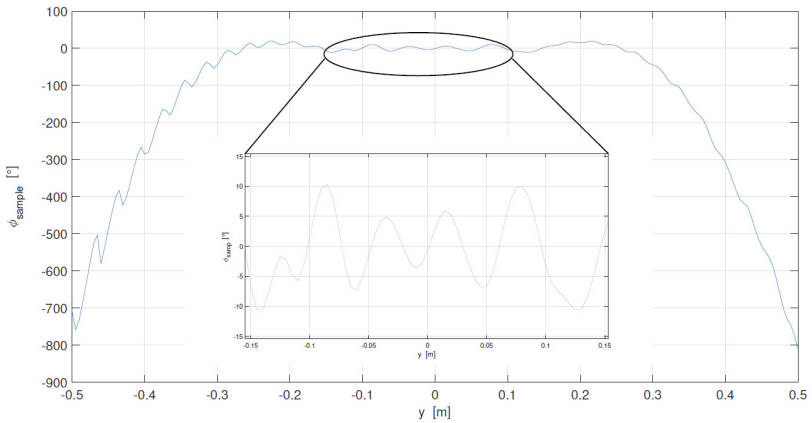

(b) $N = 64$

Figure A.5: Phase variation across the 1 m × 1.5 m area for (a) the 48-case (b) the 64-case. Note that a distance of $z = 1$ m is considered in (a) and (b).